Studies on the Electrodeposition of Copper and Lead towards Enhanced Metal Refining Processes

Masayuki Miyamoto

2024

Studies on the Electrodeposition of Copper and Lead towards Enhanced Metal Refining Processes

Masayuki Miyamoto

Department of Materials Science and Engineering

Graduate School of Engineering

Kyoto University

March 2024

Contents

General Introduction

1. Extractive metallurgy of non-ferrous metals

The production of non-ferrous metals is a crucial aspect of modern society. In particular, extractive metallurgy of such metals, involving the separation of various elements, can allow recycling of metal resources on an industrial scale. Such processes are typically used to recover copper, lead, and zinc but may also be employed to obtain gold, silver, platinum group metals (PGMs), nickel, cobalt, antimony, bismuth, selenium, tellurium, cadmium, tin, and other elements from in-process residues generated as by-products. At present, the grade of some primary resource ores, such as those containing copper, are exhibiting ongoing declines,[1,2] and both technological challenges and rising refining costs are becoming problematic.[3] In addition, the availability of certain minor metals may be restricted as a consequence of disruptions in supply chains as well as issues related to a lack of viable extraction technologies and environmental concerns.[4] Therefore, it is important to ensure stable supplies of these metals. Many industrial-scale facilities currently recover metals from secondary raw materials, such as scrap metals, waste batteries, and waste electrical and electronic equipment, as well as natural ores. Such recovery processes often involve simultaneous detoxification of the waste material.

The refining of non-ferrous metals commonly includes high-temperature pyroprocessing combined with wet chemical processes based on the dissolution of these metals in water or organic solvents. Figure G.1 summarizes a typical system by which copper is extracted from raw materials. In this process, copper concentrate (primarily composed of chalcopyrite; $CuFeS_2$) is first fed into a smelting device such as flash furnace.[5] Recycled raw materials, such as wire and cable

scrap, shredded automobiles, and waste electronics,[6] together with in-process residues from lead and zinc refineries[7] can also be employed as secondary raw materials. During the initial matte smelting stage, iron-based components of the raw materials undergo oxidation and are reacted with a silica flux to form an oxide-rich molten layer known as fayalite slag and having the formula $FeO–SiO_2$. In addition, the copper components are concentrated to form a sulfide-rich molten phase known as matte and having the formula $CuS_2–FeS$ that separates from the other phases within the furnace. Sulfur is released in the form of sulfur dioxide by off-gassing and is subsequently captured as sulfuric acid after heat and dust recovery. Following this, the matte undergoes a two-stage oxidation process in a converter. The first stage removes residual iron as slag while the second stage generates metallic blister copper. The latter is subjected to fire refining to remove sulfur and oxygen and is then cast into anode electrodes in preparation for further refining via a subsequent wet electrolytic process.

The copper anodes are purified through an electrorefining process utilizing a copper sulfate solution with sulfuric acid as the electrolyte. This process involves the dissolution of the impure copper anodes (with a typical purity of 98.5–99.5%) followed by the electrodeposition of copper with a purity of 99.99% or greater at the cathodes,[8] such that residual impurities are removed. Impurity metals and compounds with a higher electrode potential than copper or a lower solubility in the electrolyte do not dissolve at the anodes but rather form a solid residue known as anode slime. This material either adheres to or detaches from the anodes and accumulates at the bottom of the bath. Impurities having lower electrode potentials than copper dissolve in the electrolyte and are not deposited on the cathodes, allowing for their removal from the copper. The anode slime, which contains a significant amount of precious metals, can be further processed to recover these elements.[9,10]

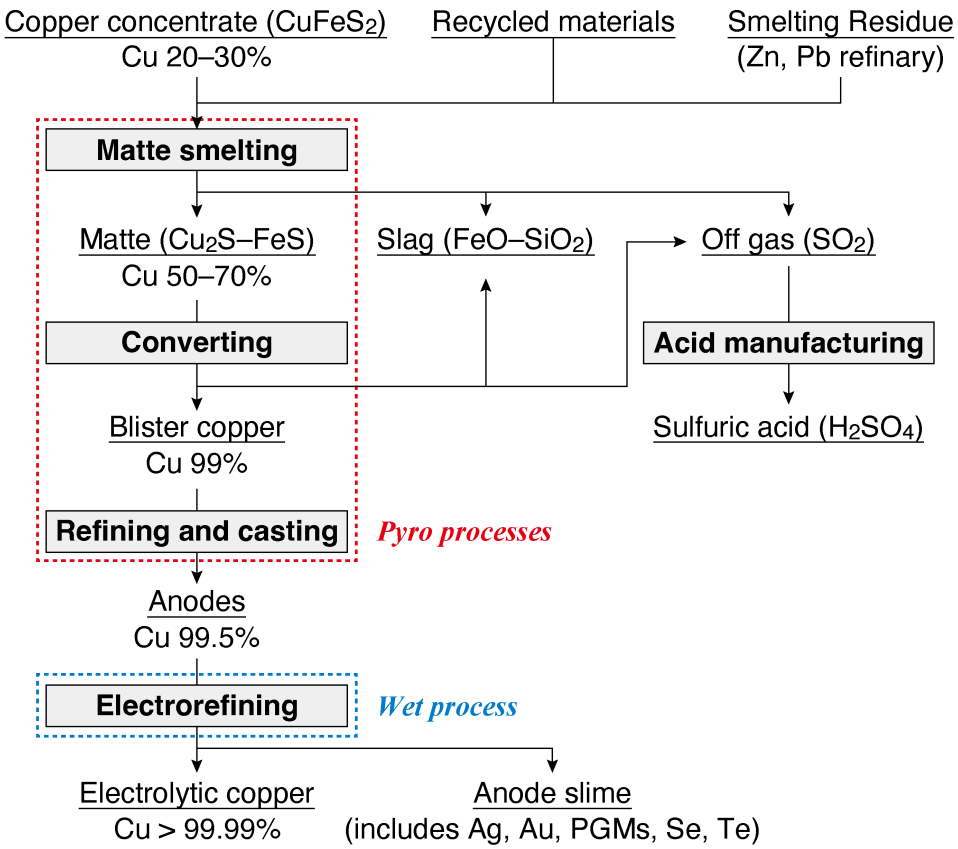

Figure G.1 Diagram summarizing the flow of a typical copper extraction process.

Wet electrolysis processes, such as electrorefining and electrowinning combined with leaching, purification, or solvent extraction, are generally used for the final refining of various metals because high-purity metals can be obtained more easily with these techniques compared with pyroprocessing. Electrorefining is often employed in the production of copper, silver, lead, tin, and bismuth after obtaining the crude raw materials via pyro smelting.[11] In contrast, electrowinning is used to process zinc, cadmium, manganese, chromium, nickel, cobalt, and copper from materials recovered from leaching solutions.[11] The latter process is selected in the case that it is relatively difficult to obtain crude metals by pyro smelting or hydrometallurgical processes that are dependent on the type of raw

material.[12–17] Although the majority of present-day electrolysis techniques have their roots in developments that took place over a century ago,[18–20] efforts to introduce various operational control improvements and process flow modifications are ongoing.

2. Recent advances in hydrometallurgical processes related to sustainable development

In the future, it will be necessary to devise innovative technological advancements and wet chemical process improvements to address various sustainability challenges and goals.

Pursuit of energy-saving, efficient processes

Reducing energy consumption and improving reaction efficiency are increasingly crucial, as are increases in mass, space, and time efficiencies.[21,22] To further reduce energy consumption and power intensity in electrolysis processes, measures have been developed to avoid short circuiting between electrodes (that is, anode–cathode pairs), which is a known cause of current loss. These measures include perpendicular alignment of the electrodes, leveling of electrode bends, and prevention of abnormal electrodeposition.[8,22–24] Additionally, techniques for the detection of short circuits have been implemented.[25–28] Insoluble anode materials that promote oxygen evolution at lower overpotentials have also been introduced into electrowinning systems,[17,22,29,30] and more energy-efficient electrode reactions have been employed at both the anode and cathode.[17,22]

Promotion of metal recycling

The optimization of processes for metal recycling is currently a pressing issue. Unlike natural ores, recycled raw materials often contain

varying amounts and types of impurities and are prone to fluctuations, which can adversely affect refining capacity and lead to unexpected operational malfunctions. Therefore, it is crucial to develop effective strategies to address these issues. Taking conventional copper electrorefining as an example, increased impurity concentrations at the copper anodes can cause various electrolytic abnormalities and result in operational challenges such as anode passivation and short circuits between electrodes caused by abnormal nodular electrodeposition.[31] Techniques to mitigate these problems are being developed at various levels, ranging from operational management to the design of novel processes.[32–34]

Transitioning to environmentally benign processes

There is presently a need to shift toward processes that reduce both the use and emission of hazardous substances. As an example, electrorefining of lead, tin, and bismuth is currently being explored as an alternative to conventional electrorefining[11] using fluorosilicic acid. The electrorefining process that is used at present for lead refining employs a fluorosilicic acid electrolyte and was first proposed by Betts in 1901.[19,20] As a consequence of growing concern for the environment, there is a need to replace such antiquated processes with electrolytic systems that do not involve fluorine and to implement improved wastewater treatments. In Japan, national effluent standards are provided by the Water Pollution Prevention Act,[35] and fluorine effluent limits for various industries, including nonferrous smelting and electroplating, have become increasingly strict over the last two decades. Techniques for the removal of fluorine from industrial wastewater have thus been developed, including those intended for use in the mining, smelting, and electroplating industries, in the generation of photovoltaics such as solar panels, and in the fabrication of batteries.[36–38] Emissions of gaseous hydrofluoric acid and silicon

tetrafluoride are also a concern[39,40] and alternative bath compounds such as sulfamic acid have been proposed and are currently utilized in some plants.[41–43]

The use of alkaline cyanide solutions for the complexation leaching of metals such as gold and silver has long been associated with the discharge of toxic waste containing cyanide ions. In recent years, there has been increased interest in the development of environmentally friendly cyanide-free leaching solutions such as thiosulfate-ammonia and thiourea systems.[44,45]

Improving wet processes is an essential aspect of achieving sustainable development in the future. Recently, Binnemans and Jones proposed the concept of "circular hydrometallurgy" as an approach to sustainable processing in hydrometallurgy.[21] This concept is based on the Twelve Principles of Green Chemistry as employed in the field of chemical synthesis[46,47] along with the Twelve Principles of Green Engineering[48] and the Nine Principles of Green Engineering in the Sandestin Declaration[49] in the field of engineering. Circular hydrometallurgy comprises twelve principles that redesign the hydrometallurgy flow to produce a cyclical system that reduces both waste and reagent consumption while increasing energy efficiency. System designs based on such concept has recently gained importance, including process analysis and development with a particular focus on factors and requirements that are unique to actual industrial processes.

3. Outline of the present work

This thesis presents research on the topic of electrorefining related to advancements in metal refining, focusing on factors specific to actual processes. The thesis is divided into three chapters, addressing two

topics. The first topic consists of abnormal electrodeposition (that is, nodulation) occurring during copper electrorefining and is examined in Chapters 1 and 2. The second topic pertains to the development of a new, environmentally benign lead electrolysis bath and is contained in Chapter 3.

Nodulation in copper electrorefining

Chapters 1 and 2 discuss the factors that contribute to nodule growth in association with copper electrorefining. One major issue that must be addressed is the current loss caused by short circuits between electrodes (that is, anode–cathode pairs) due to the formation of nodules.[8] Previous studies have suggested that impurity particles, such as anode slime, inadvertently attached to the cathode surfaces can serve as nuclei for nodule formation.[50,51] However, until recently, there has been minimal research assessing the factors that cause nodules to grow until they come into contact with the anode.[25,52–54] The following chapters examine several factors related to impurity elements that may be problematic in real-world processes and propose strategies to suppress nodule growth.

Chapter 1 focuses on the incorporation of anode slime particles in the electrolyte into the nodules as a factor contributing to nodule growth. Data confirm that anode slime particles can not only act as nuclei for nodules but can also promote further growth upon being incorporated into the nodules. The effects of particle inclusion on the deposition morphology and growth behavior of nodules were clarified based on observations and analyses of nodules recovered from an industrial tank house. Numerical simulations were also performed to analyze tertiary current distribution and particle transport phenomena and to model convection around the nodules and the behavior of particles in the electrolyte. Based on the results, a growth mechanism involving particle incorporation into the nodules is proposed and discussed.

Additionally, suggestions for operational control to reduce nodule growth and improve the process are provided.

Chapter 2 discusses the effect of impurity ions in the electrolyte, specifically nickel and antimony, on nodule growth. The increased processing of recycled materials has led to an increase in nickel and antimony inputs to copper smelters, making it crucial to address the impact of these elements on nodule growth. This chapter reports electrolysis experiments conducted using electrodes with nodule-mimicking protrusions to evaluate the effects of impurity ions on copper deposition at nodules. The results indicate that these impurity ions promote the growth of the protrusions by affecting the internal microstructure and macroscopic morphology of deposited copper on the protrusions. Numerical simulations of the secondary current distribution indicate that surface roughness on the protrusions promotes current concentration, thus contributing to growth enhancement. These impurity ions are thus thought to increase the formation of coarse grains at the deposition interface, leading to an early transition to a rapid growth mode with a rough deposition pattern. The data from these analyses suggests that controlling the bath composition can suppress nodule growth.

An environmentally benign lead electrolysis bath

Chapter 3 discusses the potential applications of highly concentrated calcium chloride solutions as novel lead electrolysis baths with reduced environmental impacts. New systems such as these must meet certain requirements to allow for practical applications in actual industrial processes. These requirements include sufficient dissolution of lead ions, cost-effectiveness, and low environmental impact. Unfortunately, the number of electrolysis systems that meet these requirements is limited. The Betts process is advantageous due to the high solubility of lead ions and the ease of obtaining smooth deposits when employing

various additives except in the presence of fluorine.[40,55] Sulfuric acid and hydrochloric acid are commonly used for the electrolysis of nonferrous metals but do not allow sufficient dissolution of lead.[42] However, nitric acid can be problematic because of the potential reduction of nitrate ions. Sulfamic acid can be used as an alternative agent for the electrodeposition of lead because this compound readily dissolves lead ions while producing smooth deposits.[41,42] Hence, sulfamic acid systems have been explored and are now used commercially. The potential to utilize methanesulfonic acid in hydrometallurgical processes has gained attention, as this acid exhibits high chemical stability and the ability to dissolve a number of metals while having a reduced environmental impact.[56–58] However, the compounds noted above are still more expensive than more common acids, which presents an economic disadvantage. Fluoroboric acid systems also readily dissolve lead ions but the use of such systems is presently limited to specific electrodeposition processes, such as solder electroplating.[42,43] Electrodeposition can also be carried out using ionic liquids[59] and deep eutectic solvents,[60] although the practical application of these non-aqueous solvents is associated with several engineering challenges.[61] Thus, there remains a need to develop new systems suitable for actual processes.

The work reported herein focused on the use of highly concentrated aqueous solutions of calcium chloride (or hydrate melts) as lead electrolysis baths. Calcium chloride is a readily available, inexpensive, and relatively low-toxic compound. The high chloride ion activities of such solutions can be expected to solubilize lead chloride via the formation of chloride complexes. This study investigated the solubility of lead chloride in concentrated aqueous solutions of calcium chloride and evaluated the electrochemical characteristics of such systems during lead electrodeposition to assess applications related to lead electrolysis.

References

1. P. Crowson, *Resour. Policy*, **37**(1), 59–72 (2012).
2. S. Northey, S. Mohr, G. M. Mudd, Z. Weng, and D. Giurco, *Resour. Conserv. Recycl.*, **83**, 190–201 (2014).
3. T. Norgate and S. Jahanshahi, *Miner. Eng.*, **23**(2), 65–73 (2010).
4. T. H. Okabe, *Miner. Process. Extr. Metall.*, **126**(1–2), 22–32 (2017).
5. M. E. Schlesinger, M. J. King, K. C. Sole, and W. G. Davenport, in *Extractive Metallurgy of Copper*, edited by M. E. Schlesinger, M. J. King, K. C. Sole, and W. G. Davenport, 5th Ed. (Elsevier, Oxford, 2011), pp. 1–12.
6. M. E. Schlesinger, M. J. King, K. C. Sole, and W. G. Davenport, in *Extractive Metallurgy of Copper*, edited by M. E. Schlesinger, M. J. King, K. C. Sole, and W. G. Davenport, 5th Ed. (Elsevier, Oxford, 2011), pp. 373–387.
7. T. Nakamura, *J. MMIJ*, **123**(12), 570–574 (2007).
8. M. E. Schlesinger, M. J. King, K. C. Sole, and W. G. Davenport, in *Extractive Metallurgy of Copper*, edited by M. E. Schlesinger, M. J. King, K. C. Sole, and W. G. Davenport, 5th Ed. (Elsevier, Oxford, 2011), pp. 251–280.
9. G. Liu, Y. Wu, A. Tang, D. Pan, and B. Li, *Hydrometallurgy*, **197**, 105460 (2020).
10. J. Hait, R. K. Jana, and S. K. Sanyal, *Miner. Process. Extr. Metall.*, **118**(4), 240–252 (2009).
11. N. Sato and Y. Waseda, (Eds.) *Shisshiki Purosesu: Youeki · Youbai · Haisuishori* (Uchidarokakuho, Tokyo, 2018), pp. 165–177.

12. M. E. Schlesinger, M. J. King, K. C. Sole, and W. G. Davenport, in *Extractive Metallurgy of Copper*, edited by M. E. Schlesinger, M. J. King, K. C. Sole, and W. G. Davenport, 5th Ed. (Elsevier, Oxford, 2011), pp. 281–322.
13. M. E. Schlesinger, M. J. King, K. C. Sole, and W. G. Davenport, in *Extractive Metallurgy of Copper*, edited by M. E. Schlesinger, M. J. King, K. C. Sole, and W. G. Davenport, 5th Ed. (Elsevier, Oxford, 2011), pp. 349–372.
14. H. R. Watling, *Hydrometallurgy*, **140**, 163–180 (2013).
15. H. R. Watling, *Hydrometallurgy*, **146**, 96–110 (2014).
16. R. R. Moskalyk and A. M. Alfantazi, *Miner. Eng.*, **15**(8), 593–605 (2002).
17. M. Moats and M. Free, *JOM*, **59**(10), 34–36 (2007).
18. J. B. Elkington, *Improvement in the manufacture of copper and in separating other metals therefrom,* US Patent US100131A, November 3, 1865.
19. A. G. Betts, *Electrodeposited lead*, US Patent US713278, November 11, 1902.
20. A. G. Betts, *Art of process of refining lead by electrolysis*, US Patent US679824, August 6, 1901.
21. K. Binnemans and P. T. Jones, *J. Sustain. Metall.*, **9**(1), 1–25 (2023).
22. M. S. Moats, in *Energy efficiency in the Minerals Industry*, edited by K. Awuah-Offei (Springer Cham, 2018), pp. 213–232.
23. H. Khayatzadeh and K. Tahmasebi, *JOM*, **76**(1), 452–463 (2024).
24. A. Filzwieser, I. Filzwieser, and S. Konetschnik, *JOM*, **64**(11), 1290–1295 (2012).
25. Q. Zeng, C. Li, Y. Meng, J. Tie, R. Zhao, and Z. Zhang, *Measurement*, **164**, 108015 (2020).
26. E. P. Wiechmann, A. S. Morales, and P. Aqueveque, *IEEE Trans. Ind. Appl.*, **45**(5), 1575–1582 (2009).

27. P. E. Aqueveque, E. P. Wiechmann, J. Herrera, and E. J. Pino, *IEEE Trans. Ind. Appl.*, **51**(3), 2607–2614 (2015).
28. P. E. Aqueveque, E. P. Wiechmann, and R. P. Burgos, *IEEE Trans. Ind. Appl.*, **45**(4), 1225–1231 (2009).
29. M. Clancy, C. J. Bettles, A. Stuart, and N. Birbilis, *Hydrometallurgy*, **131**–**132**, 144–157 (2013).
30. W. Zhang, E. Ghali, and G. Houlachi, *Hydrometallurgy*, **169**, 456–467 (2017).
31. H. Sasaki, Y. Ninomiya, and T. H. Okabe, *J. MMIJ*, **136**(3), 14–24 (2020).
32. H. Sasaki and T. H. Okabe, *J. MMIJ*, **136**(7), 77–87 (2020).
33. A. Tuncuk, V. Stazi, A. Akcil, E. Y. Yazici, and H. Deveci, *Miner. Eng.*, **25**(1), 28–37 (2012).
34. M. Ghodrat, M. A. Rhamdhani, G. Brooks, S. Masood, and G. Corder, *J. Clean. Prod.*, **126**, 178–190 (2016).
35. Ministry of the Environment, Government of Japan, *Japanese Effluent Standards*, WWW document, [cited January 9, 2024] (https://www.env.go.jp/en/water/wq/nes.html).
36. K. Wan, L. Huang, J. Yan, B. Ma, X. Huang, Z. Luo, H. Zhang, and T. Xiao, *Sci. Total Environ.*, **773**, 145535 (2021).
37. J. He, Y. Yang, Z. Wu, C. Xie, K. Zhang, L. Kong, and J. Liu, *J. Environ. Chem. Eng.*, **8**(6), 104516 (2020).
38. T. Fukuta, F. Seto, and K. Yagishita, *J. Surf. Finish. Soc. Japan*, **55**(8), 506–510 (2004).
39. C. A. Jacobson, *J. Phys. Chem.*, **27**(8), 761–770 (1923).
40. J. A. González-Domínguez, E. Peters, and D. B. Dreisinger, *J. Appl. Electrochem.*, **21**(3), 189–202 (1991).
41. R. Piontelli, *J. Electrochem. Soc.*, **94**(3), 106–108 (1948).
42. M. Jordan, in *Modern Electroplating*, edited by M. Schlesinger and M. Paunovic, 5th Ed. (John Wiley & Sons, New York, 2010), pp. 249–263.

43. M. Jordan, in *Modern Electroplating*, edited by M. Schlesinger and M. Paunovic, 5th Ed. (John Wiley & Sons, New York, 2010), pp. 265–284.
44. G. Senanayake, *Miner. Eng.*, **17**(6), 785–801 (2004).
45. J. Li, J. Kou, C. Sun, N. Zhang, and H. Zhang, *Miner. Eng.*, **197**, 108074 (2023).
46. P. T. Anastas and J. C. Warner, *Green Chemistry: Theory and Practice* (Oxford University Press, Oxford, 1998).
47. P. Anastas and N. Eghbali, *Chem. Soc. Rev.*, **39**(1), 301–312 (2010).
48. P. T. Anastas and J. B. Zimmerman, *Environ. Sci. Technol.*, **37**(5), 94A-101A (2003).
49. M. A. Abraham and N. Nguyen, *Environ. Prog.*, **22**(4), 233–236 (2003).
50. J. E. Dutrizac and T. T. Chen, in *4th International Conference COPPER 99-COBRE 99* (1999), pp. 383 – 403.
51. T. N. Andersen, C. H. Pitt, and L. S. Livingston, *J. Appl. Electrochem.*, **13**(4), 429–438 (1983).
52. K. Adachi, Y. Nakai, S. Mitsuno, M. Miyamoto, A. Kitada, K. Fukami, and K. Murase, *J. MMIJ*, **136**(2), 8–13 (2020).
53. Y. Nakai, K. Adachi, A. Kitada, K. Fukami, and K. Murase, in *Rare Metal Technology 2018*, edited by H. Kim, B. Wesstrom, S. Alam, T. Ouchi, G. Azimi, N. R. Neelameggham, S. Wang, and X. Guan (Springer Cham, 2018), pp. 319–323.
54. K. Adachi, Y. Nakai, A. Kitada, K. Fukami, and K. Murase, in *Rare Metal Technology 2018*, edited by H. Kim, B. Wesstrom, S. Alam, T. Ouchi, G. Azimi, N. R. Neelameggham, S. Wang, and X. Guan (Springer Cham, 2018), pp. 215–222.
55. C. J. Krauss, *JOM*, **28**(11), 4–9 (1976).
56. K. Binnemans and P. T. Jones, *J. Sustain. Metall.*, **9**(1), 26–45 (2023).

57. M. D. Gernon, M. Wu, T. Buszta, and P. Janney, *Green Chem.*, **1**(3), 127–140 (1999).
58. B. Jin and D. B. Dreisinger, *Sep. Purif. Technol.*, **170**, 199–207 (2016).
59. S. Tan, F. E. Bedoya-Lora, J. P. Hallett, and G. H. Kelsall, *Electrochim. Acta*, **376**, 137893 (2021).
60. Y.-S. Liao, P.-Y. Chen, and I.-W. Sun, *Electrochim. Acta*, **214**, 265–275 (2016).
61. K. Binnemans and P. T. Jones, *J. Sustain. Metall.*, **9**(2), 423–438 (2023).

Chapter 1

Mechanism of Nodular Growth in Copper Electrorefining with the Inclusion of Impurity Particles under Natural Convection

1.1. Introduction

In copper electrorefining, current efficiency needs to be close to 100% in principle because Cu electrodeposition does not involve hydrogen evolution. However, the efficiency of current operations is generally 93–98%.[1] This loss is mainly attributed to partial short circuits due to nodulation occurring on cathodes. Accidental short circuits result in electrode pairs that do not undergo an electrolytic reaction despite the flow of current, which reduces current efficiency. The loss of efficiency is also caused by the parasitic oxidation of ferrous ions at the anode, which induces the formation of ferric ions and corrosion of the electrolytic copper on the cathode. Parasitic or nonproductive reactions by ferric ions and oxygen result in a current loss of approximately 1%.[1]

Previous studies demonstrated the formation of micro protrusions on the cathode surface when conductive particles were suspended in an electrolyte,[2] and also that impurity particles derived from anode slime were present at the roots of nodules.[3] These findings suggest that nodules contain entrapped impurity particles, and that nodule formation is believed to be related to impurity particles on the cathode surface. However, direct evidence to form nodules from the impurity particles attached to the cathode is still not fully clarified. This is a topic of great interest, and therefore most studies have focused on the early stage of nodulation (nodule size of 1–2 mm or less). On the other hands, shifting the perspective to the subsequence of nodules formed, few have

investigated the mechanisms underlying anomalous nodular growth reaching the opposite anode, located at a distance of 25–35 mm from the cathode surface. Even when smooth copper deposition ($Cu^{2+} + 2e \rightarrow Cu$) proceeds at a current density of 350 A m^{-2} for one week, a typical operating condition and period, the thickness of deposits is only 7.8 mm, which demonstrates that nodular growth reaching the anode is anomalous.

In the previous study,[4–6] nodular growth behavior was quantitatively evaluated and modeled by lab-scale experiments and numerical simulations of the secondary current distribution using cathodes with intentional protrusions that mimic nodules. The findings obtained revealed that the height of protrusions increased exponentially with the duration of electrolysis due to current concentration caused by geometry of the protrusions. Further, when the protrusion height exceeded 10 mm, extremely rapid growth by macro-scale dendritic deposition occurred, and therefore it was concluded that it is important not to exceed a nodule size of 10 mm during the operating period to avoid short circuits. The threshold size of initial protrusion for whether or not a short circuit will occur within an industrial operating period was estimated to be 3 mm. Moreover, mold-releasing agents carried from the preceding anode casting process, which ranged in size from several to 20 mm, were found in some nodules and confirmed to be one of the main reasons for the formation of large nodules (refer to Section 1.2.1 for more details).

The inclusion of suspended particles in electrodeposited copper is expected to affect not only nodule outbreaks, but also the growth of nodules that are already formed. Indeed, the fact that impurity particles are incorporated into growing nodules is already known. However, the mechanism how impurity particles are transported to and incorporated into growing nodules to promote further growth has not been discussed. Zeng *et al*. examined the behaviors of particle transport and inclusion

in copper electrorefining using flat electrodes in numerical simulations of the tertiary current distribution and experimental analyses of particle inclusion.[7–10] Werner *et al*. performed numerical simulations based on the tertiary current distribution in copper electrowinning with a nodulous cathode.[11] However, limited information is currently available on the behaviors of particle transport and inclusion in terms of the convection of an electrolyte around nodules during electrorefining.

The present study investigated the mechanism of subsequent growth promoted by the successive inclusion of impurity particles in nodules that have already started to form. Impurity contents inside the nodules obtained from an industrial tank house were initially analyzed and the electrodeposition morphology of copper was examined based on observations of nodule cross-sections. The effects of particle inclusion on nodular growth were discussed. Furthermore, numerical simulations of the tertiary current distribution were performed to investigate the behavior of particle transport under natural convection around nodules. The nodular growth process with the transport and inclusion of suspended particles was also described.

1.2. Experimental

1.2.1. Experimental methods

Nodules obtained from an industrial copper tank house (acquired from JX Nippon Mining & Metals Corporation, a copper refinery in Japan) were dissolved in nitric acid and examined for inclusions. Nodules were classified into two types: relatively round and flat (Figure 1.1). Flake-like residues insoluble in nitric acid were obtained for the majority of flat nodules. These were identified as silica by X-ray diffraction, which is consistent with the mold-releasing agents used in the preceding anode

casting process. Therefore, mold-releasing agents carried from the preceding process were concluded to be one of the causes of nodule formation.[5] On the other hand, no noticeable residue was obtained from round-shaped nodules. The contents of impurity elements in round-shaped nodules were quantitatively assessed by analyzing the leachate as follows: nodules were immersed in 10% (w/w) nitric acid for 10 min with agitation at 200 rpm to clean the surface and were then cut into pieces using a high-speed precision cutting machine (Heiwa Technica, FINECUT HS-25A) as shown in Figure 1.2.

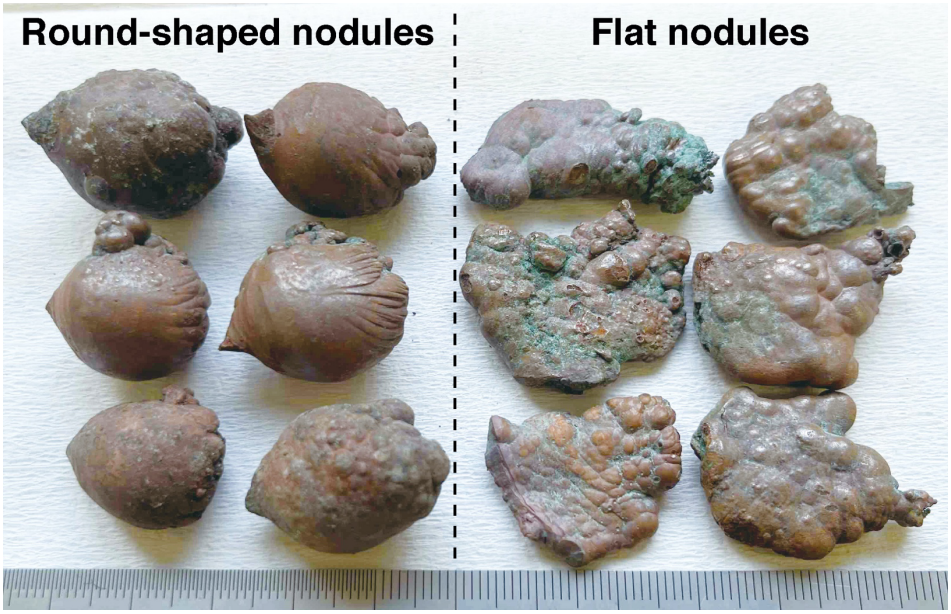

Figure 1.1 Typical types of nodules obtained from the industrial copper tank house: round-shaped nodules (left) and flat nodules (right).

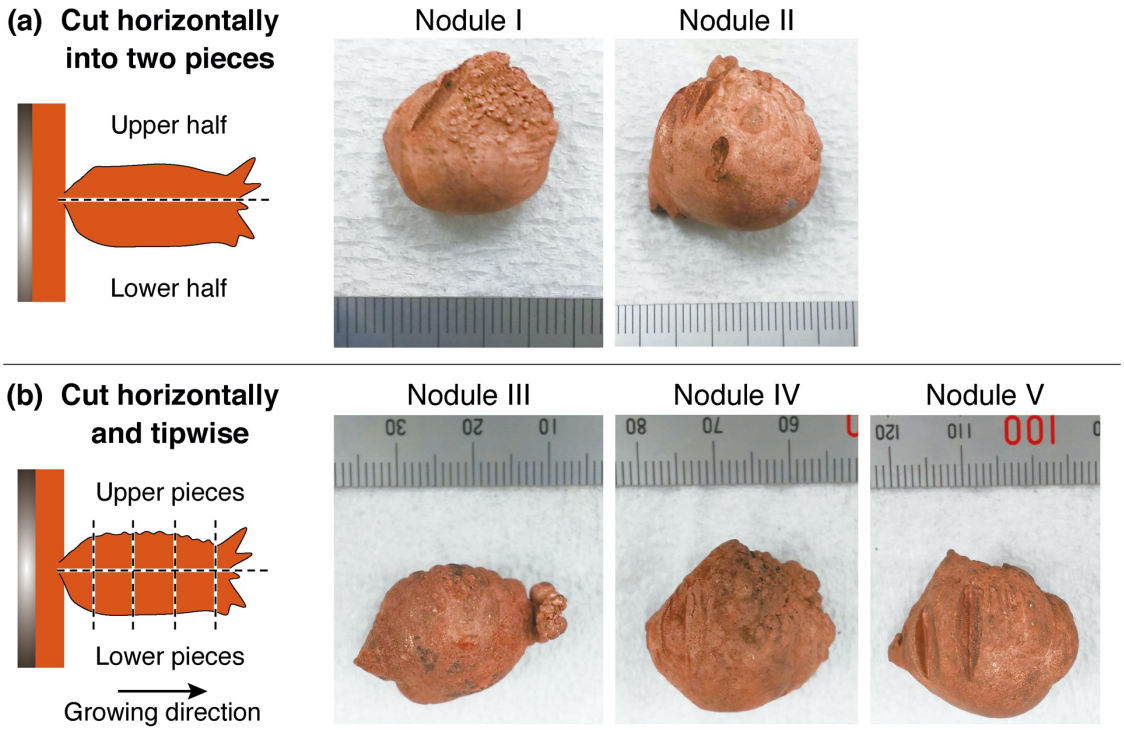

Figure 1.2 Cutting instructions and photographs of round-shaped nodules obtained from the industrial copper tank house. (a) Cut horizontally into two pieces and (b) cut horizontally and in the growing direction.

The orientation of the nodules on the cathode was identified as follows: the roots of nodules were initially detected by their characteristic pointed shapes since the root was buried in planar electrolytic copper. Their vertical orientation was then identified from the striated pattern on their surface. This pattern was considered to have formed by natural convection, and, thus, indicated the vertical orientation. The rough surface morphology also facilitated identifying the location of the upper surface. The rough upper surface of nodules is also consistent with the photograph of nodulous electrolytic copper taken at the copper tank house (Figure 1.12 in Section 1.3.4).

After the pieces had been weighed, they were dissolved in a series of a sufficient amount of 30% (w/w) nitric acid. Nitric acid was

prepared by diluting nitric acid (60% (w/w), Nacalai Tesque) with deionized water. The concentrations of impurity elements in the resulting leachates after suction filtration were then measured by inductively coupled plasma optical emission spectrometry (ICP-OES; SII NanoTechnology, SPS3500). Calibration curves were prepared for each element using the corresponding standard solution (1000 ppm (mg/L), FUJIFILM Wako Pure Chemical) diluted with 1 mol dm^{-3} nitric acid. The contents of impurity elements in each piece were obtained by multiplying the measured concentrations in each leachate by the leachate volume and dividing by the initial weight of the corresponding piece. The cut surfaces of some nodules were analyzed before dissolution by energy dispersive X-ray spectroscopy (EDX; EDAX, Element) attached to a scanning electron microscope (KEYENCE, VE-7800).

To compare impurity grades, the same experiment was also performed on electrolytic copper with non-nodulous growth that met product shipping standards (acquired from JX Nippon Mining & Metals Corporation). Electrolytic copper samples were cut into 10-mm square pieces from the top, middle, and bottom of two different electrolytic copper sheets. After the surface polishing of these samples with 240 grit abrasive paper, they were immersed in 10% (w/w) nitric acid for 2 min to remove surface dirt and oxide film, and then completely dissolved in a series of 30% (w/w) nitric acid.

Cross-sections were observed for another round-shaped nodule and for electrolytic copper accompanying a growing nodule. Samples were cut and cemented in epoxy resin. Cross-sections were continuously polished with 800–2000 grit abrasive paper and then mirror finished with an alumina abrasive with a particle size of 0.3 μm. Samples were immersed in an etchant, 20% (w/w) hydrochloric acid–ethanol mixture containing 0.3 mol dm^{-3} ferric chloride hexahydrate ($FeCl_3 \cdot 6H_2O$), for 1 min. The etchant was prepared by diluting hydrochloric acid (35–37%

(w/w), Nacalai Tesque) with ethanol (99.5% purity, Nacalai Tesque) and dissolving ferric chloride hexahydrate (99.0% purity, Nacalai Tesque). Etched samples were observed by optical microscopy (Olympus, BX51M).

1.2.2. Numerical simulation methods

Model description

In the present study, to clarify the behavior of natural convection and transport of impurity particles around nodules, numerical simulations based on the tertiary current distribution were performed using the finite element analysis software COMSOL Multiphysics®. It is important to note that the modeling of the tertiary current distribution and particle transport in copper electrorefining using COMSOL was originally proposed by Zeng *et al.*[7,8,10,12–15] The modeling used in the present study followed these studies and is not novel here.

Mass transport and current distribution

Mass transport in the electrolyte is governed by the Nernst–Planck equation (eq.1.1) and the equation of mass conservation (eq.1.2):

$$\boldsymbol{N}_j = -z_j u_j F c_j \nabla \phi_l - D_j \nabla c_j + c_j \boldsymbol{v} \tag{1.1}$$

$$\frac{\partial c_j}{\partial t} + \nabla \cdot \boldsymbol{N}_j = 0 \tag{1.2}$$

where $\boldsymbol{N}_j$, z_j, u_j, c_j, and D_j are the mass flux, valence, mobility, concentration, and diffusion coefficient of species j, respectively. ϕ_l is the potential in the electrolyte, $\boldsymbol{v}$ is the velocity vector of the electrolyte, and F is the Faraday constant. There are no homogeneous reactions in the electrolyte. Current density in the electrolyte is described as sum of the charge flux of ionic species (eq.1.3) and

governed by current conservation (eq.1.4):

$$\boldsymbol{i}_l = -F^2 \nabla \phi_l \sum z_j{}^2 u_j c_j - F \sum z_j D_j \nabla c_j \tag{1.3}$$

$$\nabla \cdot \boldsymbol{i}_l = 0 \tag{1.4}$$

where $\boldsymbol{i}_l$ is the current density vector in the electrolyte. The potential distribution only in the electrolyte was considered because the potential gradient in the copper electrode is significantly smaller than that of the electrolyte.

The composition of the electrolyte solution used in simulations was $CuSO_4$ 0.76 mol dm^{-3} and H_2SO_4 1.94 mol dm^{-3}, and the temperature was uniform at 338.15 K (65 ºC). These conditions were selected with reference to industrial operations.[1] The electrolyte was assumed to be free of impurity ions, and the effects of impurity ionic components, such as Ni^{2+}, were not addressed in the present study. The cupric ion Cu^{2+}, hydrogen sulfate ion HSO_4^-, and hydronium ion H_3O^+ (hereafter H^+) were regarded as chemical species in the electrolyte. In the strongly acidic solution of pH < 0 used in copper electrorefining, the majority of sulfate ions exist as protonated HSO_4^-.[16] Therefore, all sulfate ions in the system were treated as HSO_4^-. Although Cu^{2+} forms $CuSO_4$(aq) complexes with SO_4^{2-} in some proportions,[16] for simplicity, these complexes were not considered, and all were treated as Cu^{2+} aquo ions. Furthermore, for the simplicity of the model, the activity of the ions was assumed to be equal to the molar concentration. The initial concentrations of Cu^{2+} and HSO_4^- were obtained from mass conservation, assuming that $CuSO_4$ and H_2SO_4 completely dissociated into Cu^{2+}, HSO_4^-, and H^+. The concentration of H^+ was selected to satisfy electroneutrality at each time and position.

The diffusion coefficients of each species were selected by correcting for electrolyte viscosity and a temperature of 338.15 K based on these values at 25 ºC (298.15 K) in dilute aqueous solutions[17] using

the Stokes–Einstein equation (eq.1.5):

$$D_j = \frac{kT}{6\pi r_j \mu} \propto \frac{T}{\mu} \quad (1.5)$$

where k is the Boltzmann constant, T is the absolute temperature, r_j is the Stokes radius of species j, and μ is the viscosity of the electrolyte. Mobilities were selected from diffusion coefficients using the Nernst–Einstein equation (eq.1.6):

$$u_j = \frac{D_j}{RT} \quad (1.6)$$

where R is the gas constant. Table 1.1 shows the values of the diffusion coefficient and mobility for each species used in simulations.

Table 1.1 Diffusion coefficient D and mobility u of each species, polarization characteristics, and electrolyte properties used in simulations.

Parameter	Value	Parameter	Value
D_{Cu2+}	8.49×10^{-6} cm^2 s^{-1}	Exchange current density i_0	150 A m^{-2}
D_{HSO4-}	1.65×10^{-5} cm^2 s^{-1}	Anodic symmetry factor $(1-\alpha)n$	1.3
D_{H+}	1.11×10^{-4} cm^2 s^{-1}	Cathodic symmetry factor αn	0.7
u_{Cu2+}	3.02×10^{-9} cm^2 mol J^{-1} s^{-1}	Initial electrolyte density	1.20 g cm^{-3}
u_{HSO4-}	5.86×10^{-9} cm^2 mol J^{-1} s^{-1}	Electrolyte viscosity μ	0.859 mPa s
u_{H+}	3.93×10^{-8} cm^2 mol J^{-1} s^{-1}		

Electrode kinetics

The electrochemical reaction rate for copper deposition and dissolution is expressed by the concentration-dependent Butler–Volmer equation (eq.1.7):

$$i_{\mathrm{B.V.}} = i_0 \left[\exp\left(\frac{(1-\alpha)nF}{RT}\eta\right) - \frac{c_{\mathrm{Cu^{2+},surface}}}{c_{\mathrm{Cu^{2+},bulk}}} \exp\left(\frac{-\alpha nF}{RT}\eta\right) \right] \quad (1.7)$$

where i_0 is the exchange current density, n is the electron number (= 2), and α is the symmetry factor. $c_{Cu^{2+},surface}$ is the Cu^{2+} concentration at the electrode surface and $c_{Cu^{2+},bulk}$ is that at the bulk solution. The initial Cu^{2+} concentration in the bulk electrolyte (0.76 mol dm^{-3}) was used as $c_{Cu^{2+},bulk}$. η is the overpotential at the electrode-electrolyte interface and is obtained together with the potential distribution in the electrolyte under the boundary condition that the total current across the entire electrode is constant.

In copper electrorefining, glue, thiourea, and chloride ions, each of which has a different function,[1] are generally added to the electrolyte to increase the smoothness of deposits. In the present study, the presence and effects of these additives were not explicitly examined; however, the polarization characteristics measured in the electrolyte containing these additives were used to indirectly reflect these effects. The exchange current density and anodic and cathodic symmetry factors shown in Table 1.1 were obtained by fitting the polarization curve measured with the electrolyte containing these additives that simulates industrial electrolyte compositions.[5]

Fluid dynamics

Laminar flow is assumed, and fluid dynamics are governed by the Navier–Stokes equation (eq.1.8) and continuity equation (eq.1.9) for incompressible fluid:

$$\rho \frac{\partial \boldsymbol{v}}{\partial t} + \rho(\boldsymbol{v} \cdot \nabla)\boldsymbol{v} = -\nabla p + \mu \nabla^2 \boldsymbol{v} + \rho \boldsymbol{g} \quad (1.8)$$

$$\rho \nabla \cdot \boldsymbol{v} = 0 \quad (1.9)$$

where ρ is the density of the electrolyte, p is pressure, and $\boldsymbol{g}$ is gravitational acceleration. In the present study, neither circulating flow nor forced convection was examined, only natural convection driven by the concentration distribution near the electrodes was investigated.

The properties of the electrolyte were assessed based on regression equations for the measured values. Density was evaluated as follows from Price and Davenport:[18]

$$\rho[\mathrm{g\ cm^{-3}}] = 1.022 + 10^{-3}(2.24 M_{\mathrm{Cu}} c_{\mathrm{Cu2+}}[\mathrm{mol\ dm^{-3}}] + 0.55 M_{\mathrm{H2SO4}} c_{\mathrm{H2SO4}}[\mathrm{mol\ dm^{-3}}] - 0.58T[^{\circ}\mathrm{C}]) \quad (1.10)$$

where M_{Cu} and $M_{\mathrm{H_2SO_4}}$ are the formula weights of Cu and H_2SO_4, respectively; $c_{\mathrm{Cu^{2+}}}$ is the concentration of Cu^{2+} ions, and the variable concentration for each time and position were used to simulate natural convection; $c_{\mathrm{H_2SO_4}}$ is the concentration of free acid, and the constant value of 1.94 mol dm^{-3} was used. Viscosity was assessed for the prepared composition from the regression equation by Price and Davenport[18] and was treated as a constant to simplify the model. Table 1.1 shows the initial density for the prepared composition and viscosity used in simulations.

Particle Tracing

Particle transport in the electrolyte is governed by Newton's second law (eq.1.11):

$$\left(\frac{4}{3}\pi {r_{\mathrm{p}}}^3 \rho_{\mathrm{p}}\right)\frac{d\boldsymbol{v}_{\mathrm{p}}}{dt} = \boldsymbol{F} \quad (1.11)$$

where r_{p} and ρ_{p} are the radius and density of the particles, $\boldsymbol{v}_{\mathrm{p}}$ is the velocity vector of each particle, and $\boldsymbol{F}$ is the resultant force acting on each particle. The particle shape was assumed to be spherical. As the forces acting on each particle, the drag force expressed by Stokes' law for spherical particles[19] and the gravity and buoyancy forces were considered as follows:

$$\boldsymbol{F} = 6\mu\pi r_{\mathrm{p}}\left(\boldsymbol{v}-\boldsymbol{v}_{\mathrm{p}}\right) - \frac{4}{3}\pi {r_{\mathrm{p}}}^3\left(\rho_{\mathrm{p}} - \rho\right)\boldsymbol{g} \quad (1.12)$$

In the present study, the effects of particle transport on convection were not considered. It is also important to note that collisions or interactions

between particles, such as van der Waals interactions and electrostatic interactions, were not considered.

Difficulties are associated with uniquely assessing the apparent density of slime particles because anode slime is a complex mixture of multiple chemical species and contains pores. Therefore, two extreme cases of particle characteristics were compared in the range of the densities of chemical species typically contained in anode slime: a density of 5 g cm^{-3} and diameter of 5 μm (clearly suspending particles), and a density of 8 g cm^{-3} and diameter of 50 μm (clearly settling particles). As a reference, the densities of As_2O_3, AgCl, Cu_2Se, Cu, and Ag are 3.76, 5.56, 6.84, 8.96, and 10.49 g cm^{-3}, respectively.

Geometry and mesh

The size of the cell was 200 × 50 × 25 mm, and the area of both the anode and cathode were 150 × 50 mm (Figure 1.3(a)). Spacing between the anode and cathode surfaces was set to 25 mm to simulate an industrial arrangement.[1] To simulate the growth process, nodules of three different sizes (10, 15, and 20 mm) with a diameter/length ratio of one were placed at the center of the cathode surface. Geometry was divided in the vertical plane at the center of the electrode, on which symmetric boundary conditions were set, and calculations were performed on half of the area to reduce computational costs.

Figure 1.3(b) shows a typical mesh division of the geometry by tetrahedral elements. To resolve the concentration and convection boundary layers, relatively thin meshes were set on the anode, cathode, including the nodule, and cell bottom surfaces.

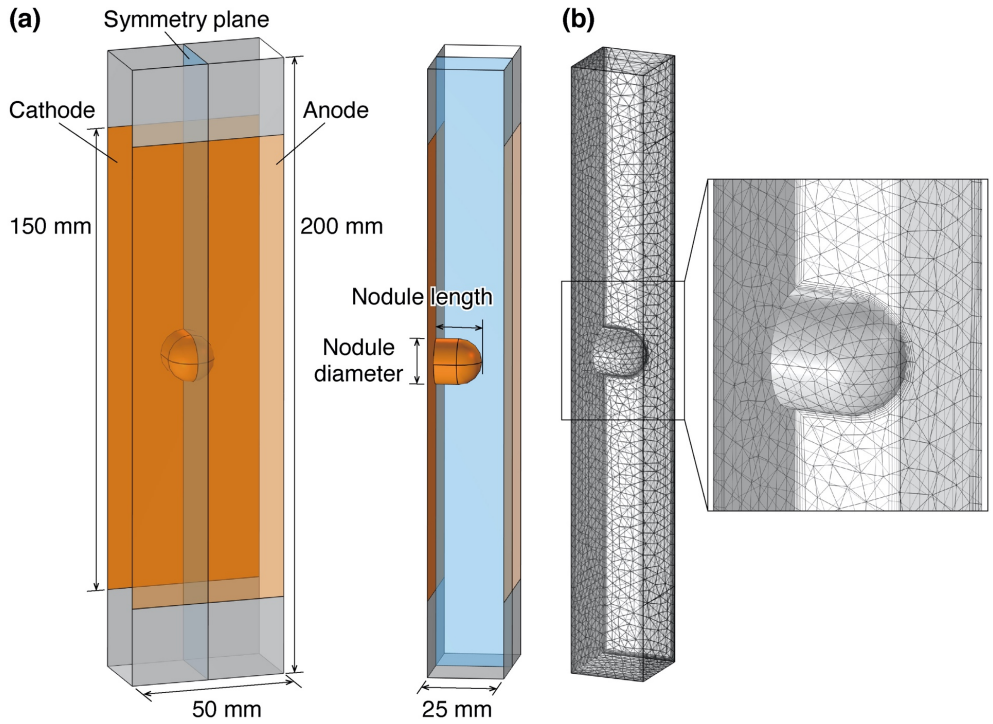

Figure 1.3 Geometry of a copper electrorefining cell used in the simulation. (a) Alignment of electrode pairs with a nodule and (b) meshes of the cell.

Boundary conditions

There was no current or mass flux in the normal direction on the cell walls or on the symmetry plane, except for the electrode surfaces. At the electrode surfaces, the current density of ion transport in the electrolyte was connected to that of the electrochemical reactions, as well as to the consumption and supply of Cu^{2+} ions. Total current across the entire electrodes was set to a constant so that the average current density was 350 A m^{-2} for the projected area of the electrode, referring to industrial operating conditions.[1] The electrode surfaces and the cell bottom were set as no-slip boundaries, and other surfaces were set as slip boundaries. In particle transport, particles in contact with the cathode surfaces were set to stop moving (freeze), while those in contact with other boundaries rebounded.

Calculations

For simplicity, it was assumed that electrode geometry did not change and remained the same as the initial shape, even though copper deposition and dissolution occurred. As a preliminary study, calculations were performed from the initial state, where the electrolyte was stationary throughout the cell, until 60 min. Convection fluctuated dynamically for the first several minutes after the start of electrolysis. After approximately 10 min of electrolysis, convection fluctuations became small and settled to a mostly constant velocity distribution. In addition, after 10 min, convection velocity decayed slowly with time. Therefore, the state after 10 min was regarded as a pseudo-steady state for the following discussion. With the uniform deposition of Cu at a current density of 350 A m^{-2}, the thickness of the deposit was approximately 7.7 μm in 10 min, and the above approximation is valid assuming that the electrode geometry does not change.

In calculations of particle transport, 1000 particles were placed in a uniform distribution throughout the electrolyte 10 min after the initiation of electrolysis. The initial velocity of each particle was given by the electrolyte velocity at each position. Particle transport behavior under quasi-steady convection was simulated after 10 min of electrolysis.

1.3. Results and discussion

1.3.1. Experimental analysis of nodules

Figures 1.4(a,b) show the contents of impurity elements in the upper and lower pieces of two round-shaped nodules (Nodule I and II) cut as shown in Figure 1.2(a). Figures 1.4(c,d) show the impurity contents in pieces sampled from three different locations for two sheets of non-nodulous electrolytic copper A and B. Any sample of electrolytic copper contained up to 13 ppm (mg/kg) Ag, 6 ppm S, and at most 1 ppm of the other elements (Se, As, Pb, Ni, Sb, and Sn), with no marked differences being observed between the sampled locations. In Nodules I and II, impurity contents in the lower half were similar to those in electrolytic copper, while the contents of Ag, Se, As, Pb, Ni, and S were higher in the upper half than in either the lower half or non-nodulous electrolytic copper; therefore, these impurities were unevenly distributed in the upper half of the nodules.

The Ag content in non-nodulous electrolytic copper is considered to be electrodeposited from the electrolyte. On the other hand, the Ag content in the upper half of the nodules is markedly higher than that of non-nodulous electrolytic copper, indicating that most of the Ag content in nodules is attributed to the included anode slime. It currently remains unclear whether Ag in slime is a metal or compound in the present study. It also contains some S, most likely from $PbSO_4$ slime inclusions and electrolyte residue remaining in the nodules. Since S is more abundant than Pb, the content of S is attributed not only to $PbSO_4$ slime, but also to the electrolyte residue. Even though components in the electrolyte residue were detected, most parts of the other impurity elements were attributed to included slime particles because the detected amounts of these elements were markedly higher than those in the electrolyte. Therefore, these results suggested that slime particles composed of

these elements were preferentially taken into the upper part of the nodules.

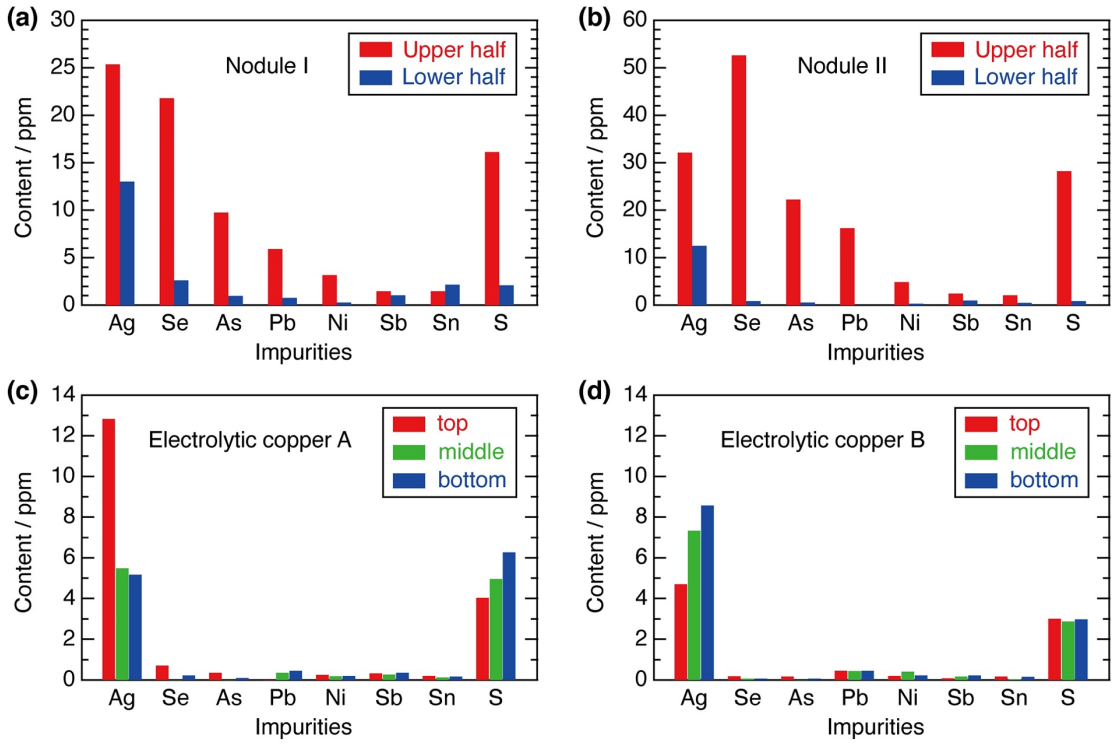

Figure 1.4 Contents of eight impurity elements measured by ICP-OES for (a,b) two different nodules I and II cut horizontally and for (c,d) top, middle, and bottom pieces of two non-nodulous electrolytic copper A and B. All samples were obtained from the industrial copper tank house.

The other three nodules (Nodules III, IV, and V) were cut into upper and lower pieces, and each piece was further cut into five smaller pieces from the root to the tip of the nodule as shown in Figure 1.2(b). In all nodules, impurity contents were more likely to be unevenly higher in the upper series than in the lower series (Figures 1.5(a–i)), similar to Nodules I and II. Nodule III showed the highest contents of all elements in the 5th piece from the left in both the upper and lower series, which was due to the high content of particles in the spherical protrusion that formed at the tip of the nodule (Figure 1.5(j)). In this case, Ag, Se, As, S, and Ni were detected by the EDX spectra of these particles, suggesting that these particles were derived from anode slime. In Nodules IV and V, impurity contents were generally higher in the pieces in the upper half and the roughness of the original surface was also higher. A number of the particles included were detected at the cut surfaces of these nodules (Figures 1.5(k,l)). The inclusion of slime particles during copper deposition may have increased impurity contents in the corresponding pieces and changed the macroscopic shape of the nodules.

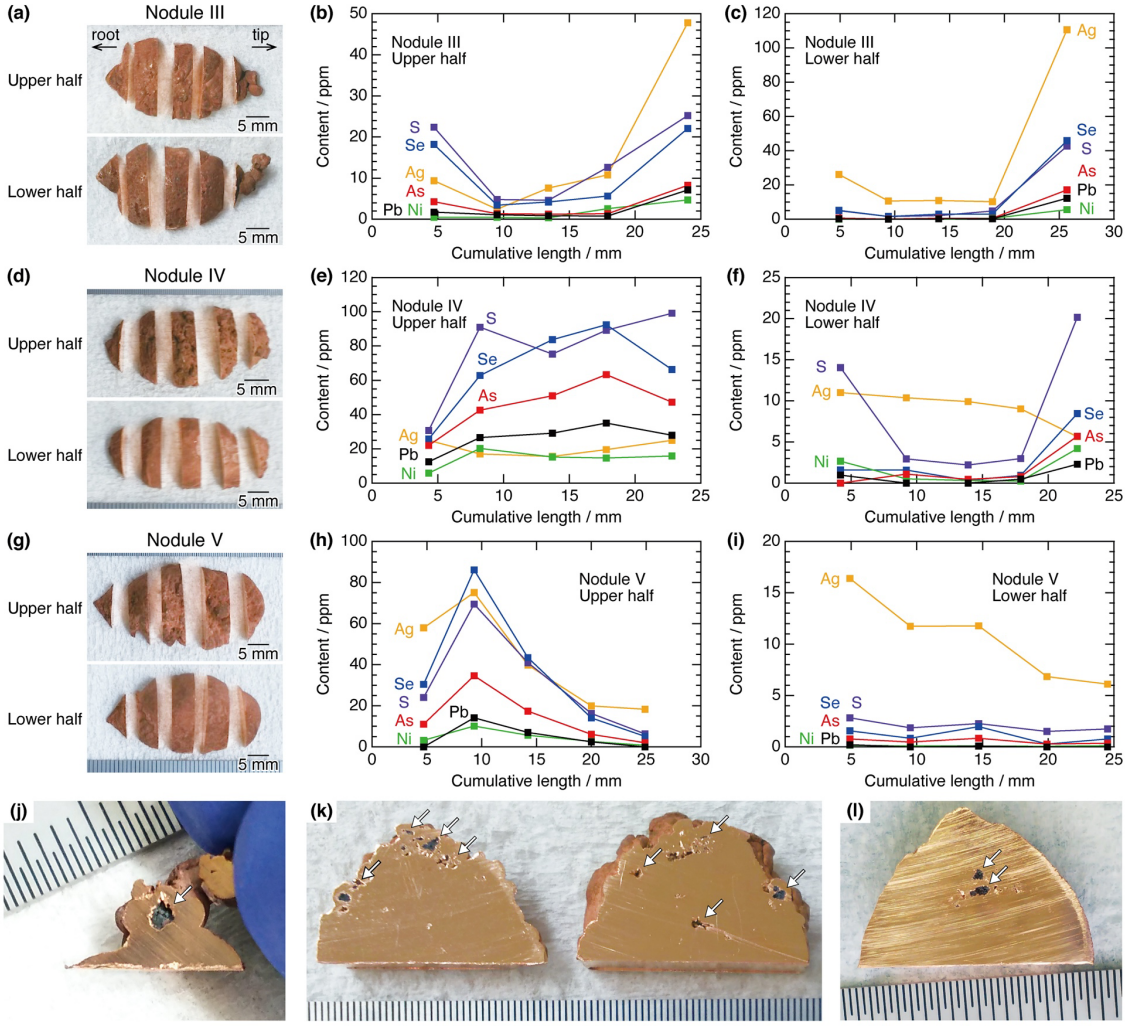

Figure 1.5 (a,d,g) Photographs of three different nodules cut horizontally and in the growing direction. The contents of six impurity elements measured by ICP-OES in each series of the (b,e,h) upper half and (c,f,i) lower half of the three nodules. (j,k,l) are the cut surfaces at the tip (i.e., 5th) of the lower half of Nodule III, the 3rd and 4th pieces from the root of the upper half of Nodule IV, and the 2nd piece from the root of the upper half of Nodule V, respectively. Particles included in the nodules are indicated by white arrows.

Figure 1.6(a) shows photographs and optical images of the cross-section of another round-shaped nodule. A crystalline morphology consisting of fine grains was observed near the root of the nodule (a-1), and fibrous structures (a-2,3) and coarse grains (a-4,5) were observed towards the tip of the nodule. These morphologies were similar to that of electrolytic copper with non-nodulous growth.[20,21] An unoriented dispersion (UD) structure formed near the root of the nodule, and as the nodule grew, the field-oriented texture (FT)-type and basis-oriented reproduction-type structure successively formed. Crystallographic investigations of nodules have been performed.[22,23] Shojaei *et al*. showed that the structure of electrodeposited copper changed from the FT to UD structure, resulting in the formation of nodules with the UD structure.[23] In the present study, a similar UD structure was noted at the root of the nodule. Figure 1.6(b) shows a unique crystalline morphology that grew radially around a slime particle found near Figure 1.6(a-2). In the region growing radially from the particle, the same FT structure as that in the original region also formed before the particle was attached. This result suggests that the inclusion of particles did not change the type of structure that formed.

Figure 1.6(c) shows a typical cross-section of electrolytic copper accompanying a growing nodule, which was obtained from the industrial tank house. As already discussed, the upper half of the nodule contained a number of slime particles and, in this case, spherical irregular deposits formed around each particle. These results indicate that the slime particles included in the deposits changed the growing direction of the crystal structure and then promoted three-dimensional growth, resulting not only in the starting point for nodule outbreaks, but also the formation of spherical or rough irregular deposits, particularly on the upper surface of the nodule.

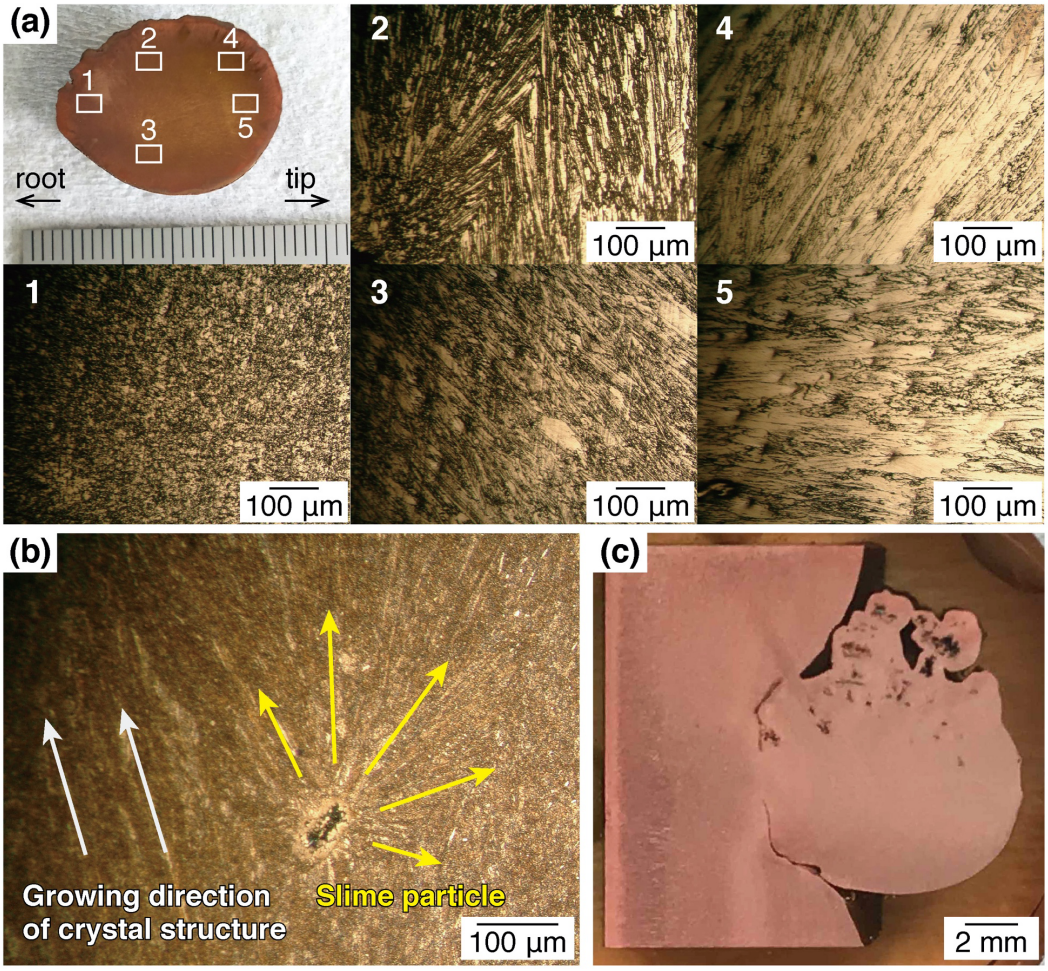

Figure 1.6 Cross-sectional images of nodules obtained from the industrial copper tank house. (a) Photograph and optical images of the electrodeposited crystalline morphology of the nodule and (b) an image around a slime particle included near (a-2). (c) A cross-sectional photograph of typical electrolytic copper accompanying a nodule.

1.3.2. Numerical simulations of the tertiary current distribution

The color profile in Figure 1.7 represents the absolute value of the simulated local current density on electrode surfaces, and streamlines represent current flux. Current density was high at the upper most and lower most edges of the electrodes and at the tip of the nodule, at which the current density vector was concentrated in a circular manner, while it was low at the root of the nodule. This current distribution around the nodule was qualitatively consistent with the previous study based on the secondary current distribution without considering mass transport.[5]

When assessed in a series of analyses with the comparative use of the secondary and tertiary current distribution models, the geometry of the nodule and the polarization characteristics of the electrode–electrolyte interface mainly influenced the current concentration at the nodule, while diffusion and convection influenced more weakly in comparison. This result was attributed to the average current density (350 A m^{-2}) being smaller than the cathodic limiting current density (1074 A m^{-2} for a flat cathode)[5] and the diffusion layer thickness at the nodule tip being smaller than that at the cathode plate, which promotes mass transport. Although a more accurate current distribution may be obtained with the tertiary current distribution, the secondary current distribution was concluded to be sufficient to obtain an approximate current distribution.

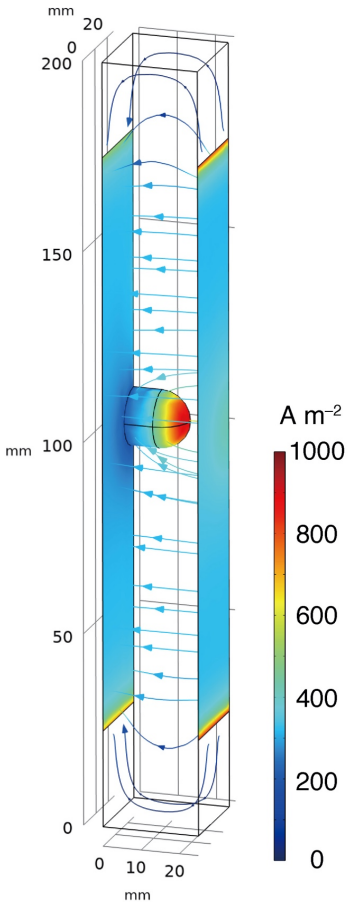

Figure 1.7 Tertiary current distribution and current flux lines on electrodes with a 15-mm mimic nodule after 10 min of electrolysis.

Since the modeled cell was closed, in contrast to a real tank house, solutions with lower and higher concentrations accumulated only at the top and bottom of the cell according to their density, respectively (Figure 1.8(a)). A concentration diffusion layer with depleted or accumulated cupric ions formed in the vicinity of the cathode and anode, respectively (Figure 1.8(b)). The concentration profile is affected by the nodule diameter as seen from Figure 1.8(b). Figure 1.8(c) shows the concentrations profiles along the perpendicular distance from the surface at positions A–E shown in Figure 1.8(b). The diffusion layer thickness was smaller at the tip of the nodule than at the planar part of

the cathode. This may be because the tip of the nodule, which was taller than the thickness of the natural convection layer (0.5–1.0 mm of the planar part), broke through the natural convection layer that developed along the surrounding cathode surface. In typical natural convection along a vertical planar cathode, a solution with diluted cupric ions flows in from upstream (bottom of the cathode), and, thus, natural convection develops and the diffusion layer thickness increases towards downstream (upward).[24–26] At the tip of the nodule, the thickness of the diffusion layer became smaller than that at the planar part of the cathode because dilute solution inflow from the surrounding decreases, in contrast to the planar part of the cathode.

It is important to note that the diffusion layer in the upper part of the nodule extended more towards the solution, as shown in Figure 1.8(b) and A and B in Figure 1.8(c). Such dilute regions of cupric ions were formed by upward natural convection flowing along the sides and front surfaces of the nodule and then detaching from the upper surface. The thickness of the diffusion layer at the tip of nodule was similar for the three nodule sizes (Figure 1.8(d)), whereas the concentration at the surface decreased with increases in the nodule size because larger nodules were associated with higher current concentrations, even in the same convection environment. In electroplating, the diffusion layer formed is generally uniform (conformally) along a convex deposition surface if the convex is sufficiently larger than the diffusion layer thickness, and diffusion flux does not differ depending on the position. In contrast, around a nodule placed on a vertical planar cathode, the concentration distribution described above was formed by natural convection because the nodule (convex) sufficiently protruded and was larger than the diffusion layer thickness.

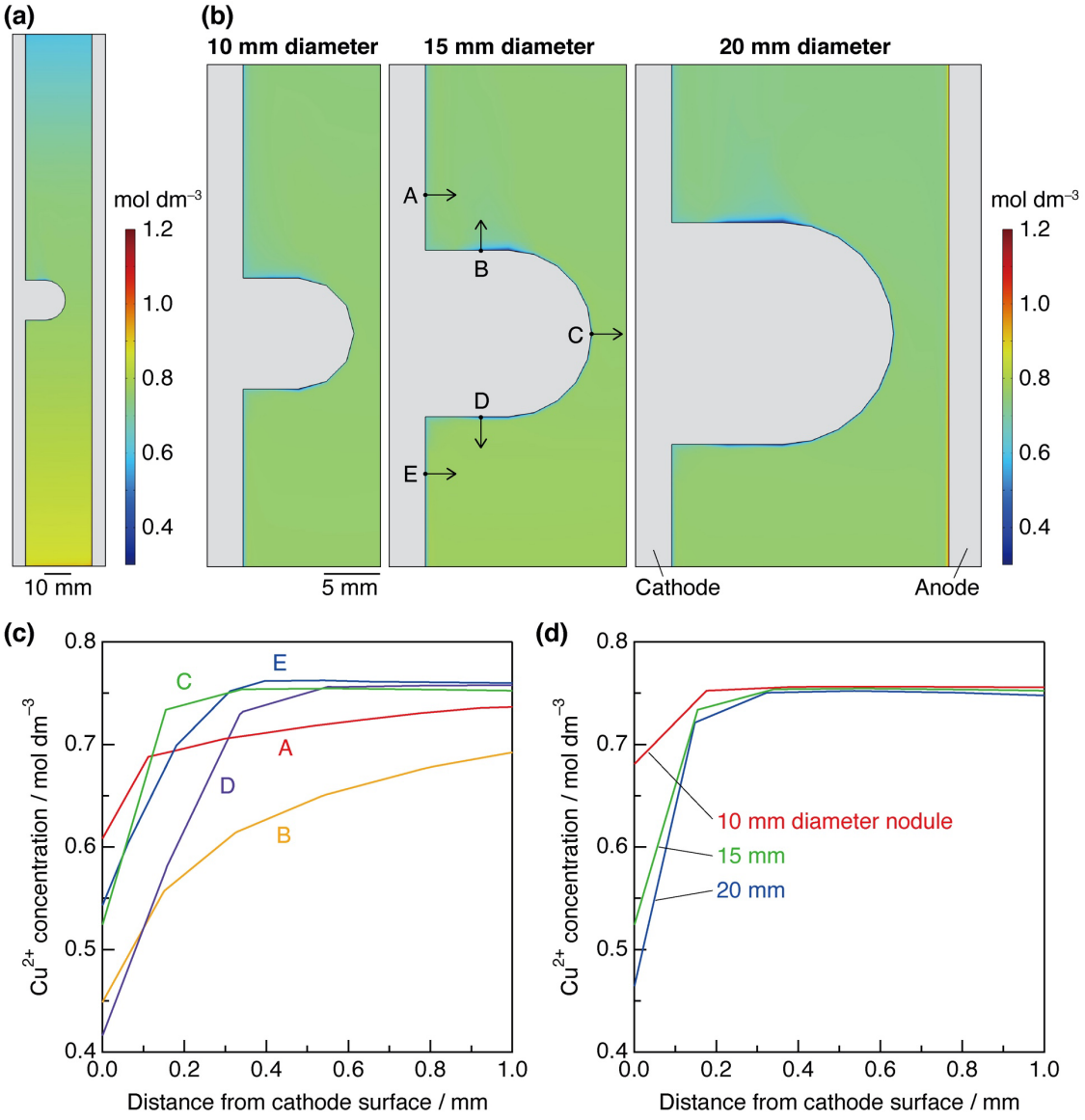

Figure 1.8 Simulated concentration distributions of cupric ions after 10 min of electrolysis using cathodes with mimic nodules with diameters of 10–20 mm. (a) Concentration distribution in the symmetry plane of the entire cell with a 15-mm mimic nodule, (b) magnified views around nodules of each size, (c) concentration profiles along the distance from the cathode surface at positions A–E for the 15-mm mimic nodule, and (d) that at the nodule tip (position C) for nodules of each size.

Upward and downward natural convection with peak velocities of 3–4 mm s^{-1} was simulated in the vicinity of the cathode and anode, respectively, depending on the distance from the top and bottom of the electrodes (Figure 1.9(a)). Such velocity profiles were reasonable with experimental observations of natural convection.[24,27] Strong upward natural convection and the associated vortex formed above each nodule with three different diameters (Figure 1.9(b)). This upward flow was formed by the dilute solution flowing upward on the sides and front surfaces of the nodules and detaching from the upper surface. Figure 1.9(c) shows the velocity distributions of the 15-mm nodule in four different planes parallel to the planar cathode. Near the root of the nodule (x = 3 mm), upward convection that developed along the planar cathode collided with the nodule and separated to the left and right sides of the nodule to circumvent the nodule. Concomitant downward convection was observed just above the nodule, slightly to the side of the upward flow, forming a vortex. These results suggest that the nodule did not only become an obstacle in natural convection that developed along the planar cathode, but it also formed strong upward flow associated with a plume-like vortex in the stagnant bulk solution.

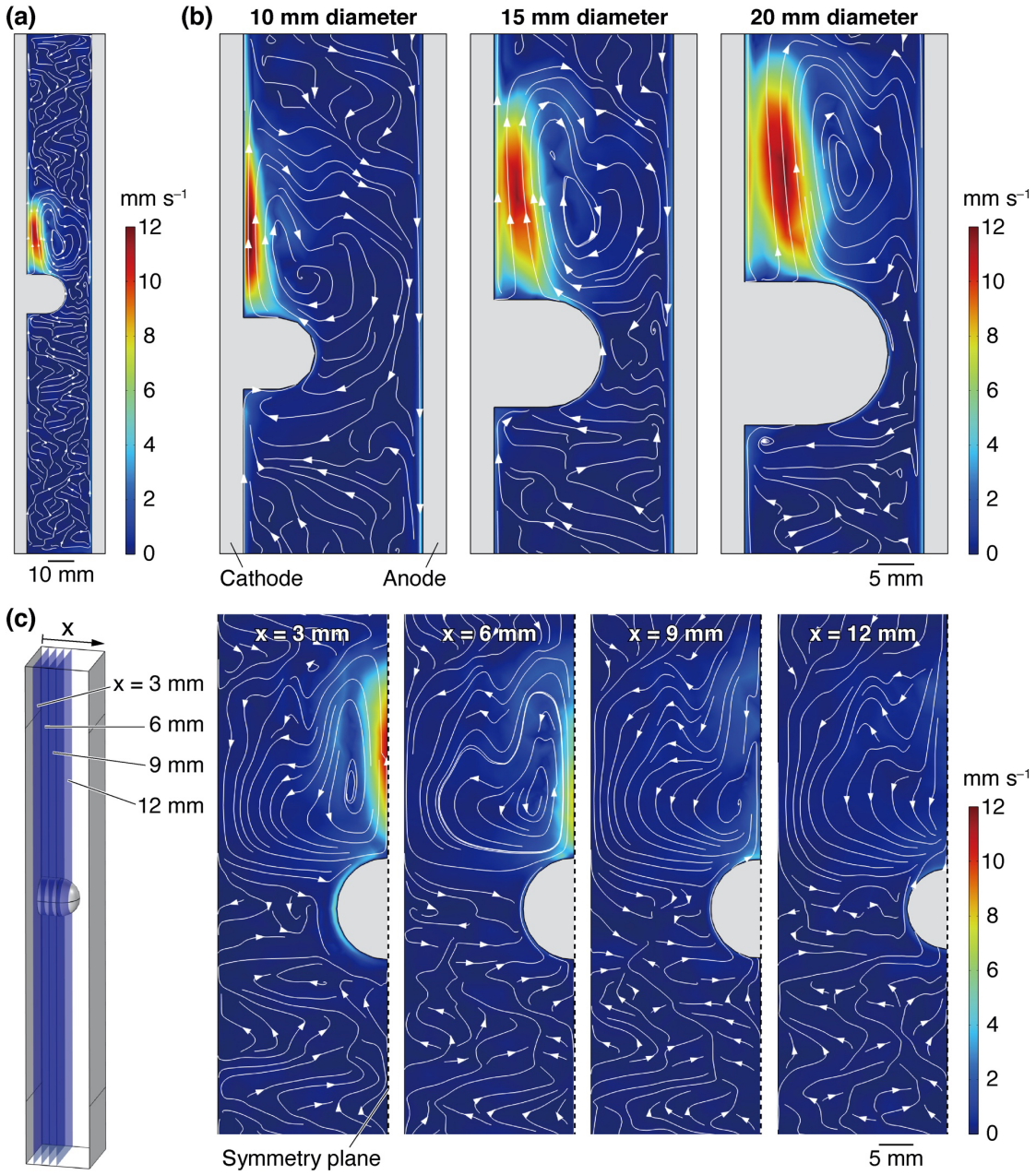

Figure 1.9 Simulated convection velocity distributions in the electrolyte after 10 min of electrolysis. (a) Velocity distribution in the symmetry plane of the entire cell with a 15-mm mimic nodule, (b) magnified views around each mimic nodule with diameters of 10–20 mm, and (c) velocity distributions in four different planes parallel to the planar cathode with a 15-mm mimic nodule. The color profiles show the absolute values of the velocity vector.

1.3.3. Numerical simulations of particle transport

Figure 1.10 shows the velocity vectors and trajectories of each particle with a diameter of 5 μm and density of 5 g cm^{-3} after 11 min of electrolysis (1 min after particles were placed). Trajectories represent the movement of these particles for one minute after their placement. The particles moved upward and downward near the cathode and anode, respectively. In the upper part of the nodule, upward flow blew up the particles. Furthermore, the particles descended downward along the vortex at the periphery, and then returned to the upper part of the nodule, where they moved along the vortex to repeat the circulation. Particles were suspended in the bulk solution distant from the nodule and only slightly moved.

Regarding particles with a diameter of 50 μm and density of 8 g cm^{-3}, particles immediately settled in the solution, and 5 s after particles were placed, the settling velocity had reached the terminal velocity of 2.6 mm s^{-1} in the bulk solution, which is consistent with previous findings.[28,29] Only particles initially located just above the nodules settled towards the nodules and attached to the upper surface while slightly shifting the settling direction due to upward flow. In any case, these easily settleable particles are assumed to sink directly towards the bottom of the cell as soon as they are released from the anode surface, and few remain suspended in the solution until they attach to the nodule. Therefore, the potential of these settleable particles attaching to the nodule is low.

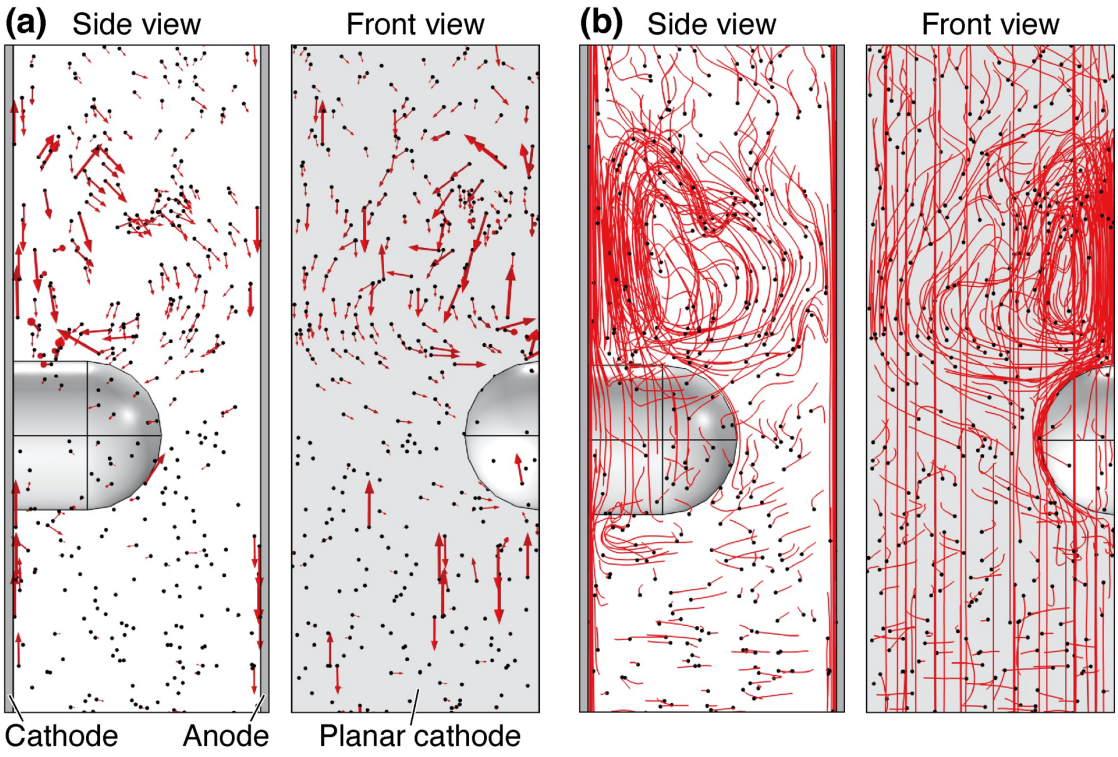

Figure 1.10 Simulated transport behavior of impurity particles with a diameter of 5 μm and density of 5 g cm^{-3} carried by natural convection after 11 min of electrolysis (1 min after particles were placed) for a 15-mm mimic nodule. Side and front views of (a) the velocity vectors and (b) trajectories of each particle (black dots). The magnitude of the arrows in (a) represents the velocity vector of each particle in logarithm. The range of the particle velocity simulated was 0–3.6 mm s^{-1}. Note that the trajectories appear to overlap in the depth direction.

1.3.4. Mechanism of nodular growth with the inclusion of impurity particles

Figure 1.11 schematically illustrates the process in which suspended particles are transported and taken inside the nodule, especially in its upper part. Current is concentrated on the nodule due to its geometry, and cupric ions are consumed at a higher rate. The diluted electrolyte

with cupric ions consumed on the nodule surface flows upward, forming an additional upward natural convection separated from convection in the vicinity of the planar cathode and the associated plume-like vortex above the nodule.

Suspended particles are blown upward and repeat the circulation motion above the nodule along the vortex. This circular motion is considered to increase the frequency of particle collisions and inclusions in the upper part of the nodule because particles with momentum frequently come towards the top surface of the nodule. The particles that collide with the nodule surface are immediately taken into the nodule by the progression of electrodeposition. Relatively settleable suspended particles of a slightly larger diameter or higher density are taken into the nodule by sinking accidentally during their circulation and entering the stagnant region near the upper surface of the nodule, which is in the shadow of the upward flow. In these pathways, particles are preferentially included in the upper side of the nodule. Easily-settleable particles of a larger diameter or higher density, such as metallic copper and silver, which are accidentally transported to the vicinity of the cathode, may sink in the solution and land on the upper surface of the nodule despite upward flow. However, few particles behave in this manner.

Particle motion becomes more complex at the edges and bottom of the operating real tank house, where circulating flow throughout the bath may affect as particles are wound up. The present study showed particle behavior for most of the inter-electrode region, where mild natural convection is dominant. Further studies such as *in situ* observations of particle motion are needed to clarify the process of the transport and inclusion of particles into nodules.

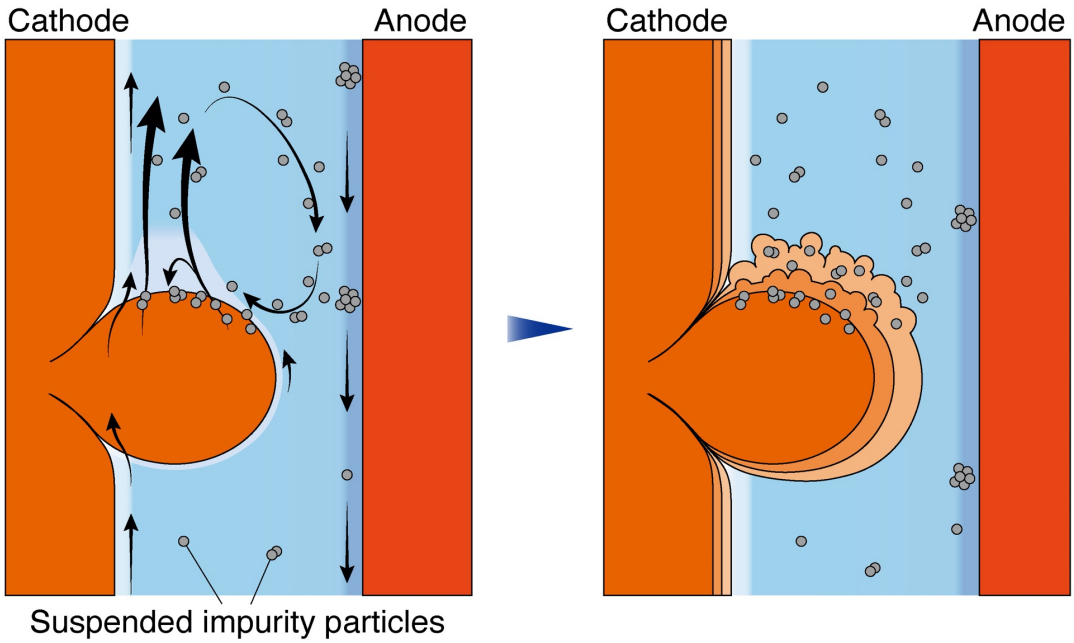

Figure 1.11 Schematic illustrations of the process in which suspended particles are transported around the nodule by natural convection and are taken inside the upper part of the nodule during electrodeposition.

Impurity particles are not only included in deposited copper, but also change the growth direction of crystal structures to promote fast three-dimensional growth. These included particles eventually cause rough morphologies on the nodule, such as grainy roughness on the upper part and vertically stacked shape as shown in Figure 1.12, taken at JX Nippon Mining & Metals Corporation. Experimental results revealed that particle inclusions resulted in fast three-dimensional growth and irregular deposits, and simulations showed that particles transported by the convection vortex were included into the upper part of the nodule. The present study clarified the growth-promoting mechanism by particle inclusion through the combination of experiments and simulations.

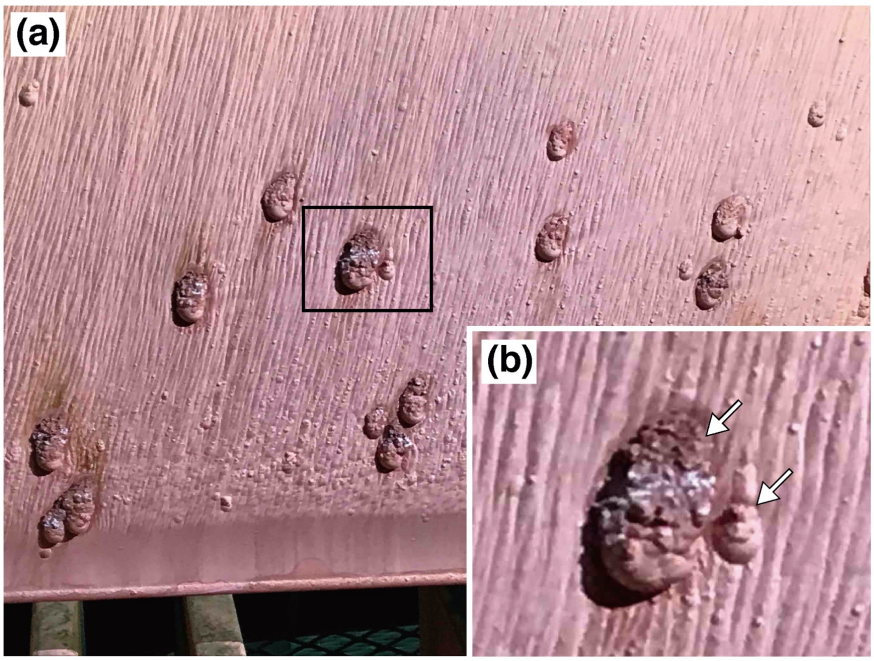

Figure 1.12 Photograph of electrolytic copper and nodules in the industrial copper tank house. (b) is an enlarged view of the open square shown in (a). White arrows in (b) indicate grainy roughness formed on the upper part of the nodule and new nodules stacked vertically on the upper part of the initial nodule.

The proposed mechanism in the present study suggests that suppressing nodule growth can be achieved by removing suspended slime particles from the electrolyte. To achieve this, it is recommended to filter the electrolyte bleed stream to trap finer slime particles. However, it is important to note that finer filtration requires extra energy and may lead to filter clogging. Therefore, the effectiveness of this proposal must be evaluated based on the operational performance of the tank house.

Nodules have a higher impurity content than non-nodulous electrolytic copper because they contain many impurity particles, such as slime. If nodules remain attached to the final electrolytic copper products, the copper grade may not be uniform and valuable metals,

such as silver, gold, and platinum group metals, contained in slime may be lost from the refining system. By removing nodules from electrolytic copper and placing them into the casting process, the uniformity of the copper grade and the recovery efficiency of valuable metals will be improved.

1.4. Conclusions

The nodular growth process with the inclusion of impurity particles in copper electrorefining was investigated by experimental analyses of impurity contents inside the nodules and numerical simulations using the tertiary current distribution. The contents of impurity elements were higher in the upper half of the nodules than in electrolytic copper with non-nodulous growth. Slime particles were preferentially included in the upper part of the nodule. Impurity particles are taken into a nodule by colliding preferentially with the upper half of the nodule as they circulate along the convection vortex that emerges above the nodule. Impurity particles attached to the nodule surface change the growth direction of crystal structures, and eventually produce granular irregularities and buds of new nodules on the upper part of the initial nodule.

References

1. M. E. Schlesinger, M. J. King, K. C. Sole, and W. G. Davenport, in *Extractive Metallurgy of Copper*, edited by M. E. Schlesinger, M. J. King, K. C. Sole, and W. G. Davenport, 5th Ed. (Elsevier, Oxford, 2011), pp. 251–280.
2. T. N. Andersen, C. H. Pitt, and L. S. Livingston, *J. Appl. Electrochem.*, **13**(4), 429–438 (1983).
3. J. E. Dutrizac and T. T. Chen, in *4th International Confonference COPPER 99-COBRE 99* (1999), pp. 383–403.
4. K. Adachi, Y. Nakai, A. Kitada, K. Fukami, and K. Murase, in *Rare Metal Technology 2018*, edited by H. Kim, B. Wesstrom, S. Alam, T. Ouchi, G. Azimi, N. R. Neelameggham, S. Wang, and X. Guan (Springer Cham, 2018), pp. 215–222.
5. K. Adachi, Y. Nakai, S. Mitsuno, M. Miyamoto, A. Kitada, K. Fukami, and K. Murase, *J. MMIJ*, **136**(2), 8–13 (2020).
6. Y. Nakai, K. Adachi, A. Kitada, K. Fukami, and K. Murase, in *Rare Metal Technology 2018*, edited by H. Kim, B. Wesstrom, S. Alam, T. Ouchi, G. Azimi, N. R. Neelameggham, S. Wang, and X. Guan (Springer Cham, 2018), pp. 319–323.
7. W. Zeng, M. L. Free, and S. Wang, *ECS Trans.*, **72**(22), 23–42 (2016).
8. W. Zeng, M. L. Free, J. Werner, and S. Wang, *J. Electrochem. Soc.*, **162**(14), E338–E352 (2015).
9. W. Zeng, J. Werner, and M. L. Free, *Hydrometallurgy*, **156**, 232–238 (2015).
10. W. Zeng, S. Wang, and M. L. Free, *J. Electrochem. Soc.*, **163**(5), E111–E122 (2016).
11. J. M. Werner, W. Zeng, M. L. Free, Z. Zhang, and J. Cho, *J. Electrochem. Soc.*, **165**(5), E190–E207 (2018).

12. W. Zeng, S. Wang, and M. L. Free, *JOM*, **69**(10), 1876–1887 (2017).
13. W. Zeng, G. Yi, S. Wang, and M. L. Free, *Hydrometallurgy*, **169**, 612–620 (2017).
14. W. Zeng, S. Wang, and M. L. Free, *J. Electrochem. Soc.*, **164**(9), E233–E241 (2017).
15. W. Zeng, S. Wang, M. L. Free, C.-J. Tang, R. Xiao, and Y. Liang, *J. Electrochem. Soc.*, **165**(14), E798–E807 (2018).
16. J. M. Casas, F. Alvarez, and L. Cifuentes, *Chem. Eng. Sci.*, **55**(24), 6223–6234 (2000).
17. D. R. Lide, (Ed.) *CRC Handbook of Chemistry and Physics*, 84th Ed. (CRC Press, Boca Raton, 2003).
18. D. C. Price and W. G. Davenport, *Metall. Trans. B*, **12**(4), 639–643 (1981).
19. R. Clift, J. R. Grace, and M. E. Weber, *Bubbles, Drops, and Particles* (Dover, New York, 2005), p. 35
20. B. Veilleux, A. M. Lafront, and E. Ghali, *J. Appl. Electrochem.*, **31**(9), 1017–1024 (2001).
21. H. Nakano, S. Oue, Y. Tsuyama, H. Fukushima, S. Kobayashi, and K. Tomioka, *J. MMIJ*, **127**(10–11), 662–666 (2011).
22. Z. Mubarok, I. Filzwieser, and P. Paschen, in *Proceedings - European Metallurgical Conference EMC 2005* (2005), pp. 109–122.
23. M. Reza Shojaei, G. Reza Khayati, S. Mohammad Javad Korasani, and R. Kafi Harnashki, *Eng. Fail. Anal.*, **133**, 105970 (2022).
24. Y. Awakura, Y. Takenaka, and Y. Kondo, *Electrochim. Acta*, **21**(10), 789–797 (1976).
25. Y. Awakura and Y. Kondo, *J. Electrochem. Soc.*, **123**(8), 1184–1192 (1976).
26. Y. Awakura, M. Okada, and Y. Kondo, *J. Electrochem. Soc.*, **124**(7), 1050–1057 (1977).

27. N. Lbl and R. H. Müller, *J. Electrochem. Soc.*, **105**(6), 346 (1958).
28. T. Kalliomäki, A. Aji, J. Aromaa, and M. Lundström, in *Proceedings of Copper 2019* (2019).
29. X. Ling, Z. H. Gu, and T. Z. Fahidy, *Can. J. Chem. Eng.*, **72**(4), 683–694 (1994).

Chapter 2

Surface Roughening and Growth-Promoting Effects of Nickel and Antimony on Nodules in Copper Electrorefining

2.1. Introduction

Nodulation of electrolytic copper is a critical issue that needs to be resolved for desirable copper electrorefining operations. Nodules that form on the electrolytic copper cathode subsequently grow and eventually reach the anode, causing partial short circuits. These accidental short circuits result in electrode pairs at which an electrolytic reaction does not occur despite the flow of current, which reduces current efficiency at 3% and requires extra energy consumption.[1] Nodulation also leads to the degradation of product quality due to the incorporation of impurities.[2] A more detailed understanding and the prevention of nodulation are important for advances in industrial copper electrorefining.

In the majority of studies on nodulation, the beginning of nodulation (e.g., less than 1–2 mm in height) has been an important topic to be elucidated and continues to be of interest. Slime particles adhering to the cathode are regarded as a serious cause of nodule outbreaks,[3,4] and the deviation of additives from their proper quantity ratio has also been reported to cause nodules.[5–8] Furthermore, a statistical analysis revealed that an increase in the ratio of current density to diffusion-limited current density was associated with a greater probability of nodule formation.[9] The correlation of overpotential and mass transfer on the surface morphology of the electrodeposited copper film has also been discussed extensively in a series of studies.[10–13] Pourgharibshahi *et al.* pointed out that the

metallographic and topographic transition in electrodeposited copper induced by the incorporation of micro-particles leads to nodule formation.[14]

On the other hand, the mechanisms by which nodules of 1–2 mm grow sufficiently large to reach the anode, which is separated from the cathode by 25–35 mm, in the industrial operation period have only recently been investigated.[2,15–18] Adachi *et al*. quantitatively evaluated the nodule growth rate in lab-scale electrolytic experiments and simulations of current distribution using several different nodule-mimicking protrusions that preliminarily attached to the planar cathode.[15–17] The threshold of the size of nodule buds that may lead to a short circuit within the operation period was estimated by considering the current concentration at the protrusion and rapid growth due to dendritic electrodeposition. Multiphysics simulations including ionic concentration distribution, convection, and particle transport in addition to current distribution are also effective tools for nodule growth analysis.[2,19]

Most of these basic studies on nodule growth were performed using simplified model electrolytes without dissolved impurity elements, such as nickel, iron, zinc, arsenic, antimony, and bismuth ions, which are released from crude copper anodes and accumulate in the electrolyte during industrial processes. Nowadays, one of the challenges in copper electrorefining is the operation with complicated electrolytes containing high levels of nickel and group 15 elements (arsenic, antimony, and bismuth), which are introduced from secondary feedstocks such as electronic waste or low-grade materials. Electrolytic copper contamination through co-deposition or incorporation of nickel,[20–22] group 15 elements,[23–28] and other elements[29–34] has long been studied extensively in the context of electrorefining and electrowinning, as well as their effects on deposition morphology and reaction kinetics. These insights provide strategies for future

sustainable copper electrometallurgy. Since these impurity elements can also complicate nodulation behavior, appropriate impurity control is urgently required. However, only a few studies have investigated how these impurities affect nodulation.[34,35]

The present study examined the effects of Ni(II) and Sb(III) ions on nodule growth behavior toward a more detailed understanding of realistic nodulation behavior. Electrolytic experiments using a cathode with a nodule-mimicking protrusion revealed that these impurities led to a coarser morphology of electrodeposited copper at the tip of the protrusion and promoted nodule growth. A combination of these experiments and numerical simulations of current distribution suggested that existing Ni(II) and Sb(III) species affected the microstructure of electrodeposited copper and promoted nodule growth through surface roughening.

2.2. Experimental

2.2.1. Electrolysis experiments

The composition of and impurity levels in the electrolyte followed the industrial process: an impurity-free solution of 0.76 mol dm^{-3} $CuSO_4$ + 1.94 mol dm^{-3} H_2SO_4 with 60 mg dm^{-3} Cl^- (as HCl), 5 mg dm^{-3} thiourea, and 0.5 mg dm^{-3} glue as typical additives. On this basis, 0.17 mol dm^{-3} $NiSO_4$ or 0.17 mol dm^{-3} Na_2SO_4 for comparison with $NiSO_4$-containing solutions or 1.65 mmol dm^{-3} Sb_2O_3, respectively, were added (hereafter referred to as Ni-, Na-, and Sb-addition compositions). As reagents, $CuSO_4 \cdot 5H_2O$ (received from JX Mining & Metals Co.), H_2SO_4 (97%, Nacalai Tesque), $NiSO_4 \cdot 6H_2O$ (99.0-102.0% purity, Nacalai Tesque), Na_2SO_4 (99.0% purity, Nacalai Tesque), Sb_2O_3 (99.0% purity, Nacalai Tesque), HCl (35%, Nacalai Tesque), thiourea (CH_4N_2S;

99% purity, Tokyo Chemical Industries, Ltd.), glue (received from JX Mining & Metals Co.), and ion-exchanged water were used to prepare the electrolyte. Electrolyte conductivity for each composition was measured using a conductivity meter (Horiba, ES-51) at a temperature of 65 °C.

Copper sheets (99.96%, Nilaco) with thicknesses of 0.8 and 5 mm were used as the cathode and anode, respectively. These electrodes were masked with fluoroplastic tape so that 60 × 50 mm on one side of the cathode and both sides of the anode were exposed. To provide a nodule-mimicking protrusion on the cathode, a columnar copper rod (99.96%, Nilaco) of 4 mm in diameter was inserted into a through-hole made in the center of the cathode and fixed with epoxy resin to the back side (Figure 2.1(a)).[15,16] The absence of contact resistance between the copper sheet and protrusion was confirmed. The anode and cathode were both placed in parallel at a distance of 25 mm, referring to the industrial arrangement. They were cleaned for 1 min with 15% HNO_3 prepared by diluting HNO_3 (60%, Nacalai Tesque) with ion-exchanged water prior to electrolysis. The volume of the electrolyte was 450 mL, and the bath temperature was maintained at 65 °C using a rubber heater and thermocouple sensor.

Galvanostatic electrolysis was performed for 40 h at a current density of 350 A m^{-2} on the projected area of the planar section (60 × 50 mm). The growth rate of the protrusion, namely, the difference in the protrusion height before and after electrolysis, ΔH_n, was evaluated for each of the eight locations, n = 1–8, of the protrusion tip, as shown in Figure 2.1(b). The average growth rate at these locations was also evaluated.

Electrochemical measurements were performed using a potentio-galvanostat with a three-electrode cell: a copper disk (4 mm in diameter) embedded in epoxy resin or a copper sheet 10 × 10 mm in size as the working electrode, a copper sheet as the counter electrode,

and Ag|AgCl in 3.33 mol dm^{-3} KCl aqueous solution with a salt bridge as the reference electrode. Copper working electrodes were polished with 2000 grid abrasive paper prior to measurements.

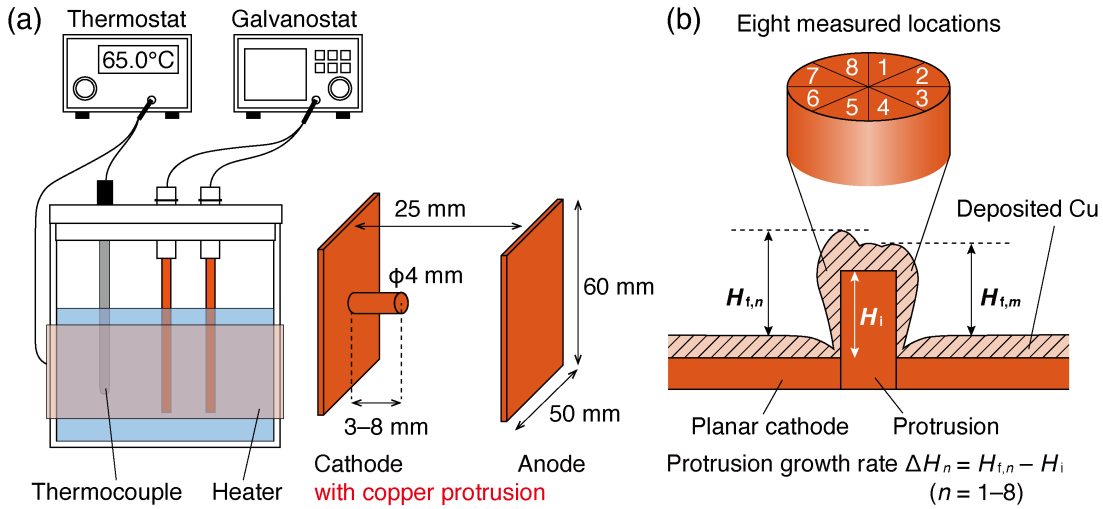

Figure 2.1 (a) Electrolysis experiments using a planar cathode with a nodule-mimicking protrusion and (b) the definition of the protrusion growth rate (ΔH_n; Index n means the eight locations at which the protrusion height was measured) evaluated by subtracting the initial protrusion height (H_i) from that after 40 h of electrolysis ($H_{f,n}$).

2.2.2. Characterization of deposited copper

After electrolysis, the protrusion-attached cathode was cut vertically through the center of the columnar protrusion using a conventional electric discharge machine, and the protrusion was divided into two pieces. One fragment of the protrusion was cemented in an epoxy resin and polished sequentially with abrasive paper (80–2000 grids) and alumina abrasive (particle size of 0.3 μm) to achieve a mirror finish on the cutting surface. This sample was immersed in a 20% HCl-ethanol

mixture containing 0.3 mol dm^{-3} $FeCl_3 \cdot 6H_2O$ for approximately 1 min for etching. The etchant was prepared by diluting 35% HCl with ethanol (99.5% purity, Nacalai Tesque) and dissolving $FeCl_3 \cdot 6H_2O$ (99.0% purity, Nacalai Tesque). The crystalline microstructure of the sample was observed using an optical microscope (Olympus, BX51M).

The contents of nickel and antimony in the other fragment of the protrusion were analyzed as follows. The fragment was further divided into two parts, one on the root side and the other on the tip side of the protrusion. They were immersed in 10% HNO_3 for 5 min to remove the electrolyte residue. After weighing, they were dissolved in 30% HNO_3, and the concentrations of nickel and antimony in the leachate were then measured by inductively coupled plasma optical emission spectrometry (ICP-OES; SII Nano Technology, SPS3500). Calibration curves were prepared using a matrix of 5% HNO_3 and standard solutions of nickel and antimony (1000 ppm, Fujifilm Wako Pure Chemicals) diluted with the matrix. The original contents of nickel and antimony in the fragments were estimated by multiplying the concentration in the leachate by the leachate volume and dividing by the weight of the pieces.

2.2.3. Numerical simulations

To evaluate current distribution on the protrusion-attached cathode, numerical simulations were performed using the finite element analysis software COMSOL Multiphysics®. The simulation model for the secondary current distribution followed previous studies.[15,17] The simulated area was the electrode surface and the electrolyte between the planar anode and cathode with a columnar protrusion, as shown in Figure 2.2(a), and it was divided into tetrahedral meshes for calculations. In the electrolyte, current distribution was governed by the Laplace equation (eq.2.1) and Ohm's law (eq.2.2), in which

electrolyte conductivity was a parameter:

$$\nabla^2 \phi_l = 0 \tag{2.1}$$

$$i_l = -\kappa \nabla \phi_l \tag{2.2}$$

where ϕ_l and i_l are the potential and current density in the electrolyte, and κ is the conductivity of the electrolyte. On the electrode–electrolyte interface, electrode kinetics were governed by the Butler–Volmer equation (eq.2.3):

$$i_{\text{B.V.}} = i_0 \left[\exp\left(\frac{(1-\alpha)nF}{RT} \eta \right) - \exp\left(\frac{-\alpha nF}{RT} \eta \right) \right] \tag{2.3}$$

where i_0, n, α, F, R, T, and η are the exchange current density, electron number (= 2), symmetry factor, Faraday constant, gas constant, absolute temperature, and overpotential, respectively. Polarization characteristics obtained by fitting the measured polarization curve, exchange current density i_0 of 150 A m^{-2}, anodic symmetry factor $(1-\alpha)n$ of 1.3, and cathodic symmetry factor αn of 0.7 were applied regardless of the assumed bath composition.[2,15] This was due to the lack of a significant difference in polarization for the electrolyte composition treated in the present study.

To evaluate protrusion growth in response to current distribution, electrolysis for 40 h at an average current density of 350 A m^{-2} for the projected area of the electrode was simulated with smooth deformation of the electrode–electrolyte interface with respect to the electrodeposition and dissolution of copper. Furthermore, the conditions under which microscopic unevenness was formed at the tip of the protrusion were mimicked by a geometry model with tetrahedral pyramids of 0.1–0.4 mm in size arrayed on the protrusion tip, as shown in Figure 2.2(b). The areas occupied by the pyramids relative to the tip of the protrusion were designed to be the same for different sizes of the pyramids (shown in blue in Figure 2.2(b)), and the surface areas of the pyramids were then identical regardless of their size. Due to calculation

difficulties, the deformation of the electrode by electrodeposition was neglected and current distribution analyses without time evolution were performed under the same electrolysis conditions.

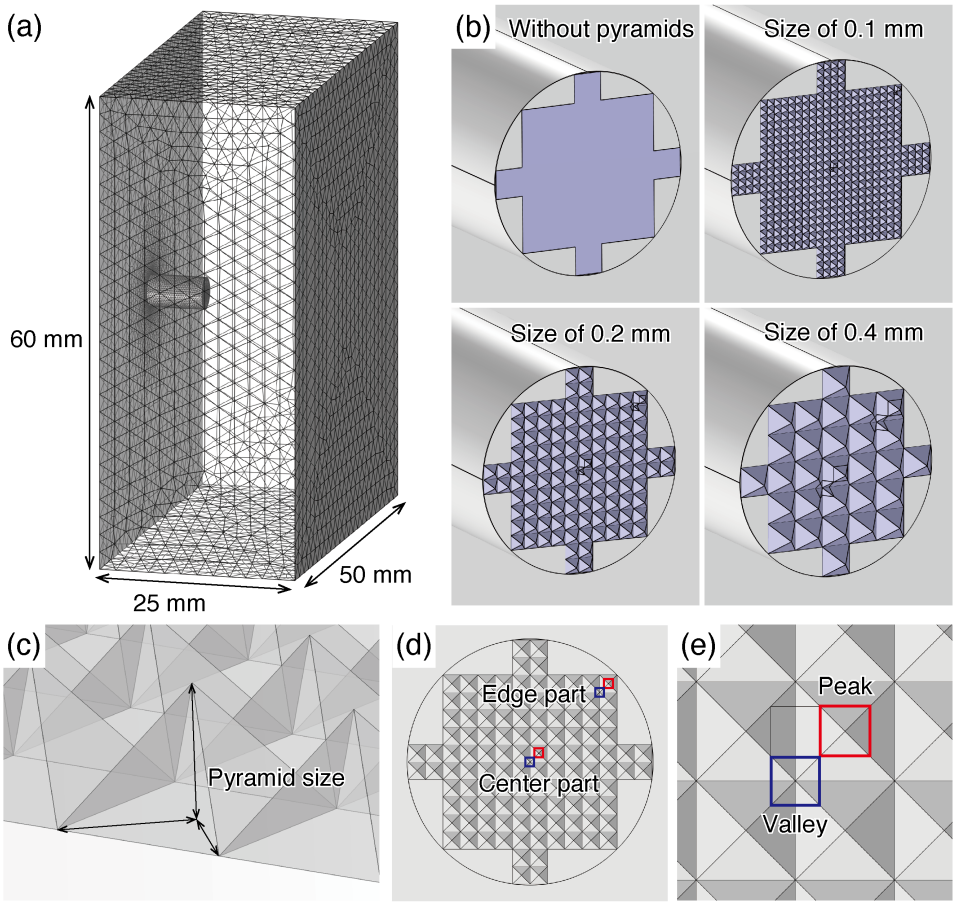

Figure 2.2 Geometry of the cell in the simulation model: (a) Electrolyte between the anode and cathode pair with a nodule-mimicking protrusion. (b) Enlarged view of the tip of the protrusion with and without three different sizes of pyramid arrays. (c) Pyramid sizes indicated by the arrows. (d,e) Areas as the peak (red square) and valley (blue square) of the pyramids defined to evaluate the local apparent current densities for the center and edge parts of the protrusion tip, respectively. (e) is an enlarged view of the center part of (d).

2.3. Results and discussion

2.3.1. Growth behavior of nodule-mimicking protrusions

Figure 2.3 shows nodule-mimicking protrusions on cathodes after electrodeposition using the electrolyte with impurity-free, Ni-addition, Na-addition, and Sb-addition compositions. In the case of the impurity-free composition, protrusions with an initial height from 3 to 5 mm had a relatively smooth appearance (Figures 2.3(a,b)). At an initial height of 6 mm or greater, grain roughness of less than 1 mm in size, which had a metallic luster originating from crystalline facets, was obtained on the protrusions (Figures 2.3(c,d)). Since the ratio of local current density to limiting current density has been shown to increase to approximately 0.3–0.5, a transition occurs from smooth to non-smooth deposition, such as needles and nodules.[9,36] In the present study, current was concentrated on the tip of the protrusion and electrodeposition proceeded at a relatively high ratio of local current density to limiting current density; therefore, rough deposits were obtained.

In the case of the Ni-addition composition, more severe irregularities with facets were obtained around the tips of the protrusions in all cases with an initial height from 3 to 8 mm (Figures 2.3(e–h)) than with the impurity-free composition (Figure 2.3(a–d)). At an initial height of more than 7 mm, coarse grains greater than 1 mm in size formed and had a dendritic morphology (Figures 2.3(g,h)). In the case of the Na-addition composition, at an initial height of more than 7 mm (Figure 2.3(i)), deposits became rougher than with the impurity-free composition (Figure 2.3(d)); however, dendritic growth, as with the Ni-addition composition, was not obtained. In the case of the Sb-addition composition, deposits became non-uniform with facets, particularly at an initial height of more than 5 mm (Figures 2.3(l–n)).

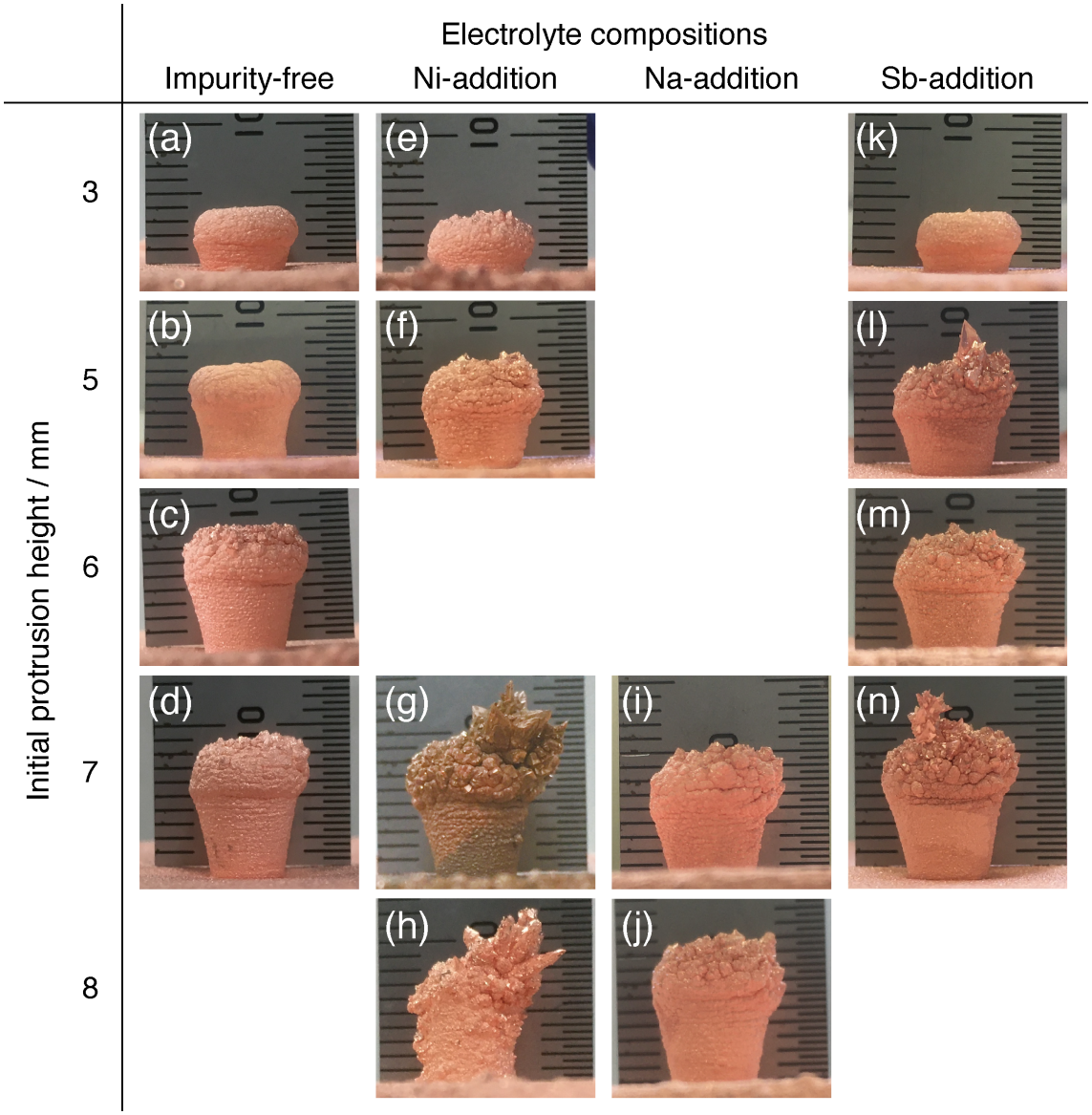

Figure 2.3 Electrodeposition morphology of copper protrusions with various initial heights after 40 h of electrolysis with four different electrolyte compositions: (a–d) impurity-free, (e–h) Ni-addition, (i,j) Na-addition, and (k–n) Sb-addition.

The protrusion growth rate was evaluated for each sample (Figure 2.4). In the case of the impurity-free composition, the protrusion growth rate increased almost linearly with the initial protrusion height within 5 mm due to enhancement of current concentration at the protrusion. There is a critical jump at an initial height of 5 mm, which comes from the appearance of surface roughness as mentioned earlier. In the case of the Ni-addition composition (Figure 2.4(a)), at an initial height of more than 5 mm, the average growth rate was higher than with the impurity-free composition. At an initial height of more than 7 mm, the growth rate at the eight measured locations significantly varied. This variation in the growth rate mainly reflected the surface roughness of deposits at the protrusion tip, which was attributed to coarse grains. Similarly, in the case of the Sb-addition composition (Figure 2.4(b)), the average growth rate was higher than with the impurity-free composition at an initial height of more than 5 mm, and variations in the growth rate at each location were also larger. These results show that the addition of nickel, antimony, and sodium sources to the electrolyte promoted protrusion growth in that order by inducing non-smooth deposition at the tip of the protrusion.

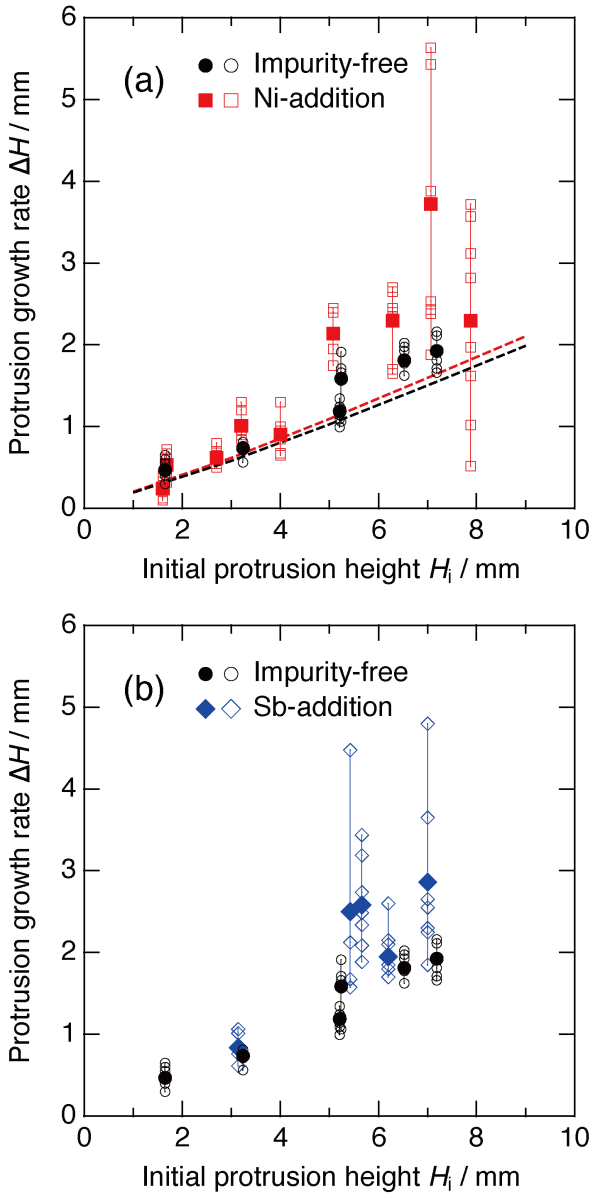

Figure 2.4 Protrusion growth rate after 40 h of electrolysis for different initial protrusion heights in (a) impurity-free (black circle) and Ni-addition (red square) and (b) impurity-free (black circle) and Sb-addition (blue diamond) solutions. Empty markers indicate the protrusion growth rate evaluated at eight different locations (Figure 2.1(b)), and filled markers indicate their average. The simulated protrusion growth rate as broken lines in (a), using an electrolyte conductivity of 689 mS cm^{-1} for the impurity-free solution (black) and 647 mS cm^{-1} for the Ni-addition solution (red).

Figure 2.5 shows optical microscope images of a cross-section of the protrusion with an initial height of 7 mm for each electrolyte composition. In all cases, the internal microstructure observed in the initial stage of electrodeposition was classified as the unoriented dispersion type (UD) consisting of fine grains, and it gradually shifted as deposition thickness increased to the field-oriented texture type (FT) or their mixture (FT-UD) and, ultimately, the basis reproduction structure (BR).[36] The formation of this microstructure is related to the effects of the surface adsorption and polarization of additives commonly used to achieve a smooth deposition surface.[6–8] In the Ni-, Na-, and Sb-addition compositions, the microstructure shifted from UD to FT and BR at an earlier stage (at a smaller electrodeposition thickness) than with the impurity-free composition, particularly with the Ni-addition composition. As BR growth proceeded, coarse grains were more likely to form and, thus, the deposition surface became rougher. The importance of this result is that the effects of these impurity ions were not obvious until the duration of electrolysis was longer and the thickness of deposited copper exceeded 500 μm. These impurity ions accelerated transition in the microstructure type, resulting in rougher deposits within 40 h of electrolysis.

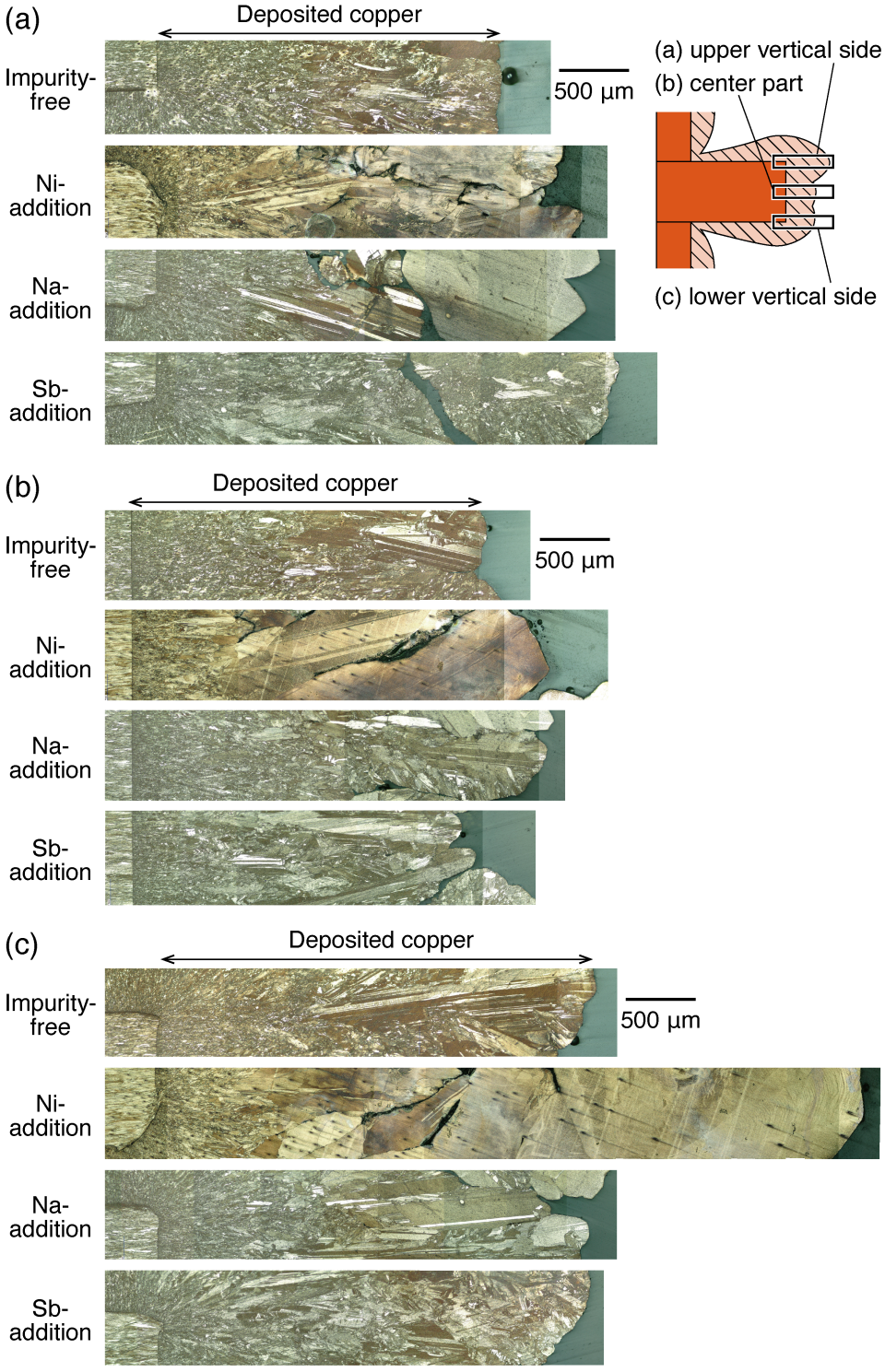

Figure 2.5 Crystalline microstructures of electrodeposited copper on (a) the upper vertical side, (b) center part, and (c) lower vertical side (these locations are illustrated) of the protrusion tip with an initial height of 7 mm obtained from four different electrolyte compositions.

This section discusses the mechanism by which these impurity ions affected microstructure formation by co-deposition. The standard electrode potentials of copper and nickel are +0.337 and –0.250 V *vs*. SHE, respectively. Local current density at the peak area of the arrayed pyramids, as shown in a later section, was estimated to be –1200 A m^{-2} at most in simulations. Based on galvanostatic electrolysis at this current density in the Ni-addition solution (Figure 2.6), the overpotential was only –0.11 V from the open circuit potential of copper. This was sufficiently small for the reduction of Ni(II) ions. In addition, copper and nickel constitute a binary system of a total rate solid solution and there is no intermetallic compound.[37] In this case, low-activity nickel (i.e., nickel activity of 10^{-10}), which compensates for the potential difference between copper and nickel, is unlikely to be co-deposited with copper at a high content. Therefore, the electrodeposition of nickel is not considered to occur in this potential region. The nickel content in deposits on the protrusion was quantitively analyzed by ICP-OES, and did not significantly differ between the samples obtained from the impurity-free and Ni-addition electrolytes.

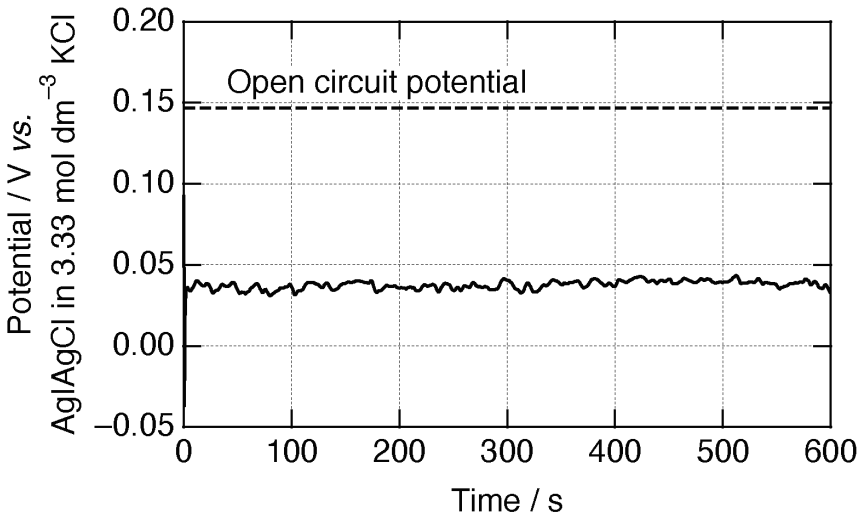

Figure 2.6 Electrode potential during galvanostatic electrolysis at a current density of –1200 A m^{-2} (solid line) and the open circuit potential (broken line) in the electrolyte of the Ni-addition solution. A copper disk (4 mm in diameter) embedded in epoxy resin was used as the working electrode.

Linear sweep voltammograms (Figure 2.7) obtained in solutions of a low $CuSO_4$ concentration with and without Sb(III) ions showed a weak, but clear reduction wave at approximately –0.15 V *vs*. Ag|AgCl in 3.33 mol dm^{-3} KCl only for the Sb-addition solution, which corresponded to the reduction of Sb(III) to Sb.[25] Local current density was estimated to be –1200 A m^{-2} at most in simulations, and the electrode potential for copper deposition at this current density was 0.04 V *vs*. Ag|AgCl in 3.33 mol dm^{-3} KCl (Figure 2.6), which is nobler than the potential for Sb deposition. Therefore, the electrodeposition of Sb does not occur in this potential region. The active co-deposition of antimony as an alloy is also unlikely because the interaction between copper and antimony is not as significant, as indicated by the small solid solubility limit of antimony in copper,[38] and the concentration of Sb(III) ions in the electrolyte was more than two orders of magnitude

smaller than that in cupric ions. As with nickel, the content of antimony in deposits on the protrusion was below the detection limit. In other words, even if deposited copper contained antimony, its amount was very small. In conclusion, these impurity ions exerted effects through mechanisms other than their incorporation into copper by co-deposition.

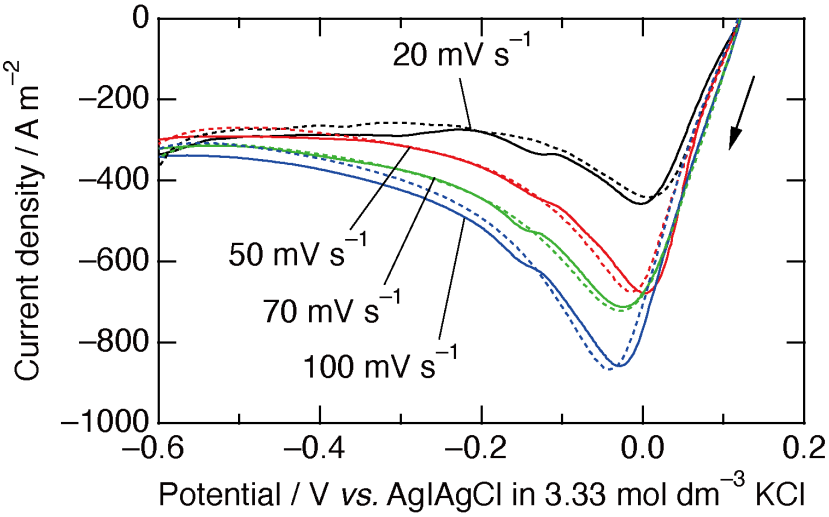

Figure 2.7 Linear sweep voltammograms measured at scan rates of 20–100 mV s^{-1} in 0.16 mol dm^{-3} $CuSO_4$ + 1.94 mol dm^{-3} H_2SO_4 solutions without any additives, with (solid lines) and without (broken lines) 1.65 mmol dm^{-3} Sb_2O_3, respectively. A copper sheet with an exposed area of 1 × 1 cm was used as the working electrode.

2.3.2. Numerical simulations of current distribution

Impurity ions changed the microstructure by being present in the electrolyte even though they were not incorporated. Therefore, the viewpoint shifted to the electrolyte side. One possible cause of the microstructure transition is a change in electrolyte properties due to the addition of impurity sources. Regarding a typical copper electrolyte, a

higher concentration of sulfates, such as nickel sulfate, has been associated with an increase in electrolyte viscosity and decrease in conductivity.[39,40] The following section focused on the effects of conductivity variations on current distribution.

Smooth growth by electrodeposition according to current distribution was verified. The growth rates of the protrusions after 40 h of electrolysis were simulated as shown in the broken lines (Figure 2.4(a)) in the same manner as described in the Experimental section, using conductivities measured for the impurity-free (689 mS cm^{-1}) and Ni-addition solutions (647 mS cm^{-1}). It is important to note that the finite element simulation used in the present study cannot reproduce the crystal characteristics of the solid phase, i.e., electrodeposited copper, such as being dendritic and granular with faceted crystal growth. Reproducing them would require advanced simulations that treat crystal growth in combination with different models, such as kinetic Monte Carlo method;[41] however, this remains difficult because of the lack of information on the reaction mechanism involving impurity ions.

At an initial protrusion height smaller than 4 mm, simulated growth rates were consistent with those in the experiments because smooth deposition occurred at the protrusion in this range. At an initial protrusion height of more than 5 mm, growth rates in the experiments were markedly higher than those in the simulations, particularly with the Ni-addition composition. This difference resulted from non-smooth deposition at the protrusion surface, which cannot be reproduced by simulations. More importantly, the enhancement of protrusion growth by the addition of nickel was mainly due to the roughening of deposits. As shown by the small difference in the two broken lines (Figure 2.4(a)), the effects of conductivity deviations on the growth rate were sufficiently small, although it slightly facilitated current concentration at the protrusion as long as smooth deposition was assumed.

The effects of microscopic unevenness that developed at the

protrusion surface were evaluated based on the simulated current distribution. A set of regular square pyramids were arrayed on the tips of the columnar protrusion (Figure 2.2(b)) to imitate conditions under which {111} facets, the most stable plane of FCC, emerged and grew. Only current distribution was calculated without deforming the electrode geometry through electrodeposition to avoid inaccurate calculation results caused by mesh distortions.

The initial focus is on current distribution at the entire protrusion. The “apparent” current density at the protrusion tip, namely, the total current integrated over the surface of the arrayed pyramids (shown in blue in Figure 2.2(b)) normalized by its projection area (the blue area in “without pyramids” in Figure 2.2(b)), was evaluated as shown in Figure 2.8. Basically, increases in the height of the protrusion H_i, were associated with a greater apparent current density at the protrusion tip. This result indicated an increase in the amount of copper deposited on the tip and, consequently, a higher average growth rate of the protrusion. With the pyramids in place, apparent current density increased by a factor of 1.5–1.6 from that without the pyramids, corresponding to the larger effective surface area of the protrusion tip. Therefore, once surface roughness formed at the protrusion tip, current concentration began to increase at an accelerated rate. A decrease in conductivity resulted in a slight, at most 3%, increase in apparent current density.

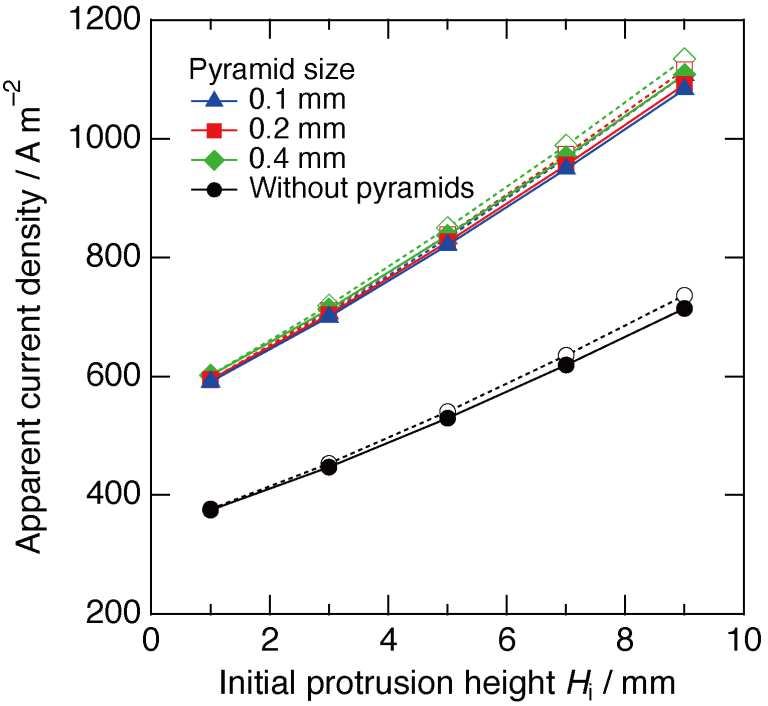

Figure 2.8 Simulated apparent current density at the tip of the protrusion with pyramid sizes of 0.1 mm (blue triangle), 0.2 mm (red square), and 0.4 mm (green diamond) and without pyramids (black circle). Solid lines and filled markers are for an electrolyte conductivity of 689 mS cm^{-1} in the impurity-free solution, and broken lines and empty markers are for an electrolyte conductivity of 647 mS cm^{-1} in the Ni-addition solution.

The next focus is on local current distribution at the convexity of the arrayed pyramids. Apparent current density in the peak and valley areas of the pyramids (defined as the red and blue squares in Figure 2.2(d,e), respectively) and the difference between them for the center and edge portions of the protrusion were examined, as shown in Figure 2.9. This difference indicated the bias of the amount of copper deposited at the convex and concave portions of the arrayed pyramids and, thus, was considered to reflect the degree of convexity growth. The larger the pyramid size, the greater the difference between the simulated

currents flowing in the peak and valley. This suggested that convexity is more likely to grow, i.e., convexity growth is self-promoting. Moreover, the larger the height of the basis protrusion, the larger the current difference, resulting in the more rapid development of coarse grains or secondary nodules when the nodule becomes large enough to be in close proximity to the anode. The current difference was larger at the edge of the protrusion than at the center because current concentrated at the edge of the cylindrical protrusion. This is consistent with macroscopic unevenness often emerging at the edge in experiments (Figure 2.3). These changes became more pronounced when electrolyte conductivity decreased, resulting in an up to 11% increase in the current density difference.

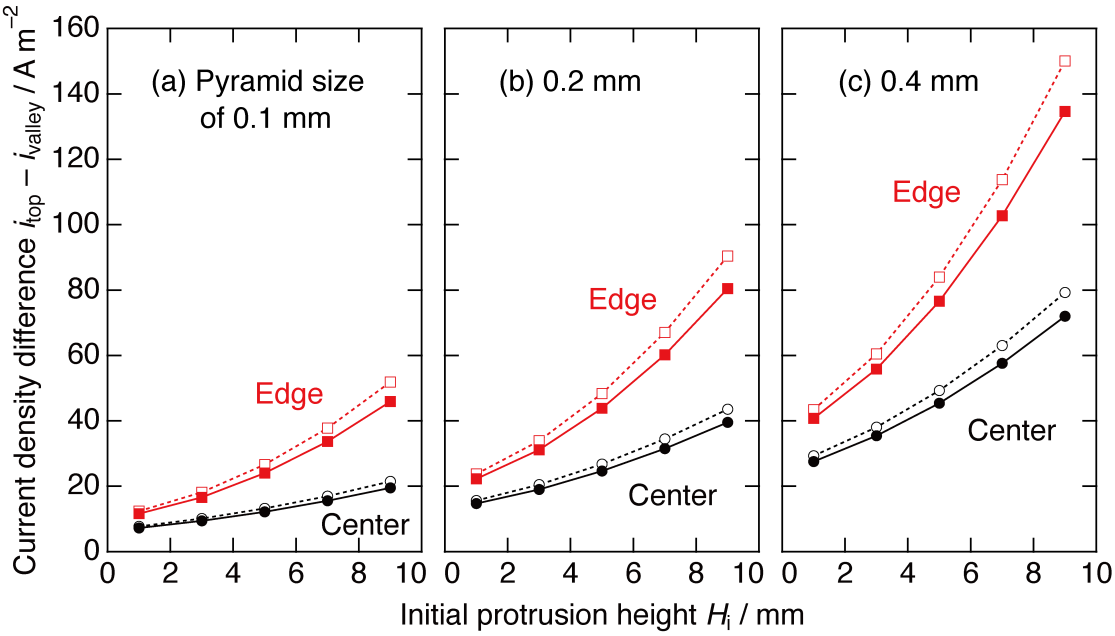

Figure 2.9 Simulated differences in apparent current density between peak and valley areas of pyramids with sizes of (a) 0.1 mm, (b) 0.2 mm, and (c) 0.4 mm for the center (black) and edge (red) parts of the protrusion tip. Solid lines are for the electrolyte conductivity of 689 mS cm^{-1} and broken lines are for that of 647 mS cm^{-1}.

In summary, the effects of conductivity degradation only became apparent after microstructure transitions from UD to FT and BR, that is, conductivity did not markedly affect current distribution as long as smooth deposition proceeded. On the other hand, with the appearance of surface roughness, the local current concentration at the convexity was enhanced due to the degradation of conductivity in addition to the contribution of current concentration over the entire protrusion.

The conductivities of the Na- (646 mS cm^{-1}) and Sb-addition (690 mS cm^{-1}) electrolytes were similar to those of the Ni-addition (647 mS cm^{-1}) and impurity-free (689 mS cm^{-1}) electrolytes, respectively. Nevertheless, the behavior of protrusion growth differed between the Ni- and Na-addition electrolytes as well as between the Sb-addition and impurity-free electrolytes. These results also suggest that the addition of impurity ions not only changed the properties of the bulk electrolyte, but also that the impurity ions themselves affected the copper electrocrystallization process to accelerate the transition of the crystalline microstructure prior to the emergence of surface roughness.

2.3.3. Effects of impurity ions on protrusion growth

The transition of the internal microstructure to the BR type was promoted by Ni(II) and Sb(III) ions; however, neither actively co-deposited with copper, and the degradation of conductivity was only affected after the rough surface became apparent. The remaining possibility is that these impurity ions affect the copper electro-crystallization process by adsorbing on the surface and temporarily interposing at the electrode–electrolyte interface, even though they are not incorporated into the deposits.

The additives commonly used in copper electrorefining (e.g., glue, thiourea, and Cl^- ions) are known to have different functions from each

other and markedly affect the microstructure by adsorbing on specific crystalline surfaces.[6,7,42,43] The proper control of the dosage of these three additives suppresses the formation of coarse grains and achieves a smooth surface. Similarly, Ni(II) and Sb(III) ions may have temporarily adsorbed on the cathode surface, similar to conventional additives, interfering with the smoothing effects of the additives. It is important to note that current density at the tip of the protrusion was greater than that under typical operating conditions, and thus, deviated from the target current density of the additive composition adjusted to obtain a smooth surface. Hospadaruk *et al*. reported an increase in the overpotential of copper electrodeposition when an antimony species was introduced into the solution and suggested the surface adsorption of antimony species.[27] Nakano *et al*. showed that under typical electrorefining conditions, the simultaneous use of the three additives, glue, thiourea, and Cl^- ions, resulted in the formation of the FT-type microstructure preferentially oriented in the <110> direction.[44] Moreover, if one of the three additives was absent, the FT structure was not maintained: the UD structure formed in the absence of glue, and coarse grains formed through epitaxial growth in the absence of thiourea or Cl^-. Based on this finding, Ni(II) and Sb(III) ions may weaken the functions of thiourea or Cl^- ions, such as by inhibiting their adsorption; however, the mechanisms by which impurity ions induce the BR structure remain unclear and warrant further study to achieve optimal additive control.

In addition, once the transition to the BR structure proceeds and a rough surface appears to a size of several tens to hundreds μm, protrusion growth is then accelerated by current concentration over the entire protrusion and at local convexity, finally developing into large grains or dendritic deposits of several mm. In the Ni-addition electrolyte, the degradation of conductivity further contributes to uneven growth by intensifying the local current concentration. A

schematic illustration summarizing these growth processes is shown in Figure 2.10.

Therefore, it is important to prevent the transition of the growth mode to the BR type in order to avoid short circuits by nodulation. Maintaining low impurity levels by enhancing the recovery and removal of impurity ions in the electrolyte, as well as optimizing the dosage of additives used in response to various impurity concentrations, are expected to be important solutions for suppressing nodule growth.

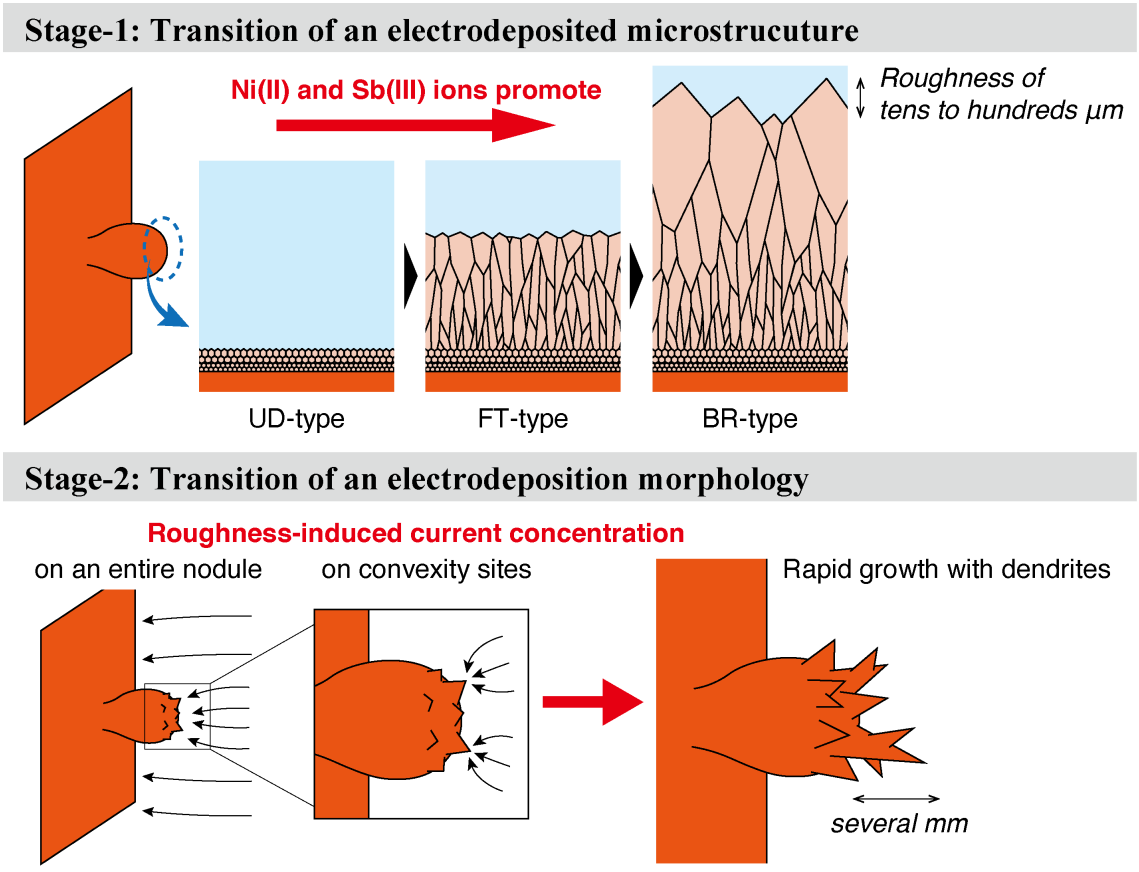

Figure 2.10 Schematic illustration of nodule growth mechanism by transition of microstructure and electrodeposition morphology under the effects of Ni(II) and Sb(III) ions.

2.4. Conclusions

The effects of Ni(II) and Sb(III) ions on nodule growth were investigated in electrolysis experiments using a cathode with a nodule-mimicking protrusion and simulations. When the electrolyte contained these impurity ions, the electrodeposition morphology at the protrusion became coarser and more dendritic and protrusion growth was promoted more than with the impurity-free composition. Rapid growth was the most apparent with the Ni-addition composition, followed by the Sb- and Na-addition compositions. This result was attributed to (i) increased surface roughness due to Ni(II) and Sb(III) ions, which facilitated the transition of the microstructure from UD to FT and BR, and (ii) a switch to a rapid growth mode due to current concentration over the entire protrusion and at local convexity sites, originating from surface roughening at the protrusion. The latter was enhanced with the Ni-addition composition because of lower conductivity.

These effects may significantly change the microstructure and surface morphology of electrolytic copper. The appropriate control of the levels of these impurities as well as typically-used smoothing additives may be one of the parameters employed to smooth electrodeposition and suppress short circuits by nodulation.

References

1. M. E. Schlesinger, M. J. King, K. C. Sole, and W. G. Davenport, in *Extractive Metallurgy of Copper*, edited by M. E. Schlesinger, M. J. King, K. C. Sole, and W. G. Davenport, 5th Ed. (Elsevier, Oxford, 2011), pp. 251–280.
2. M. Miyamoto, S. Mitsuno, A. Kitada, K. Fukami, and K. Murase, *Hydrometallurgy*, **216**, 106013 (2023).
3. T. N. Andersen, C. H. Pitt, and L. S. Livingston, *J. Appl. Electrochem*, **13**(4), 429–438 (1983).
4. J. E. Dutrizac and T. T. Chen, in *4th International Confonference COPPER 99-COBRE 99* (1999), pp. 383 – 403.
5. D. F. Suarez and F. A. Olson, *J. Appl. Electrochem.*, **22**(11), 1002–1010 (1992).
6. Z. Mubarok, I. Filzwieser, and P. Paschen, in *Proceedings - European Metallurgical Conference EMC 2005* (2005), pp. 109–122.
7. B. Veilleux, A. M. Lafront, and E. Ghali, *J. Appl. Electrochem.*, **31**(9), 1017–1024 (2001).
8. A. M. Lafront, B. Veilleux, and E. Ghali, *J. Appl. Electrochem.*, **32**(3), 329–337 (2002).
9. J. Bauer and M. Moats, *Metall. Mater. Trans. B*, **53**(1), 561–570 (2022).
10. M. C. Lafouresse, P. J. Heard, and W. Schwarzacher, *Phys. Rev. Lett.*, **98**(23), 236101 (2007).
11. M. C. Lafouresse, Y. Fukunaka, T. Matsuoka, and W. Schwarzacher, *Electrochim. Acta*, **56**(12), 4457–4461 (2011).
12. M. C. Lafouresse, Y. Fukunaka, T. Homma, S. Honjo, S. Kikuchi, and W. Schwarzacher, *Electrochem. Solid-State Lett.*, **14**(7), D77 (2011).

13. Y. Fukunaka, H. Doi, and Y. Kondo, *J. Electrochem. Soc.*, **137**(1), 88–93 (1990).
14. M. Pourgharibshahi, S. M. J. Khorasani, N. Yaghoobi, and P. Lambert, *Electrocatalysis*, **14**(2), 138–147 (2023).
15. K. Adachi, Y. Nakai, S. Mitsuno, M. Miyamoto, A. Kitada, K. Fukami, and K. Murase, *J. MMIJ*, **136**(2), 8–13 (2020).
16. Y. Nakai, K. Adachi, A. Kitada, K. Fukami, and K. Murase, in *Rare Metal Technology 2018*, edited by H. Kim, B. Wesstrom, S. Alam, T. Ouchi, G. Azimi, N. R. Neelameggham, S. Wang, and X. Guan (Springer Cham, 2018), pp. 319–323.
17. K. Adachi, Y. Nakai, A. Kitada, K. Fukami, and K. Murase, in *Rare Metal Technology 2018*, edited by H. Kim, B. Wesstrom, S. Alam, T. Ouchi, G. Azimi, N. R. Neelameggham, S. Wang, and X. Guan (Springer Cham, 2018), pp. 215–222.
18. Q. Zeng, C. Li, Y. Meng, J. Tie, R. Zhao, and Z. Zhang, *Measurement*, **164**, 108015 (2020).
19. J. M. Werner, W. Zeng, M. L. Free, Z. Zhang, and J. Cho, *J. Electrochem. Soc.*, **165**(5), E190–E207 (2018).
20. M. Sahlman, J. Aromaa, and M. Lundström, *Metals*, **11**(11), 1758 (2021).
21. Y. Wang, L. Li, H. Li, and H. Wang, *Ionics*, **25**(10), 5045–5056 (2019).
22. T. Subbaiah and S. C. Das, *Hydrometallurgy*, **36**(3), 271–283 (1994).
23. F. Verbruggen, P. Ostermeyer, L. Bonin, A. Prévoteau, K. Marcoen, T. Hauffman, T. Hennebel, K. Rabaey, and M. S. Moats, *Miner. Eng.*, **176**, 107312 (2022).
24. F. Verbruggen, A. Prévoteau, L. Bonin, K. Marcoen, T. Hauffman, T. Hennebel, K. Rabaey, and M. S. Moats, *Hydrometallurgy*, **211**, 105886 (2022).

25. J. B. Hiskey and Y. Maeda, *J. Appl. Electrochem.*, **33**(5), 393–401 (2003).
26. T. J. O'keefe and L. R. Hurst, *J. Appl. Electrochem.*, **8**(2), 109–119 (1978).
27. V. Hospadaruk and C. A. Winkler, *JOM*, **5**(10), 1375–1377 (1953).
28. R. G. Barradas and M. Girgis, *Metall. Trans. B*, **22**(5), 575–581 (1991).
29. L. Muresan, A. Nicoara, S. Varvara, and G. Maurin, *J. Appl. Electrochem.*, **29**(6), 723–731 (1999).
30. L. Cifuentes, M. Grágeda, J. M. Casas, and T. Vargas, *Mater. Sci. Technol.*, **25**(6), 753–759 (2009).
31. T. R. Da Silva, D. Majuste, J. Bauer, and M. S. Moats, *Hydrometallurgy*, **198**, 105513 (2020).
32. F. Safizadeh, A.-M. Lafront, E. Ghali, and G. Houlachi, *Hydrometallurgy*, **111**–**112**(1), 29–34 (2012).
33. A. Baral, C. K. Sarangi, B. C. Tripathy, I. N. Bhattacharya, and T. Subbaiah, *Hydrometallurgy*, **146**, 8–14 (2014).
34. M.-E. Wagner, R. Valenzuela, T. Vargas, M. Colet-Lagrille, and A. Allanore, *J. Electrochem. Soc.*, **163**(2), D17–D23 (2016).
35. M. Reza Shojaei, G. Reza Khayati, S. Mohammad Javad Korasani, and R. Kafi Harnashki, *Eng. Fail. Anal.*, **133**, 105970 (2022).
36. R. Winand, *Hydrometallurgy*, **29**(1–3), 567–598 (1992).
37. M. A. Turchanin, P. G. Agraval, and A. R. Abdulov, *Powder Metall. Met. Ceram.*, **46**(9–10), 467–477 (2007).
38. X. J. Liu, C. P. Wang, I. Ohnuma, R. Kainuma, and K. Ishida, *J. Phase Equilibria*, **21**(5), 432–442 (2000).
39. D. C. Price and W. G. Davenport, *Metall. Trans. B*, **12**(4), 639–643 (1981).
40. T. Subbaiah and S. C. Das, *Metall. Trans. B*, **20**(3), 375–380 (1989).

41. X. Li, T. O. Drews, E. Rusli, F. Xue, Y. He, R. Braatz, and R. Alkire, *J. Electrochem. Soc.*, **154**(4), D230 (2007).
42. A. Suzuki, S. Oue, S. Kobayashi, and H. Nakano, *Mater. Trans.*, **58**(11), 1538–1545 (2017).
43. A. Suzuki, S. Oue, and H. Nakano, *Mater. Trans.*, **61**(5), 972–979 (2020).
44. H. Nakano, S. Oue, Y. Tsuyama, H. Fukushima, S. Kobayashi, and K. Tomioka, *J. MMIJ*, **127**(10–11), 662–666 (2011).

Chapter 3

Lead Electrodeposition from Highly Concentrated Calcium Chloride Aqueous Solutions

3.1. Introduction

The primary application of metallic lead is in lead-acid batteries and the demand for lead for use in automobiles is expected to increase in the near future.[1] Even so, environmental regulations such as the RoHS Directive in the European Union have restricted the use of lead in various industries, including the soldering of electronic devices. The efficient separation and recovery of this metal through lead refining from spent lead-acid batteries, electric and electronic wastes, and residues from copper and zinc refineries has become an essential aspect of conserving lead while also preventing environmental pollution.

Traditionally, the Betts process is employed during the final stage of lead refining. This is an electrorefining process that utilizes an electrolyte based on hexafluorosilicic acid (H_2SiF_6) to refine crude lead obtained from preceding pyrometallurgical processes.[2,3] However, the generation of wastewater containing fluorine is increasingly of concern as a consequence of stricter emission regulations in recent years. In addition, air pollution caused by the volatilization of hydrogen fluoride (HF) and silicon tetrafluoride (SiF_4) from processing solutions can be problematic. Therefore, there is a need for alternative lead electrolytes that are free of fluorine and have a lower impact on the environment.

Lead electrodeposition baths intended for various applications have been explored and commercialized. These applications have included the electroplating of Pb-Sn eutectic solder and electrorefining.[4,5] Such baths can comprise commercially available aqueous solutions of

compounds such as fluoroboric acid,[6] sulfamic acid,[7] or methanesulfonic acid.[8] Alkaline solutions[9] and non-aqueous systems such as deep eutectic solvents[10] and ionic liquids[11] may also be employed. However, viable substitutes are limited to those able to dissolve lead salts as well as by economic considerations and the morphology of the resulting lead deposits. The use of chloride baths for lead electrodeposition was previously studied with regard to the wet recycling of spent lead-acid batteries.[12–14] This process combines the leaching of lead compounds into a chloride solution with the subsequent electrowinning of lead. However, the solubility of $PbCl_2$ in these chloride solutions is not as high as the Pb(II) concentration in a typical electrorefining baths (approximately 70 g dm^{-3} of lead ions in the case of the Betts process),[3] which makes the application of such chloride systems to electrorefining challenging.

The present work assessed highly concentrated aqueous solutions capable of dissolving large quantities of alkaline or alkaline-earth chloride salts, including calcium chloride ($CaCl_2$) and lithium chloride (LiCl). Such solutions have unique properties when used as metal electrodeposition baths.[15,16] In the case of calcium chloride hexahydrate ($CaCl_2 \cdot 6H_2O$), which has a melting point of 29.8°C, Ca^{2+} cations coordinate with almost all water molecules constituting the solution.[17,18] Aqueous solutions of such compounds or the hydrated salts themselves, having melting points close to room temperature, are known as hydrate melts. The mean activity coefficients for these solutions increase as the proportion of water molecules that do not interact with electrolyte ions, referred to as “free water,” decreases.[19] As a result of thermodynamic and mass transport effects, these unique properties suppress the hydrogen evolution reaction, while also facilitating the complexation of metal cations with chloride anions. Aqueous $CaCl_2$ solutions are expected to be applicable to industrial scale processes because such solutions are inexpensive and minimally

toxic and there are no effluent regulations. In fact, $CaCl_2$ is commonly used as a snow melting agent. With these characteristics in mind, concentrated $CaCl_2$ solutions could be a viable option for the preparation of unique metal electrodeposition baths utilizing a chloride complex concept.

Displacement silver plating using concentrated $CaCl_2$ solutions was previously demonstrated by Adachi *et al*.[15] These solutions were found to dissolve silver chloride (AgCl), which is insoluble in pure water but dissolves somewhat in concentrated $CaCl_2$ solutions to form chloride complexes as a result of the high Cl^- activity of such solutions. Adachi *et al.* attributed the smooth displacement silver plating obtained from such solutions to the higher viscosity and lower diffusion coefficient (by one order of magnitude) and diffusion layer thickness compared with aqueous solutions of standard concentration.

On this basis, it can be expected that, similar to AgCl, lead chloride ($PbCl_2$) may dissolve in concentrated $CaCl_2$ solutions to generate electrodeposition baths, despite being insoluble in pure water. Several studies have already indicated the increased solubility of $PbCl_2$ in aqueous solutions having high concentrations of chloride ions.[20,21] However, there have been no detailed investigations of the solubility of $PbCl_2$ in such concentrated solutions or in hydrate melts. In addition, the electrodeposition behavior of lead from such solutions is presently uncertain. The aim of the present study was to assess the feasibility of lead electrodeposition based on $PbCl_2$ using baths comprising concentrated $CaCl_2$ solutions by investigating the solubility of $PbCl_2$ in such solutions and the corresponding lead electrodeposition behavior.

3.2. Experimental

3.2.1. Assessing $PbCl_2$ solubility in $CaCl_2$ solutions

$CaCl_2$ (95% purity, FUJIFILM Wako Pure Chemicals) was dissolved in deionized water to obtain solutions with varying concentrations. Subsequently, a specific amount of $PbCl_2$ (99% purity, FUJIFILM Wako Pure Chemicals) was added to each solution followed by stirring at 300 rpm for 12 h at 30 ºC to obtain a series of $PbCl_2$-saturated solutions. After filtration to remove any undissolved residue, 0.1 mL of each such solution was transferred into a 100 mL volumetric flask. Following this, 1 mL of nitric acid (60 wt.%, Nacalai Tesque) and 2.5 g of thiourea (99% purity, Tokyo Chemical Industry) were added and the solution was made up to volume with deionized water. It is important to note that thiourea was added as a complexing agent to avoid $PbCl_2$ precipitation during dilution. The solubility of $PbCl_2$ in each solution was determined by quantifying the Pb concentration using inductively coupled plasma optical emission spectrometry (ICP-OES; SII Nanotechnology, PSP3500). A calibration curve was prepared prior to the ICP-OES analyses using a commercially available standard solution of Pb.

3.2.2. Electrochemical measurements

All measurements were performed at room temperature and in air utilizing a potentio-galvanostat (BioLogic, SP-300). Initially, the immersed potentials of Pb metal were evaluated in 9.74 and 5.84 mol kg^{-1} $CaCl_2$ solutions, both of which included 10 mmol kg^{-1} of $PbCl_2$. During these trials, the working electrodes consisted of Pb metal sheets (99.99%, Nilaco) polished with emery paper and rinsed with deionized

water. Since lead is a soft metal, there was a possibility that abrasive particles could have become embedded in the surfaces of the sheets during polishing but this was not expected to affect the measured electrode potentials. A reference electrode consisting of Ag|AgCl with a porous glass liquid junction immersed in a 3.33 M (M = mol dm^{-3}) KCl solution was also used.

Cyclic voltammetry experiments were performed to examine the electrochemical phenomena during Pb electrodeposition. In these trials, the working electrode was a Pt disk (3 mm diameter) while the counter electrode was a glassy carbon electrode and the same reference electrode as previously described was utilized. Hydrodynamic voltammetry with a rotating disk electrode (RDE) was carried out to determine the diffusion coefficient for Pb(II) ions in each solution. Linear sweep voltammetry (LSV) was performed with a Pt RDE (5 mm diameter) as the working electrode and a rotating electrode apparatus (Hokuto Denko, Dynamic Electrode HR-201). The static viscosity of each solution was measured with an EMS viscometer (Kyoto Electronics Corporation, EMS-1000). The density of each solution was determined by finding the mass of a 1 mL volume while the kinematic viscosity was calculated by dividing the static viscosity by the density. Electrochemical behaviors were also studied in dilute aqueous solutions containing 0.10 mol kg^{-1} of $NaNO_3$ (98% purity, Fujifilm Wako Pure Chemicals) and 10 mmol kg^{-1} of $Pb(NO_3)_2$ (99.5% purity, Nacalai Tesque).

3.2.3. Electrodeposition and characterization of deposits

Potentiostatic electrodeposition was conducted with a solution containing 5.84 mol kg^{-1} $CaCl_2$ and 100 mmol kg^{-1} $PbCl_2$, employing a volume of approximately 50 mL. The applied potential was 100 mV

lower than the immersed potential determined earlier for Pb and was continued until the total charge reached 1 C cm^{-2}. In certain experiments, a stir bar at the bottom of the cell was rotated at 400 rpm. Copper sheets (0.5 mm thickness, Hull Cell Cathode Plates, Yamamoto-MS) having a rectangular morphology with a width of 1 cm were used as the working electrodes because these sheets were able to remain vertical relative to the Pb sheets and could be distinguished from electrodeposited Pb based on X-ray diffraction (XRD) patterns. Prior to electrodeposition, each specimen was submerged in a degreasing agent (Ace Clean 850, Okuno Chemical Industries), rinsed with pure water and covered with fluoroplastic tape, leaving a 1 cm × 1 cm area exposed. The counter electrode was an IrO_2-coated titanium electrode used as an insoluble anode. Although the anodic dissolution of lead metal was also possible, the anodic passivation of lead occurred during these electrolysis trials under certain conditions, such as prolonged electrolysis or at high current densities. Hence, in the present study, an insoluble anode was utilized to reduce experimental error. In the case that the electrodeposits were rinsed with water alone, the solution remaining on the substrate would have become diluted, possibly causing $PbCl_2$ to precipitate on the surface. To prevent this contamination, electrodeposits were initially rinsed with a $CaCl_2$ solution having the same concentration as the electrolyte but without $PbCl_2$, followed by a rinse with deionized water. The resulting electrodeposits were analyzed using XRD (Rigaku, RINT2200) and their surface characteristics were assessed via scanning electron microscopy (SEM; Keyence, VE-8800).

For comparison purposes, electrodeposition was carried out in a similar manner using a solution containing 0.10 mol kg^{-1} $NaNO_3$ and 100 mmol kg^{-1} $Pb(NO_3)_2$. In this solution, anodic passivation took place at the counter electrode, presumably due to the anodic deposition of PbO_2 on the insoluble anode. For this reason, a small quantity of nitric

acid (60 wt.%) was added to the solution to adjust the pH to 1.0 and electrodeposition was performed in this acidic medium.

3.3. Results and discussion

3.3.1. Solubilities of $PbCl_2$ in $CaCl_2$ solutions

The solubilities of $PbCl_2$ in $CaCl_2$ solutions as determined in this work and expressed as mass and volumetric molar concentrations are presented in Figures 3.1(a) and (b), respectively. These values were found to increase with increases in the $CaCl_2$ concentration. In terms of mass concentration, the solubility of $PbCl_2$ approached an upper limit at a $CaCl_2$ concentration of 6.94 mol kg^{-1} (equivalent to a $H_2O/CaCl_2$ molar ratio, n, of 8). At a $CaCl_2$ concentration of 9.25 mol kg^{-1} (n = 6), the maximum solubility was 0.452 mol kg^{-1} ([Pb(II)] = 93.7 g kg^{-1}). When expressing the solubility in terms of volumetric concentration, it was found that the maximum solubility was 0.351 mol dm^{-3} ([Pb(II)] = 72.8 g dm^{-3}) at a $CaCl_2$ concentration of 6.94 mol kg^{-1} (n = 8). Using a solubility product, log K_{sp}, of –4.78 at 25 °C and an ionic strength, I, of 0,[22] the solubility of $PbCl_2$ in pure water was determined to be 16 mmol dm^{-3} ([Pb(II)] = 3.3 g dm^{-3}). Therefore, it can be concluded that the solubility of $PbCl_2$ was increased by up to 22 times in the concentrated $CaCl_2$ solutions compared with that in pure water. The increase in $PbCl_2$ solubility at higher levels of $CaCl_2$ can be attributed to the stabilization of $[PbCl_x]^{-(x-2)}$ complexes. These complexes will form in conjunction with high degrees of Cl^- activity, as demonstrated by the equations:[21,22]

$$Pb^{2+} + Cl^- = PbCl^+ \quad (3.1)$$

$$PbCl^+ + Cl^- = PbCl_2(aq) \quad (3.2)$$

$$PbCl_2(aq) + Cl^- = PbCl_3^- \quad (3.3)$$

$$PbCl_3^- + Cl^- = PbCl_4^{2-}. \quad (3.4)$$

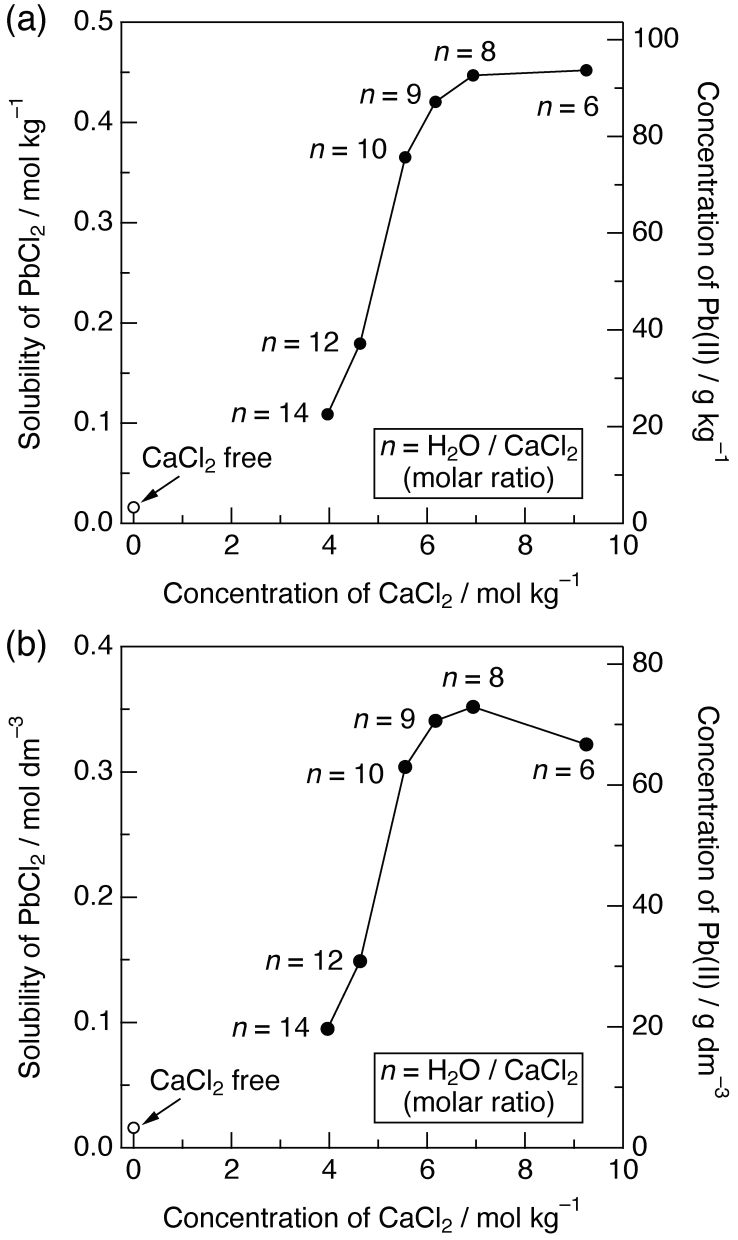

Figure 3.1 Solubilities of $PbCl_2$ (filled circles) in aqueous $CaCl_2$ solutions at room temperature on the basis of (a) mass and (b) volumetric concentration. The solubility in $CaCl_2$-free pure water[22] is also indicated (unfilled circles).

Solubility values obtained for $PbCl_2$ in the present concentrated $CaCl_2$ solutions and for several representative Pb salts in pure water are presented in Table 3.1. The solubilities in the concentrated $CaCl_2$ solutions are reported in both mass and volumetric concentrations. Although the solubilities in the concentrated $CaCl_2$ solutions were lower than those of several salts that are currently used in lead refining, including lead hexafluorosilicate ($PbSiF_6$) and lead sulfamate ($Pb(NH_2SO_3)_2$), these solubilities would still be sufficient for utilization in lead electrodeposition baths.

Table 3.1 Solubilities of various lead salts in pure water and solubilities of $PbCl_2$ in aqueous $CaCl_2$ solutions with six different $CaCl_2$ concentrations.

Lead salt	Solubility (g_{-Pb} dm^{-3})	Solubility (g_{-Pb} kg^{-1})	Ref.
Lead fluorosilicate, $PbSiF_6$	409	-	4
Lead sulfamate, $Pb(NH_2SO_3)_2$	368	-	4
Lead chloride, $PbCl_2$ in			
9.25 mol kg^{-1} $CaCl_2$ aq (n = 6)	66.7	93.7	This work
6.94 mol kg^{-1} $CaCl_2$ aq (n = 8)	72.8	92.7	This work
6.17 mol kg^{-1} $CaCl_2$ aq (n = 9)	70.6	87.2	This work
5.55 mol kg^{-1} $CaCl_2$ aq (n = 10)	62.9	75.7	This work
4.63 mol kg^{-1} $CaCl_2$ aq (n = 12)	31.0	37.2	This work
3.96 mol kg^{-1} $CaCl_2$ aq (n = 14)	19.8	22.6	This work
Lead chloride, $PbCl_2$ in pure water	7.2	-	4
Lead sulfate, $PbSO_4$	0.03	-	4

3.3.2. Electrochemical behavior of lead species

The immersed potentials of Pb in concentrated $CaCl_2$ solutions containing 10 mmol kg^{-1} of $PbCl_2$ are plotted against pCl (defined as $-\log a_{Cl-}$, where for convenience the analytical concentration of Cl^- ions is considered to equal the activity, a_{Cl-}) in Figure 3.2. The potential-pCl diagram is also provided, calculated using standard complexation constants[22] and the standard electrode potential of the Pb^{2+}/Pb redox system,[23] as summarized in Table 3.2. The equilibrium reactions presented in Table 3.3 were used in these calculations and an acidic pH range was assumed over which lead oxides and hydroxides were unstable. The immersed potentials of Pb in the concentrated $CaCl_2$ solutions were shifted to values approximately 180 mV lower than the equilibrium potential of the Pb^{2+}/Pb redox pair, in which Pb(II) ions exist as aquo ions. This result is in good agreement with the expected equilibrium potential for the $PbCl_4^{2-}/Pb$ system, although it includes differences resulting from the Cl^- activity coefficient not considered here. This potential shift suggests that the dominant Pb(II) species in the concentrated $CaCl_2$ solutions was the chloride complex $PbCl_4^{2-}$.

Table 3.2 Formation constants for Pb(II)-Cl complexes, $PbCl_2$ solubility product, and standard electrode potential used to generate the potential-pCl diagram.

Reactions	log K (25 °C, I = 3.0)	Ref.
$Pb^{2+} + Cl^- = PbCl^+$	1.17	22
$Pb^{2+} + 2Cl^- = PbCl_2(aq)$	1.7	22
$Pb^{2+} + 3Cl^- = PbCl_3^-$	1.9	22
$Pb^{2+} + 4Cl^- = PbCl_4^{2-}$	1.2	22
$PbCl_2(s) = Pb^{2+} + 2Cl^-$	–5.0	22
Redox pair	E° (V *vs*. SHE)	Ref.
$Pb^{2+} + 2e = Pb$	–0.126	23

Table 3.3 Equilibrium reactions and conditions used to generate a potential-pCl diagram. The electrode potentials are with reference to Ag|AgCl in 3.33 M KCl aq.

Equilibrium reactions	Equilibrium conditions
$Pb^{2+} + 2e = Pb$	E (V) = –0.332 + 0.0295 log $a_{Pb(II)}$
$PbCl_2(s) + 2e = Pb + 2Cl^-$	E (V) = –0.480 + 0.0591 pCl
$PbCl_4^{2-} + 2e = Pb + 4Cl^-$	E (V) = –0.367 + 0.118 pCl + 0.0295 log $a_{Pb(II)}$
$Pb^{2+} + 2Cl^- = PbCl_2(s)$	2pCl = 5.0 + log $a_{Pb(II)}$
$PbCl_2(s) + 2Cl^- = PbCl_4^{2-}$	2pCl = –3.8 – log $a_{Pb(II)}$

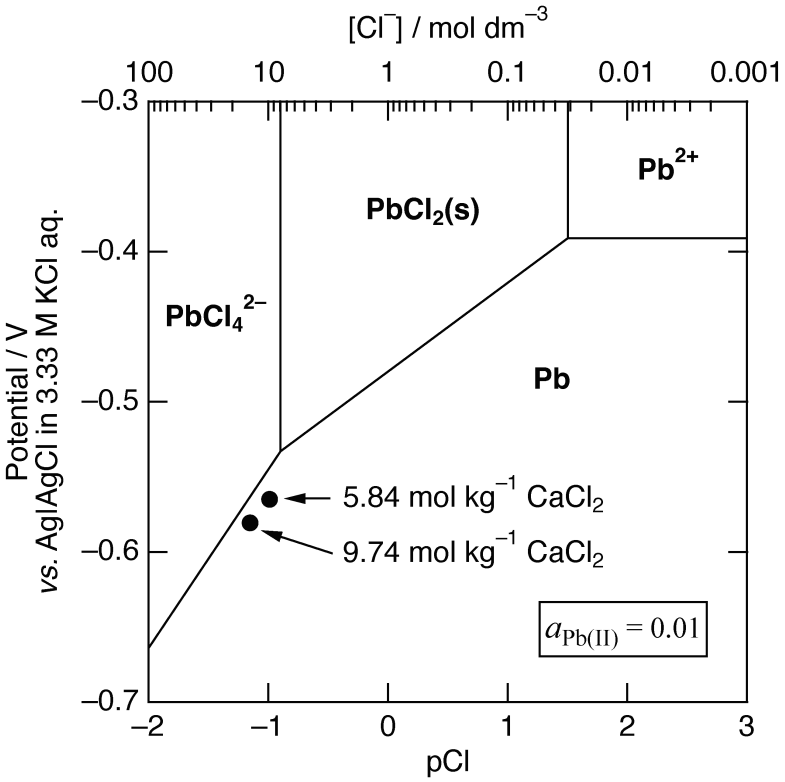

Figure 3.2 A potential-pCl diagram (pCl = –loga_{Cl^-}) for the Pb-Cl-H_2O system at 25 °C ($a_{Pb(II)}$ = 0.01). The rest potentials for a Pb electrode immersed in concentrated aqueous solutions with two different $CaCl_2$ concentrations containing 10 mmol kg^{-1} Pb(II) are indicated. The scale on the upper horizontal axis assumes that a_{Cl^-} is equal to $[Cl^-]$.

Cyclic voltammograms generated with a Pt electrode from $CaCl_2$-$PbCl_2$ and $NaNO_3$-$Pb(NO_3)_2$ solutions with a Pb(II) ion concentration of 10 mmol kg^{-1} are provided in Figure 3.3(a). These data were acquired at a potential sweep rate of 5 mV s^{-1}, with the sweep initiating from the immersion potential and starting in the cathodic direction followed by a reverse sweep in the anodic direction. In Figure 3.3(b), the area over which the reduction and oxidation currents switch during the sweep in the anodic direction is enlarged and the intercept with the potential axis is set to 0 V. The exchange current densities were estimated from a linear approximation of the Butler-Volmer equation at low overpotentials[24] in the range of ±5 mV with respect to a potential of 0 V (see Figure 3.3(b)). This equation was:

$$i = i_0 \left(\frac{mF}{RT}\right) \eta \qquad (3.5)$$

where i_0 is the exchange current density, m is the number of electrons in the rate-determining step (= 2), F is the Faraday constant, R is the ideal gas constant, T is the absolute temperature (= 298.15 K), and η is the overpotential. In addition, the current densities at the potential associated with switching the sweep from the cathodic to anodic direction were extracted and used as the cathodic limiting current densities under static conditions. The exchange and limiting current densities obtained for each solution are summarized in Table 3.4.

Table 3.4 Exchange current densities, i_0, and limiting current densities, i_L, obtained under static conditions.

Solutions	i_0 (μA cm^{-2})	i_L (μA cm^{-2})
9.74 mol kg^{-1} $CaCl_2$	57	134
5.84 mol kg^{-1} $CaCl_2$	131	243
0.10 mol kg^{-1} $NaNO_3$	425	902

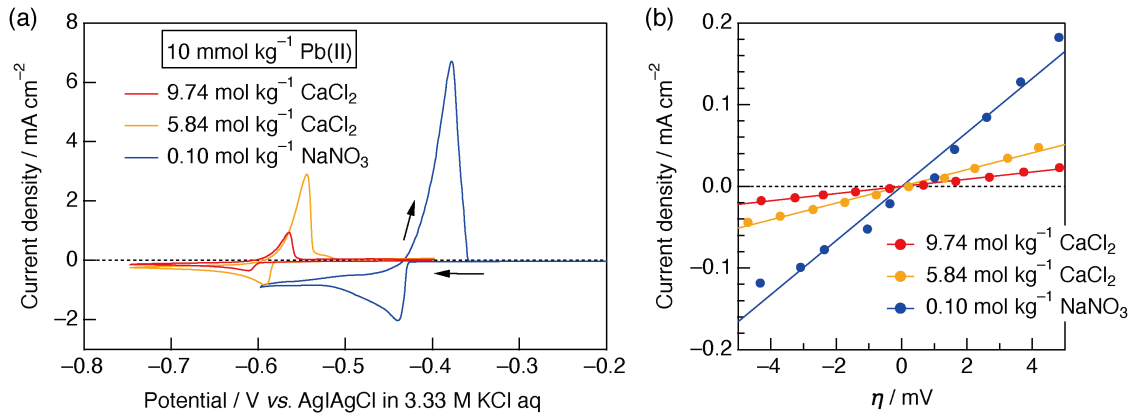

Figure 3.3 (a) Cyclic voltammograms (second cycle) obtained from a Pt electrode with concentrated aqueous $CaCl_2$ solutions or aqueous solutions containing 0.10 mol kg^{-1} $NaNO_3$ and 10 mmol kg^{-1} Pb(II) at a scan rate of 5 mV s^{-1}. (b) Positive-direction voltammograms near the intercept of the potential axis.

It should be noted that a steady-state polarization curve should ideally be applied in association with a low overpotential approximation or a high overpotential approximation (that is, a Tafel slope analysis) to obtain the most accurate exchange current density. However, in the case of the present system, the state of the electrode surface was easily modified during continuous electrolysis due to uneven electrodeposition. Consequently, it was difficult to obtain a steady-state polarization curve and so this study employed a convenient approximation to estimate the exchange current density based on dynamic measurements (that is, cyclic voltammetry). Because the concentration distribution of redox species in front of the electrode deviated somewhat from the steady-state concentration, the estimated exchange current density included a deviation from the true value that was dependent on the potential sweep, but this effect is considered to have been negligible.

The onset potential for lead electrodeposition was shifted negatively with increases in the $CaCl_2$ concentration and this corresponded to the shift in equilibrium potentials noted above. Moreover, both the exchange current density and the limiting current density decreased along with the $CaCl_2$ concentration, as shown in Table 3.4. In particular, the exchange current density obtained from the concentrated 9.74 mol kg^{-1} $CaCl_2$ solution was one order of magnitude lower than that associated with a dilute $NaNO_3$ solution. The exchange current density is an indicator of the electrode kinetics. Hence, the apparent decrease in the exchange current density may have resulted from a higher activation energy for the reduction of $PbCl_4^{2-}$ complexes compared with that for Pb^{2+} aquo ions. This effect would have led to a lower rate constant for the reduction reaction. Increasing the Cl^- activity caused the thermodynamically stable $PbCl_4^{2-}$ complexes to become dominant relative to Pb^{2+} aquo ions. Hence, the electrodeposition reaction, which involved a loss of ligands, likely became less thermodynamically and perhaps less kinetically favorable. The decreased limiting current density noted in conjunction with the concentrated solutions is ascribed to the inhibited diffusion of $PbCl_4^{2-}$ complexes. This phenomenon, in turn, is attributed to increases in both viscosity and ionic interactions as well as to the larger size of the $PbCl_4^{2-}$ ions. To further evaluate these effects, the diffusion coefficients for Pb(II) species were evaluated by hydrodynamic voltammetry, as described in the following section.

3.3.3. Transport characteristics of lead species

Linear sweep voltammograms obtained from an RDE for each solution are presented in Figures 3.4(a–c). In the case of the trials using concentrated $CaCl_2$ solutions (Figures 3.4(a,b)), the reduction currents at potentials lower than –0.6 V correspond to Pb electrodeposition. When using the dilute $NaNO_3$ solution, a constant reduction current was observed in the range of potentials greater than –0.47 V, at which Pb electrodeposition was initiated. A good linear relationship was confirmed between this reduction current and the square root of the rotational speed, $\omega^{1/2}$. Consequently, this current is believed to have resulted from the reduction of nitrate ions or dissolved oxygen in conjunction with mass transport limitations. In a subsequent analysis, the limiting current density for Pb electrodeposition was obtained by subtracting this background current from the measured current.

According to Levich's equation,[25] the relationship between the limiting current density and the rotational speed of the RDE (assuming mass transport limitations) is:

$$i_{\mathrm{L}} = 0.62mFD^{2/3}\nu^{-1/6}c\omega^{1/2} \qquad (3.6)$$

where i_{L} is the limiting current density, D is the diffusion coefficient for the reactant, ν is the kinematic viscosity, c is the reactant concentration in the bulk solution, and ω is the rotational angular velocity of the RDE. To determine c, the Pb(II) concentration was converted from 10 mmol kg^{-1} to a volumetric molar concentration using the density of each solution.

The Levich plots provided as insets to Figures 3.4(a–c) demonstrate a good linear relationship between i_{L} and $\omega^{1/2}$ in all solutions. The diffusion coefficients calculated from the slopes of the Levich plots are summarized in Table 3.5 along with the static viscosity, density, and kinematic viscosity data. Using the diffusion coefficient and the

limiting current density determined for static conditions (Table 3.4), the diffusion layer thickness, δ, for static conditions in each solution was calculated based on the Nernst diffusion layer (eq.3.7)[25] using the equation:

$$i_{\mathrm{L}} = \frac{mFDc}{\delta} \qquad (3.7)$$

These values are provided in Table 3.5. Interestingly, the diffusion coefficients for Pb(II) species in the concentrated $CaCl_2$ solutions were significantly lower than those in dilute $NaNO_3$ solutions. In particular, the value for a 9.74 mol kg^{-1} $CaCl_2$ solution was reduced by a factor of 25. As discussed above, this difference can possibly be ascribed to the higher viscosity of the former solution and to stronger ionic interactions in this solution, both of which inhibited the diffusion of Pb(II) species. As the $CaCl_2$ concentration was increased, the diffusion layer was thinned. In particular, in the case of the 9.74 mol kg^{-1} $CaCl_2$ solution, the thickness was decreased by 80 % compared with that of the dilute solution.

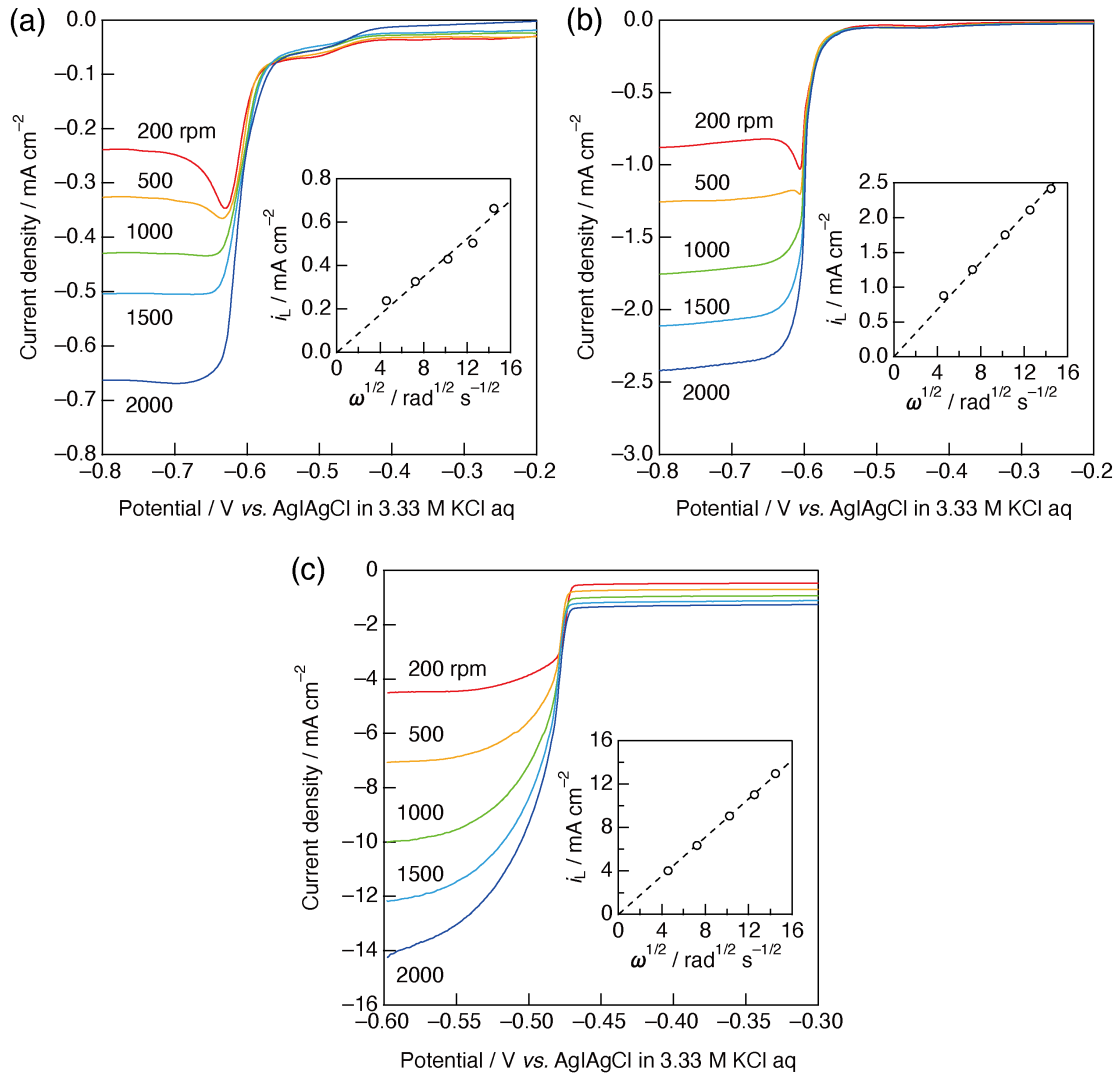

Figure 3.4 Linear sweep voltammograms acquired using an RDE for 10 mmol kg^{-1} Pb(II) aqueous solutions containing (a) 9.74 mol kg^{-1} $CaCl_2$, (b) 5.84 mol kg^{-1} $CaCl_2$, and (c) 0.10 mol kg^{-1} $NaNO_3$ at a scan rate of 10 mV s^{-1}.

Table 3.5 Values for the static viscosity, μ, density, d, kinematic viscosity, ν, diffusion coefficient for Pb(II) species, D, and Nernst diffusion layer thickness, δ, under static conditions for various solutions containing 10 mmol kg^{-1} Pb(II).

Solutions	μ (mPa s)	d (g cm^{-3})	ν (mm^2 s^{-1})	D (10^{-6} cm^2 s^{-1})	δ (μm)
9.74 mol kg^{-1} $CaCl_2$	39	1.53	26	0.25	26
5.84 mol kg^{-1} $CaCl_2$	7.3	1.38	5.3	1.1	70
0.10 mol kg^{-1} $NaNO_3$	0.95	1.01	0.94	6.3	135

In a study of Ag deposition from concentrated $CaCl_2$ solutions,[15] the exchange current density associated with Ag electrodeposition decreased with increases in the $CaCl_2$ concentration. The exchange current density was up to one order of magnitude less than that obtained from a $CaCl_2$-free dilute solution containing Na_2SO_4 as the supporting electrolyte. In addition, the diffusion coefficient for Ag(I) species was decreased by a factor of up to 30 with increases in the $CaCl_2$ concentration while the diffusion layer thickness was decreased by up to 79 % compared with such a dilute solution. The same phenomena were observed during Pb electrodeposition trials in the present study. This agreement suggests that decreases in the exchange current density, diffusion coefficient, and diffusion layer thickness with increasing $CaCl_2$ concentrations will occur during the electrodeposition of various metals from concentrated $CaCl_2$ solutions.

3.3.4. Lead electrodeposition

The potentiostatic electrodeposition of Pb(II) was performed under static conditions using aqueous solutions containing 5.84 mol kg^{-1} $CaCl_2$ or 0.10 mol kg^{-1} $NaNO_3$ with pH adjusted to 1.0, all containing 100 mmol kg^{-1} Pb(II). Photographic images and surface SEM images of the resulting electrodeposits are shown in Figure 3.5. The dilute $NaNO_3$ solutions generated faceted crystal grains approximately 1.5 μm in size on the copper substrate (Figures 3.5(a,d,g)). In contrast, the concentrated $CaCl_2$ solutions gave smaller grains (less than 1 μm in size) at a higher density along with some dendritic and needle-like deposits. The XRD patterns presented in Figure 3.6 confirm that the deposits obtained from both solutions comprised crystalline face centered cubic Pb. It should be noted that chlorine and oxygen were evidently produced at the counter electrode in the concentrated $CaCl_2$ and dilute $NaNO_3$ solutions, respectively.

Figure 3.7 shows current-time plots acquired during electrolysis. In all cases, the applied potential was sufficiently negative for the Pb electrodeposition to reach the point of mass transport limitation. Therefore, the current density exhibited a decay in the early stage of electrolysis, representing a diffusion limiting current on a relatively smooth electrode surface. The subsequent increase in the current density corresponds to an increase in the effective surface area of the electrode due to the formation of uneven electrodeposits such as dendrites. Whereas the current density increased markedly over time in the dilute $NaNO_3$ solution, the increase in the concentrated $CaCl_2$ solution was slower and not as significant. These results are consistent with the dense deposits obtained from the latter. In the concentrated $CaCl_2$ solution, dense grains are thought to have been formed in the early stage of the trial while dendritic deposition occurred in the later stage. Hence, the dense deposits generated from the concentrated $CaCl_2$

solution were related to the thin diffusion layer in this solution and to the extremely low diffusion coefficient for Pb(II) species.[15]

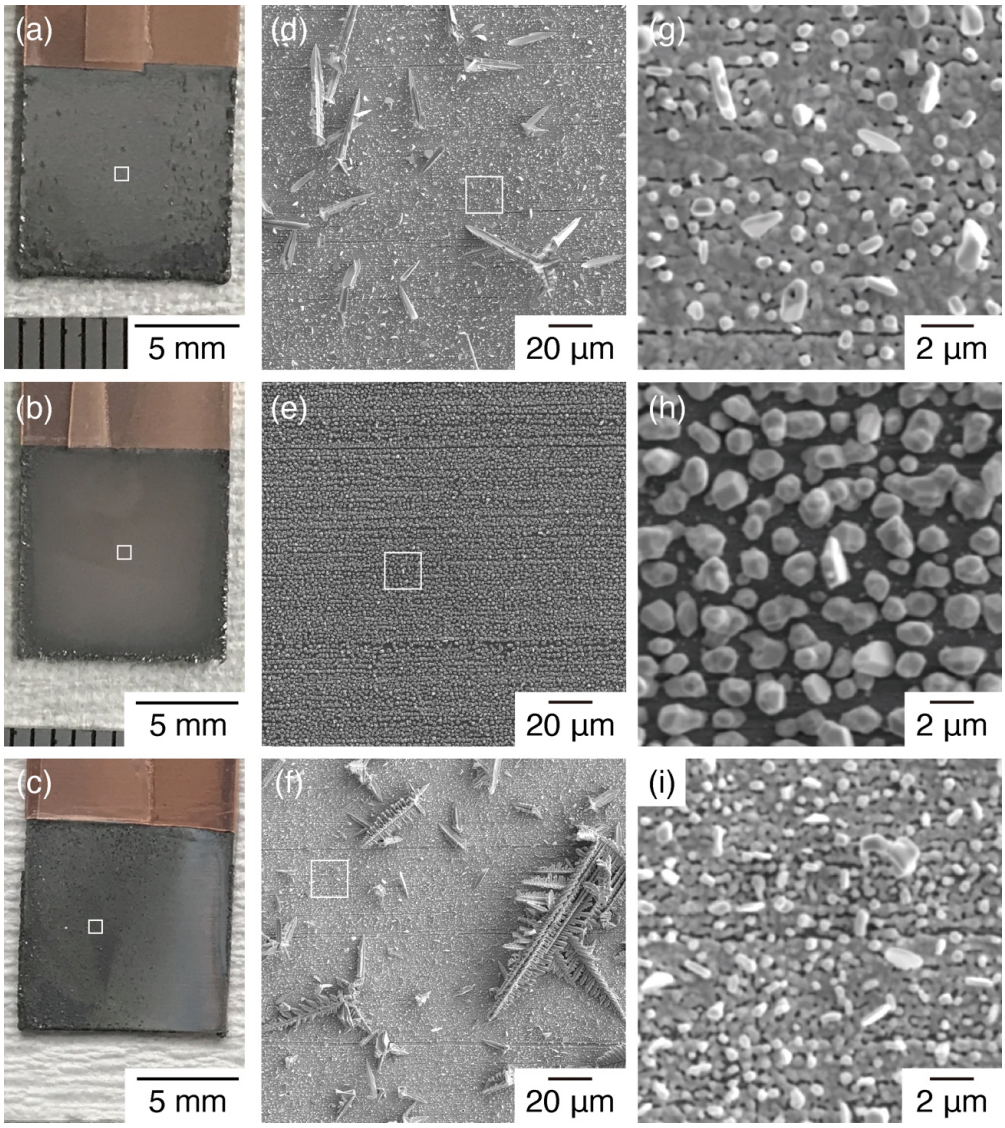

Figure 3.5 (a–c) Photographs and (d–i) surface SEM images of deposits obtained via potentiostatic electrodeposition using aqueous solutions containing 100 mmol kg^{-1} Pb(II) and 5.84 mol kg^{-1} $CaCl_2$ (a,d,g) without stirring and (c,f,i) with stirring at 400 rpm, and from aqueous solutions containing (b,e,h) 0.10 mol kg^{-1} $NaNO_3$ with pH adjusted to 1.0. The square regions outlined in (a–c) indicate the regions from which the images in (d–f) were acquired while the squares in (d–f) indicate the regions from which the images in (g–i) were obtained.

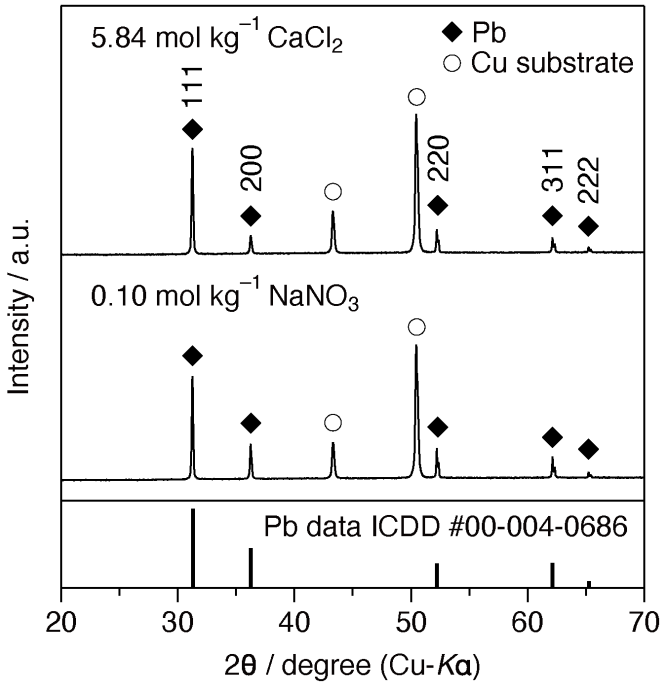

Figure 3.6 XRD patterns for deposits obtained via potentiostatic electrodeposition without electrolyte agitation.

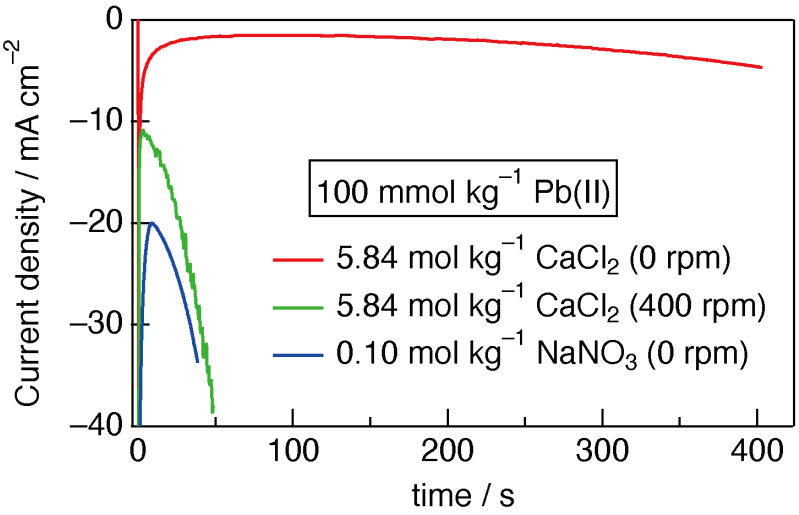

Figure 3.7 Current density data over time during potentiostatic electrodepositions with and without electrolyte agitation.

The effect of solution agitation on electrodeposition was also investigated. The electrodeposits obtained with agitation and the associated current-time transition curve are provided in Figures 3.5(c,f,i) and in Figure 3.7, respectively. As a result of accelerated mass transport, the current density was greatly increased, including during the initial stage of electrolysis. Additionally, the electrolysis period required for a charge of 1 C cm^{-2} was reduced to one-eighth of that without agitation. Thus, agitation is an effective means of promoting mass transport and increasing the electrodeposition rate even when using viscous concentrated solutions. The frequency of dendrite formation was also observed to increase while the effective surface area of the electrode became significantly higher at greater current density values. Dendritic deposition was most prominent on the leftmost half of the electrode (the area with the black appearance in Figure 3.5(c)), which was upstream of the forced convection generated by the agitation. This effect is attributed to preferential growth at the sites at which dendrites were initially generated on the electrode. This growth was, in turn, a result of the enhanced supply of Pb(II) species in the upstream region. In future, smoother deposits could potentially be obtained by optimizing the electrode arrangement and adding smoothing additives, such as those used in conventional industrial electrodeposition.

3.4. Conclusions

The characteristics of Pb electrodeposition from concentrated $CaCl_2$ solutions were examined. Lead chloride, which is poorly soluble in pure water at room temperature, was found to be soluble up to a concentration of 0.351 mol dm^{-3} ([Pb(II)] = 72.8 g dm^{-3}) in concentrated $CaCl_2$ solutions based on the formation of $PbCl_4^{2-}$ complexes. This solubility was a result of the high Cl^- activity of such solutions. Electrochemical analyses of Pb electrodeposition indicated a significant reduction in both the exchange current density and the limiting current density with increases in the $CaCl_2$ concentration. Potentiostatic electrodeposition under mass transport limitations generated electrodeposits consisting of grains below 1 μm in size. High viscosity and strong ionic interactions limited the diffusion of Pb(II) species in such solutions, resulting in slower electrodeposition rates. However, agitation of the solutions overcame these limitations and increased the electrodeposition rate, although stirring also promoted dendritic deposition.

Chloride solutions have rarely been employed for the purpose of Pb electrolysis in the past due to the low solubility of $PbCl_2$ in such solutions. Even so, the present work confirms that concentrated $CaCl_2$ solutions have the potential to expand the use of chloride systems across a wider range of Pb(II) concentrations. Consequently, this approach could be employed to construct lead electrolysis systems. It should be noted that electrorefining baths based on concentrated $CaCl_2$ solutions might dissolve various metal ions as chloride complexes, which may be a problem. Further study is required to obtain a better understanding of the anodic dissolution of crude lead and other impurity elements to allow such solutions to be employed in electrometallurgy.

References

1. Japan Oil Gas Metals National Corporation, *Mineral Resources Material Flow 2019.* (Japan Oil Gas Metals National Corporation, Tokyo, 2020), pp. 21–37.
2. J. A. González-Domínguez, E. Peters, and D. B. Dreisinger, *J. Appl. Electrochem.*, **21**(3), 189–202 (1991).
3. T. Dobrev and S. Rashkov, *Hydrometallurgy*, **40**(3), 277–291 (1996).
4. M. Jordan, in *Modern Electroplating*, edited by M. Schlesinger and M. Paunovic, 5th Ed. (John Wiley & Sons, New York, 2010), pp. 249–263.
5. M. Jordan, in *Modern Electroplating*, edited by M. Schlesinger and M. Paunovic, 5th Ed. (John Wiley & Sons, New York, 2010), pp. 265–284.
6. E. Expósito, J. González-García, P. Bonete, V. Montiel, and A. Aldaz, *J. Power Sources*, **87**(1–2), 137–143 (2000).
7. R. Piontelli, *J. Electrochem. Soc.*, **94**(3), 106–108 (1948).
8. B. Jin and D. B. Dreisinger, *Sep. Purif. Technol.*, **170**, 199–207 (2016).
9. S. M. Wong and L. M. Abrantes, *Electrochim. Acta*, **51**(4), 619–626 (2005).
10. Y.-S. Liao, P.-Y. Chen, and I.-W. Sun, *Electrochim. Acta*, **214**, 265–275 (2016).
11. S. Tan, F. E. Bedoya-Lora, J. P. Hallett, and G. H. Kelsall, *Electrochim. Acta*, **376**, 137893 (2021).
12. G. Díaz and D. Andrews, *JOM*, **48**(1), 29–31 (1996).
13. D. Andrews, A. Raychaudhuri, and C. Frias, *J. Power Sources*, **88**(1), 124–129 (2000).
14. P. Xing, C. Wang, L. Wang, B. Ma, and Y. Chen, *Hydrometallurgy*, **189**, 105134 (2019).

15. K. Adachi, A. Kitada, K. Fukami, and K. Murase, *J. Electrochem. Soc.*, **166**(10), D409–D414 (2019).
16. K. Adachi, A. Kitada, K. Fukami, and K. Murase, *Electrochim. Acta*, **338**, 135873 (2020).
17. A. A. Chialvo and J. M. Simonson, *J. Chem. Phys.*, **119**(15), 8052–8061 (2003).
18. B. Carlsson, H. Stymne, and G. Wettermark, *Sol. Energy*, **23**(4), 343–350 (1979).
19. J. A. Rard and S. L. Clegg, *J. Chem. Eng. Data*, **42**(5), 819–849 (1997).
20. A. Kitada, K. Adachi, and K. Murase, *Kinzoku mataha kinzokuen no youkaiyou youeki oyobi sono riyou*, JP Patent P2019–123927A (July 25, 2019).
21. R. G. Holdich and G. J. Lawson, *Hydrometallurgy*, **19**(2), 199–208 (1987).
22. R. M. Smith and A. E. Martell, *Critical Stability Constants Vol.4 Inorganic Complexes*, 2nd Ed. (Plenum Press, New York, 1976), p. 109.
23. M. Pourbaix, *Atlas of Electrochemical Equilibria in Aqueous Solutions*, 2nd Ed. (NACE, Houston, 1974), p. 487.
24. V. S. Bagotsky, *Fundamentals of Electrochemistry*, 2nd Ed. (John Wiley & Sons, New York, 2005), pp. 79–98.
25. A. J. Bard and L. R. Faulkner, *Electrochemical Methods: Fundamentals and Applications*, 2nd Ed. (John Wiley & Sons, New York, 2000), p. 339.

This chapter is reproduced with permission from Journal of MMIJ:
“Lead Electrodeposition from Highly Concentrated Calcium Chloride Aqueous Solutions,”
Masayuki Miyamoto, Atsushi Kitada, Ken Adachi, Kazuhiro Fukami, and Kuniaki Murase,
Journal of MMIJ, **137**(11), 103–109 (2021).

The final publication is available at J-Stage via:
https://doi.org/10.2473/journalofmmij.137.103

General Conclusions

The present study investigated the electrochemical deposition of copper and lead as a means of addressing various sustainability-related issues in wet electrolytic refining processes, focusing on the factors and requirements unique to actual industrial processes.

The primary cause of current loss in copper electrorefining is abnormal electrodeposition, otherwise known as nodulation. This work examined the contributions of several impurity elements that may act to promote the growth of nodules and provided valuable insights that could allow this process to be improved. Chapter 1 provided information concerning the growth characteristics of nodules incorporating anode slime particles. Experimental analyses of nodules recovered from an industrial tank house suggested that the upper portions of such nodules preferentially incorporated these particles. Simulations of suspended particle transport in association with convection indicated that strong upward convection is formed in conjunction with nodules, generating vortices above nodules. These vortices facilitate the repeated circulation of particles, resulting in their preferential incorporation into nodules. The inclusion of slime particles alteres the morphology of the nodules and increases the level of impurities in the final product. Hence, more efficient removal of suspended particles from the electrolyte via filtration may be a viable means of suppressing nodule growth.

Chapter 2 examined the effects of dissolved impurity ions, specifically Ni(II) and Sb(III), on the growth of nodules. Electrolytic experiments were conducted in solutions containing various impurities to assess the growth behavior of nodule-mimicking protrusions attached to the cathode. These trials established that such impurities enhance surface roughening and promote the growth of protrusions.

Microscopic-scale roughness on the protrusions was also found to facilitated current concentration such that convexities are formed, eventually leading to rapid growth with dendritic deposition. As such, it is evidently crucial to prevent a BR-type structure transition caused by impurity ions and to maintain smooth growing surfaces by controlling the impurity levels and the dosage of smoothing additives.

Chapter 3 summarized work with concentrated $CaCl_2$ solutions serving as alternative electrolytic systems for lead electrorefining. These solutions were found to be effective and could replace potentially hazardous fluorosilicic acid electrolytic baths. The high activity of chloride ions in concentrated $CaCl_2$ solutions were shown to promote the dissolution of $PbCl_2$ at a concentration suitable for use in lead electrodeposition baths. This technique is cost-effectiveness and generates an effluent with minimal environmental impact. Hence, concentrated $CaCl_2$ solutions could be advantageous with regard to industrial applications. The lead deposits obtained from these concentrated solutions exhibited smaller and denser grains than those generated from a typical dilute solution. However, the deposition rate remains an issue due to slow mass transfer. Agitation could possibly address this issue, although additional research is required to obtain smoother deposits.

This study provides novel insights and practical strategies to mitigate challenges related to modern electrolytic refining processes. The work reported herein also demonstrates methodologies that include process modeling and analysis based on both numerical simulations and experimentation, as well as the exploration of systems meeting the requirements for industrial processing. Such techniques are expected to make valuable contributions to future process improvements.

List of Publications

Chapter 1

Masayuki Miyamoto, Shohei Mitsuno, Atsushi Kitada, Kazuhiro Fukami, Kuniaki Murase,
"Mechanism of nodular growth in copper electrorefining with the inclusion of impurity particles under natural convection,"
Hydrometallurgy, **216**, 106013/1–12 (2023).

(Proceedings of international conferences)
Masayuki Miyamoto, Atsushi Kitada, Kazuhiro Fukami, Kuniaki Murase,
"Tertiary Current Distribution Analysis for Simulation of Nodule Growth in Copper Electrorefining,"
Proceedings - Copper2022, Vol. 5 (Electrometallurgy), Instituto de Ingenieros de Minas de Chile, Santiago, Chile, 2022, pp. 125–136.

Chapter 2

Masayuki Miyamoto, Yuki Ishikawa, Kazuhiro Fukami, Kuniaki Murase,
"Surface Roughening and Growth-Promoting Effects on Nickel and Antimony on Nodules in Copper Electrorefining,"
Metallurgical and Materials Transactions B, **54**, 3579–3590 (2023).

Chapter 3

Masayuki Miyamoto, Atsushi Kitada, Ken Adachi, Kazuhiro Fukami, Kuniaki Murase,
"Lead Electrodeposition from Highly Concentrated Calcium Chloride Aqueous Solutions,"
Journal of MMIJ, **137**(11), 103–109 (2021).

The following publications are not included in this thesis.

Ken Adachi, Yuya Nakai, Shohei Mitsuno, Masayuki Miyamoto, Atsushi Kitada, Kazuhiro Fukami, Kuniaki Murase,
"The Mechanism of Nodular Growth in Copper Electrorefining,"
Journal of MMIJ, **136**(2), 8–13 (2020).

Takumi Yasuda, Masahiro Nakata, Masayuki Miyamoto, Atsushi Kitada, Kuniaki Murase, Kazuhiro Fukami,
"Unexpected Downstream Mode of Spatiotemporal Rotating Waves Found in the Model of H_2O_2 Reduction on a Platinum Ring-Shaped Electrode under Mild Convection,"
The Journal of Physical Chemistry C, **125**(13), 74240–7250 (2021).

Masahiro Nakata, Takumi Yasuda, Masayuki Miyamoto, Atsushi Kitada, Yutaka Okazaki, Reiko Oda, Kuniaki Murase, Kazuhiro Fukami,
"Production of Noble-Metal Nanohelices Based on Nonlinear Dynamics in Electrodeposition of Binary Copper Alloys,"
Nano Letters, **23**, 462–468 (2023).

Acknowledgments

This work was carried out under the supervision of Professor Kuniaki Murase, Department of Materials Science and Engineering, Graduate school of Engineering, Kyoto University. First and foremost, the author would like to express sincere gratitude to Professor Kuniaki Murase for his invaluable guidance and tremendous support.

The author is also profoundly grateful to Professor Hiroyuki Sugimura, Department of Materials Science and Engineering, Graduate school of Engineering, Kyoto University, and Professor Tetsuya Uda, Department of Materials Science and Engineering, Graduate school of Engineering, Kyoto University, for their careful review and critical comments on this thesis.

The author is deeply grateful to Associate Professor Kazuhiro Fukami, Department of Materials Science and Engineering, Graduate school of Engineering, Kyoto University for his insightful suggestions and encouragement on numerous occasions.

The author expresses his appreciation to Associate Professor Atsushi Kitada, Department of Chemical System Engineering, Graduate School of Engineering, The University of Tokyo, for his generous support and fruitful discussions.

The author would like to thank Assistant Professor Ken Adachi, Center for Mineral Processing and Metallurgy, Institute of Multidisciplinary Research for Advanced Materials, Tohoku University, for his careful guidance and advice.

The author's thanks also go to Mr. Shohei Mitsuno and Mr. Yuki Ishikawa, graduates of the master's course in Professor Murase's laboratory, for their invaluable contributions to conducting several experiments and engaging in discussions during the development of this thesis.

Deep thanks are expressed to Ms. Sari Nakano and Ms. Kumi Hirose, the assistant administrative staff of Professor Murase's laboratory, for their support, which enabled the author to fully concentrate on the study.

The author would like to express deep gratitude to all members of Professor Murase's laboratory. The days spent engaging in research with Assistant Professor Kiho Nishioka, Dr. Takumi Yasuda, Dr. Ryutaro Miura, Mr. Takahiro Mori, Mr. Yuki Murakami, and Mr. Haruki Katori in the PhD program were stimulating and instructive. The team's diverse perspectives and expertise made the research experience truly fascinating.

Finally, the author would like to express his sincere appreciation to his parents for their unwavering support.

March 2024

Masayuki Miyamoto